ORNL/TM-2014/447

Fusion Materials Research at Oak Ridge National Laboratory in Fiscal Year 2014

Complied by:

F.W. Wiffen
S.P. Noe
L.L. Snead

October 2014

OAK RIDGE NATIONAL LABORATORY
MANAGED BY UT-BATTELLE FOR THE US DEPARTMENT OF ENERGY

Materials Science and Technology Division

FUSION MATERIALS RESEARCH AT OAK RIDGE NATIONAL LABORATORY IN FISCAL YEAR 2014

Complied by:

F.W. Wiffen
S.P. Noe
L.L. Snead

Date Published: October 2014

Prepared by
OAK RIDGE NATIONAL LABORATORY
Oak Ridge, Tennessee 37831-6283
managed by
UT-BATTELLE, LLC
for the
US DEPARTMENT OF ENERGY
under contract DE-AC05-00OR22725

CONTENTS

Page

LIST OF FIGURES

Figure **Page**

Figure **Page**

Figure **Page**

Figure **Page**

LIST OF TABLES

1.0 INTRODUCTION

Lance Snead (sneadll@ornl.gov), Yutai Katoh and Bill Wiffen

The realization of fusion energy is a formidable challenge with significant achievements resulting from close integration of the plasma physics and applied technology disciplines. Presently, the most significant technological challenge for the near-term experiments such as ITER, and next generation fusion power systems, is the inability of current materials and components to withstand the harsh fusion nuclear environment. The overarching goal of the ORNL fusion materials program is to provide the applied materials science support and understanding to underpin the ongoing DOE Office of Science fusion energy program while developing materials for fusion power systems. In doing so the program continues to be integrated both with the larger U.S. and international fusion materials communities, and with the international fusion design and technology communities.

The ORNL program on materials continues to pursue development of low activation structural materials such as the Reduced Activation Ferritic/Martensitic Steels, the higher strength/higher creep resistant Nano Composited Ferritic Steels, and Silicon Carbide Composites. A significant recent change is the increased emphasis on high heat flux testing and the development of refractory metals. This includes the use of an ORNL Plasma Arc Lamp facility adapted for the thermal testing of irradiated materials, the development and evaluation of new tungsten materials, and the study and understanding of the irradiation performance of tungsten. In each case the materials are being developed in a design-informed fashion where properties improvements are led by fusion-relevant design studies and directed at advancing the Technology Readiness Level of the material systems. A limited effort is directed towards diagnostic materials and high-temperature superconductors. In the area of diagnostics, ORNL continues to develop irradiation-hardened dielectric mirrors and to support basic irradiation materials science of ceramics for diagnostic systems. For high-temperature superconductors the ORNL program has undertaken a limited program to quantify the irradiation sensitivity of the most recently developed tape materials. Finally, this program integrates fundamental modeling into the development efforts as much as practicable.

This program makes heavy reliance on neutron irradiation in HFIR, the High Flux Isotope Reactor at ORNL. This is complemented by use of the ORNL-University of Tennessee ion irradiation facility when that facility is better suited to explore fundamental aspects of materials behavior under irradiation. In the longer term, we are looking forward to using the proposed FMITS facility that will allow irradiation in the more fusion-relevant neutron field of the ORNL Spallation Neutron Source.

This document provides a summary of Fiscal Year - 2014 activities supporting the Office of Science, Office of Fusion Energy Sciences Materials Research for MFE (AT-60-20-10-0) carried out by ORNL. The organization of this report is mainly by material type, and then with sections on specific technical activities. The four projects selected in the Funding Opportunity Announcement solicitation of late 2011 and first funded in late FY 2012 are identified by "FOA" in the titles. A newer activity, "Materials Engineering in Support of the FNSF Program," is reported in Chapter 10.0. The fusion materials effort consists of a wide array of tasks and collaborations both within the US and with international partners. The major continuing international collaborating partners are the Japan Atomic Energy Agency (the US-JAEA collaboration), the Japanese National Institute for Fusion Sciences (the PHENIX collaboration) and the Karlsruhe Institute of Technology in Germany. The latter two collaborations, now in their third year, focus on high heat flux materials and refractory metals.

Milestones for the ORNL program were listed in the five FWPs for the program. Of 22 listed milestones listed in Table 1, ten were completed as scheduled, three were completed ahead of schedule, and nine have been rescheduled or cancelled.

Table 1. Status of Fiscal Year 2014 Milestones in ORNL Fusion Materials Program Field Work Proposals

FWP-ERAT 725 – Base Program - FY2014	**Schedule & Status**
Irradiate high-temperature superconducting tapes in HFIR.	5/1/14 **Delayed**
Changes in capsule design to include TE materials. HFIR irradiation started 10/07/14	
Complete first ferritic steel thermal convection loop with Pb-Li (1000 h, 550°C peak)	6/30/14 **Done** 6/30/14
Report on nanostructured two-phase ferritic-martensitic materials and basic properties	8/31/14 **Cancel**
Staff departure	
Publish the results on MD-based investigation of helium bubble hardening mechanisms	8/31/14 **Delayed**
Rescheduled completion 12/31/14	
With PHENIX, complete fixturing of one PAL high-heat flux test of tungsten	9/10/14 **Done** 2/15/14
With PHENIX, develop thermo-mechanical model of PAL high-heat flux test stand	9/10/14 **Delayed**
Rescheduled due to new focus on PHENIX needs and budget limits. 9/30/15	
Complete mechanical tests for advanced MC-reinforced RAFM steels	9/30/14 **Early** 8/31/14
Quantify microstructure of ODS particles and swelling in irradiated 9Cr and 14Cr NFAs	9/30/14 **Cancel**
Staff departure	
Complete microstructural examination of 70 dpa irradiated silicon carbide composites	9/30/14 **Done** 7/31/14
Complete electrical characterization of neutron irradiated HTS conductors.	9/30/14 **Delayed**
Delayed by change in irradiation schedule. Rescheduled completion 8/31/15	
Complete optical and microstructural characterization of 1 and 4 dpa dielectric mirrors.	9/30/14 **Done** 9/31/14
Publish assessment of empirical potentials used for primary damage formation in SiC	9/30/14 **Delayed**
Rescheduled completion 12/31/14	
Develop outline materials roadmap for credible pathway to design, construct and operate FNSF	9/30/14 **Delayed**
Rescheduled. Need FNSF concept and operating condition definitions before outlining materials roadmap.	
FWP-ERAT752 Friction Stir Welding - FOA	
Complete computational model of temperature and deformation during FSW of ODS alloys	3/31/14 **Delayed**
Behind schedule, due to staff changes. Rescheduled completion 9/30/15	
Quantify the effect of FSW on the nano particle size and distribution in FSW joints	9/30/14 **Done** 9/30/14
[Develop FSW conditions to produce defect free joints between ODS/NFA and RAFM	3/30/15 **Early** 3/31/14]
FWP-ERAT754 Structural Materials of Potentially Unique Irradiation Resistance - FOA	
Complete HFIR irradiations of mechanical, thermal and microstructural specimens	6/30/14 **Done** 6/30/14
FWP- ERAT762 Silicon Carbide Joining Technology for Fusion Energy Applications - FOA	
Draft ASTM test standard for shear strength of ceramic joints	3/31/14 **Done** 3/31/14
FWP-ERAT763 Development of High-Cr ODS Alloys with Zr Additions for Fusion - FOA	
Complete characterization of first ODS FeCrAl composition	1/31/14 **Done** 1/31/14
Initiate compatibility testing of program alloys in Pb-Li	4/30/14 **Done** 4/30/14
Complete first Pb-Li compatibility test of new ODS FeCrAl	6/30/14 **Early** 5/31/14
Complete initial tensile testing and three creep tests on new ODS FeCrAl alloy	9/30/14 **Done** 9/30/14

2.0 FMITS – THE FUSION MATERIAL IRRADIATION TEST STATION AT SNS

M. W. Wendel (wendelmw@ornl.gov), and P. D. Ferguson

OBJECTIVE

The Fusion Materials Irradiation Test Station (FMITS) is a proposed irradiation facility for the Spallation Neutron Source (SNS). This design and planning effort aims to develop the proposal and to minimize risk to SNS normal operations and safety. Because of the uncertainties associated with both modeling and ion irradiation experiments, there is a clear need for a fusion materials irradiation facility that can provide near-prototypic levels of helium and hydrogen production, along with displacement damage, for screening candidate fusion materials. A modest range of He/dpa ratios is desirable to help calibrate and verify the modeling studies. Development of such a facility will provide the opportunity for the US program to take the scientific lead in this critical area of fusion structural materials development.

SUMMARY

The feasibility of the Fusion Materials Irradiation Test Station (FMITS) was confirmed in FY2014 based on a Feasibility Study Report, 30% Design Review, and a Preliminary Safety Assessment. FMITS is proposed as a modification to the SNS target station in order to promote advances in fusion materials candidates. A $13.4 million /4 year project plan (including $2.6 M and 1 year contingency) has been developed for a potential FMITS project. This estimate includes the cost of the first FMITS experiment harness and a contribution toward the first two FMITS-style target modules. The 30% design review committee confirmed the feasibility of the design, clarified technical vulnerabilities and made some helpful recommendations that will strengthen the viability of FMITS as a project. Planned work for FY2015 will substantially mitigate the technical project risk, strengthen the preliminary safety assessment, and secure the operational reliability case based on the review committee recommendations. These are high priority items for preparation of an anticipated viability review by DOE.

PROGRESS AND STATUS

A feasibility study for including a fusion materials irradiation capability in the SNS target station has been completed. FMITS is a proposed modification to the SNS target station to provide a temperature-controlled sample irradiation environment with a helium generation-to-dpa (displacements per atom) ratio that is prototypic of a fusion reactor. The test sections will be placed within two horizontal tubes extended forward of the target module, where the materials radiation response parameters will resemble the conditions for water-cooled first-wall facilities such as ITER. Samples will be located on the edge of or just outside the SNS 7 cm high by 20 cm wide elliptical proton beam. As envisioned in a previous Design Study (2011), the FMITS test sections require gas, water, and instrumentation lines for experimental performance, facility safety, and reliability. The 2011 study proposed some ideas for the design, and this feasibility study presents workable solutions (including engineering solid models) to the design challenges that were identified.

The main goals of the current work on FMITS are to advance the design and address the risk to the SNS neutron science mission. The SNS operations staff was actively engaged in the discussions and planning activities for this effort, ensuring there is no disconnect between current operations and FMITS planning ideas. The SNS safety officer and radiation safety officer have been consulted in the planning, and a preliminary safety analysis has also been completed.

Changes made to the target station to incorporate FMITS will be completely reversible. There are three functional target station components that must be designed or modified to accommodate FMITS: (1) the FMITS experiment harness, (2) the SNS target module, and (3) the SNS vent-line shield block (VLSB). The FMITS test sections that

contain the material samples are part of a replaceable harness weldment that must be designed to slide onto and off the target module. The experiment harness, along with its connections and cabling, will be a new addition to the target station. It is intended for use on multiple targets and assumes the sealing function between the target and the core vessel flange. The SNS target module, especially the external water-cooled shroud, must be modified to accommodate the FMITS harness. The VLSB—a long, narrow shield block on the target carriage that houses the mercury system vent line and conducts instrumentation to and from the target—must be redesigned and replaced before FMITS can be operated. FMITS instrumentation cables and gas tubing will be included in the new VLSB design. Besides these three functional assemblies, other handling and storage fixtures and support systems need to be designed for FMITS operation. All installation and handling operations must be performed remotely using manipulators, and smoothly integrated into normal operations with minimal impact to the neutron science program. The design ideas presented in the feasibility report are ready for an extensive mock-up testing phase should DOE decide that FMITS is a viable project.

FMITS operation should have no impact on the neutron production schedule, although additional resources to monitor and maintain the target station will be required. Increased activity and equipment usage will result in commensurate maintenance requirements. Much of the FMITS harness-related remote-handling activity— such as the installation, removal, and storage of the experiment harness—could be performed during scheduled maintenance outages without prolonging the outage. Operations such as material sample extraction could be performed while the beam is on target. Analysis indicates that moderator performance would be unaffected by the addition of the FMITS tubes in front of the target. Some complication is introduced into the operation of the target imaging beam-alignment system (TIS), but the changes can be managed to ensure that the TIS maintains function, keeping the beam parameters within requirements.

Outside of normal operations, the addition of the FMITS presents potential delays and risks; but the risk is managed so that prolonged impacts to the neutron production schedule could be avoided by ending a particular FMITS experiment. In the case of an unanticipated target failure, the outage would be prolonged by 2–4 days because of the additional handling requirements of the FMITS harness. There is a potential for instrumentation failures within FMITS, and some possibility of gas or water leaks or mechanical failures; but the risks are within the range of those already assumed for target operations, and the mitigation strategy is comprehensive.

Off-normal failures of the FMITS harness are limited in their consequence by keeping the FMITS modification reversible. Although the target modules will not be backward-compatible, the FMITS experiment can be removed and replaced with an auxiliary seal ring. Further, if the auxiliary seal ring has an issue, then it can be removed along with the FMITS-style target and replaced with a target of the pre-FMITS vintage. In this manner, the risk to SNS availability is bounded by the time it takes to replace the target module.

Except for the VLSB, the installation of the FMITS support systems would be accomplished while the beam is active on target; the VLSB replacement must occur during one of the scheduled outages. The impact the VLSB installation would have on the duration of a specific outage is unknown because plans that far into the future have not been formalized.

A separate safety assessment based on the engineering solutions presented in the feasibility study is being released concurrently: it states that the FMITS can be safely installed and operated in the SNS target facility. FMITS project plans call for safety personnel to remain engaged throughout the FMITS project to ensure that the design continues to support this conclusion. As the design evolves, the safety assessment will be kept up to date and revised as necessary to ensure that any needed safety features are incorporated as an integral part of the FMITS design/build process.

A $13.4 million /4 year project plan (including $2.6 M and 1 year contingency) has been developed for a potential FMITS project. This estimate includes the cost of the first FMITS experiment harness and a contribution toward the first two FMITS-style target modules. The schedule is subject to slip only in 6 month increments because of the requirement that the first FMITS target be installed during a semiannual outage.

FUTURE PLANS

The planned work for FY2015 consists of a three-part effort to mitigate the highest-level vulnerabilities identified in the FMITS 30% design review: (1) constructing and initial testing of a double inflatable seal mock-up, (2) addendum to the preliminary safety report (PSR), and (3) transient three-dimensional analysis of off-normal operational events.

3.0 FOA - STRUCTURAL MATERIALS OF POTENTIALLY UNIQUE IRRADIATION RESISTANCE

(Contact: Steve Zinkle, zinklesj@ornl.gov)

This project is exploring the basic radiation resistance of three unique structural materials [high entropy crystalline alloys (HEA), bulk metallic glass (BMG), and MAX phase alloys] that may have the potential for very good resistance to neutron-induced property degradation.

3.1 ION IRRADIATION EFFECTS IN Fe-Ni-Cr-Mn HIGH ENTROPY ALLOY

N.A.P. Kiran Kumar (nimishakavia@ornl.gov), K.J. Leonard, H. Bei, Yanwen Zhang and S.J. Zinkle

OBJECTIVE

The key objective of the present study is to examine the extent of microstructural and mechanical changes produced by irradiation on a specified austenitic HEA, compared to conventional Fe-Cr-Ni FCC alloys. This work provides the initial examination of the fundamental irradiation behavior of an HEA material, thereby giving insight into the potential of this family of materials for nuclear applications.

SUMMARY

In recent years, high entropy alloys (HEA) have attracted significant attention due to their excellent mechanical properties and good corrosion resistance, making them potential candidates for high temperature fusion structural applications. However, there is practically nothing known about their radiation resistance. In the present study, a high entropy alloy of composition 27%Fe-27%Mn-28%Ni-18%Cr, manufactured at ORNL is ion irradiated at room temperature and at 500°C to doses ranging from 0.1 dpa to 10 dpa. Transmission electron microscopy (TEM), scanning transmission microscope with energy diffraction spectrometry (STEM/EDX) and X-ray diffraction (XRD) were used to examine the radiation defects and microstructural changes. Irradiation at 500°C showed evidence of significant solute segregation at grain boundaries and discrete precipitates were observed; precipitation was not observed in the room temperature irradiated samples. The grain boundary precipitates were highly enriched in Cr and Mn. Voids were not observed at any irradiation condition. Nano-indentation tests on the specimens showed a rapid increase in hardness ~40% higher than the unirradiated value at 0.1 dpa and to approximately double the unirradiated hardness at 1 dpa with the irradiation dose at room temperature. The irradiation hardness was less pronounced for 500°C irradiations. The present study provides insight of the fundamental irradiation behavior of HEA material.

PROGRESS AND STATUS

Figure 1Figure 2 show weak-beam dark field and typical bright field TEM images of ion irradiated HEA specimens. The irradiation damage consists of black spots, network dislocations and dislocation loops. However, in the current results dislocation loops dominate the defect microstructure at all irradiation conditions. The diameter of dislocation loops ranging from 1 to 10 nm can be seen in the micrographs. Figure 3(a) summarizes the average loop size variation in HEA and is compared with Fe-Ni-Cr alloys. A qualitative trend of increase in loop size was observed with increasing irradiation temperature and dose. However, the growth of dislocation loop diameter with respect to irradiation temperature and irradiation dose is not very substantial (3 to 4 nm) when compared with other Fe-Ni-Cr alloys. Figure 3(b) shows a comparison of loop density data of irradiated HEA with Fe-Ni-Cr alloys irradiated under similar

conditions. Loop density saturates after exposure to a dose of 1 dpa. Although the uncertainty in loop density measurement is a factor to be considered, it should be noted that the point defects retained in HEAs are around 10^{22}-10^{23} m^{-3}. The observed defect cluster densities of low temperature irradiated HEAs are comparable to the densities of many Fe-Cr-Ni alloys irradiated under similar conditions. Slight variation in defect density could be because some authors separated the black spots and dislocation loops, where in the current study both black spots and dislocation loops are collectively considered as dislocation loops. Relatively high defect density was also observed for the high temperature irradiated specimen. Usually, the increase in irradiation temperature results in decrease in loop density and an increase in loop diameter due to increase in diffusion rate of solute interstitial and vacancies. However, the high dislocation density and limited growth in loop size in current specimens suggest that the diffusion kinetics in HEA's are more sluggish than in conventional Fe-Ni-Cr alloys. In addition, the smaller loop size in HEA suggest that only a small fraction of point defects are trapped in the loops and recombination between vacancies and interstitials is the dominant recovery process in the HEAs.

In general, voids are formed due to accumulation of radiation-induced vacancies into stable cavities. In contrast to conventional Fe-Ni-Cr alloys, the present HEA showed no pronounced void swelling at any irradiation conditions. The fact that no voids were found in current HEA even after high temperature (500^{o}C) irradiation indicated that the HEA has better swelling resistance than conventional austenitic FeCrNi or FeCrMn alloys, which exhibit significant void formation after 10 dpa at this temperature. Considering the average loop radius of each irradiation condition, the loop sink strength of 500°C irradiated samples is around 10^{16} m^{-2} which is relatively high when compared with conventional Fe-Ni-Cr alloys. Dislocation loops being the dominant defect clusters at all irradiation conditions, the series of sinks spread throughout the grain would minimize the excess accumulation of vacancies at each sink thereby will reduce any void formation.

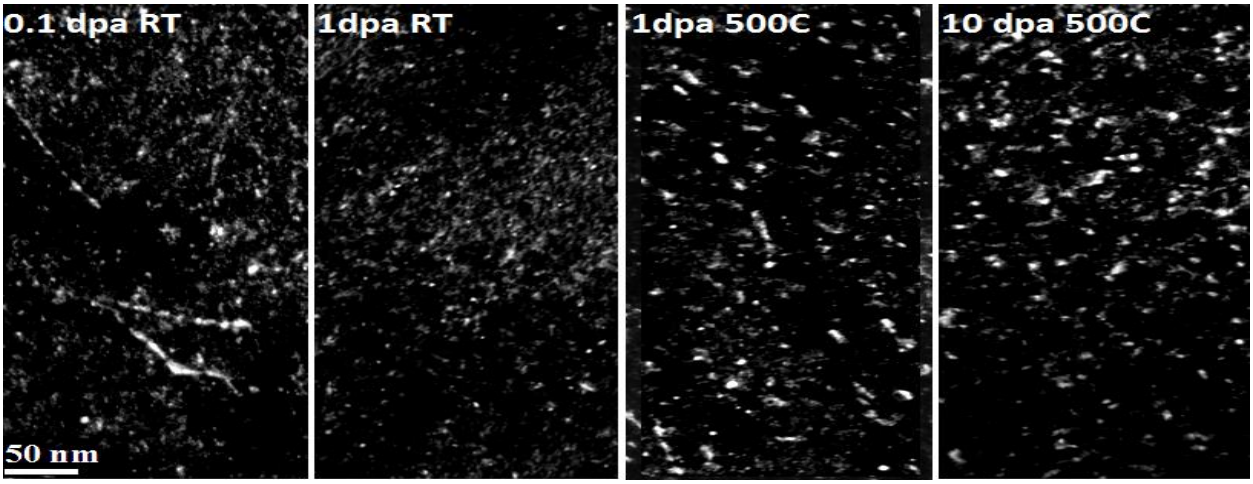

Figure 1. TEM Weak Beam Dark Field (WBDF) images of ion irradiated HEA samples (g= {111})

FUTURE PLANS

Based on the preliminary results obtained from ion irradiation studies, a new set of ion irradiation experiments will be performed at an irradiation temperature of 600°C. This study will be performed in coming months at the ORNL/University of Tennessee ion beam laboratory. Low dose neutron irradiated samples have been shipped to LAMDA. Post irradiation examination including electric resistivity, tensile and nano-hardness testing has been initiated on the neutron irradiated samples. The capsule design work for high dose and high temperature neutron irradiations is in progress.

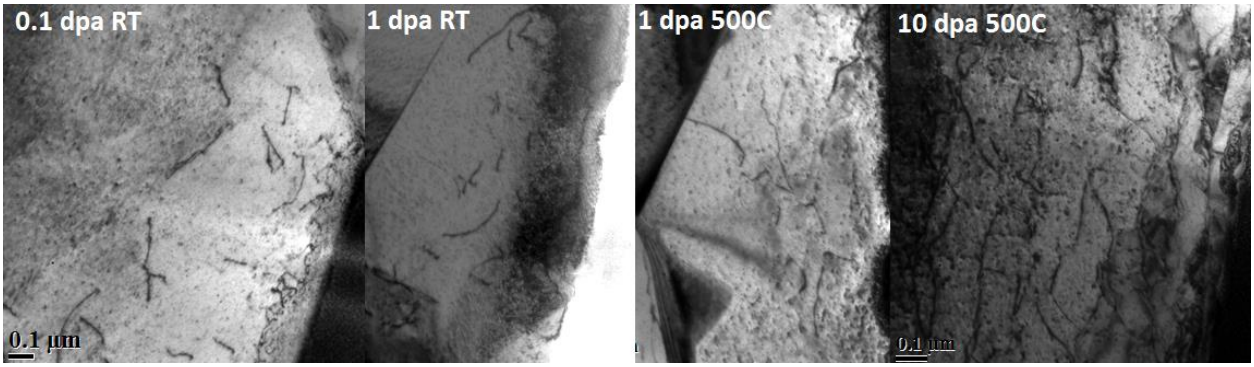

Figure 2. Microstructure showing network dislocations in HEA after ion irradiation

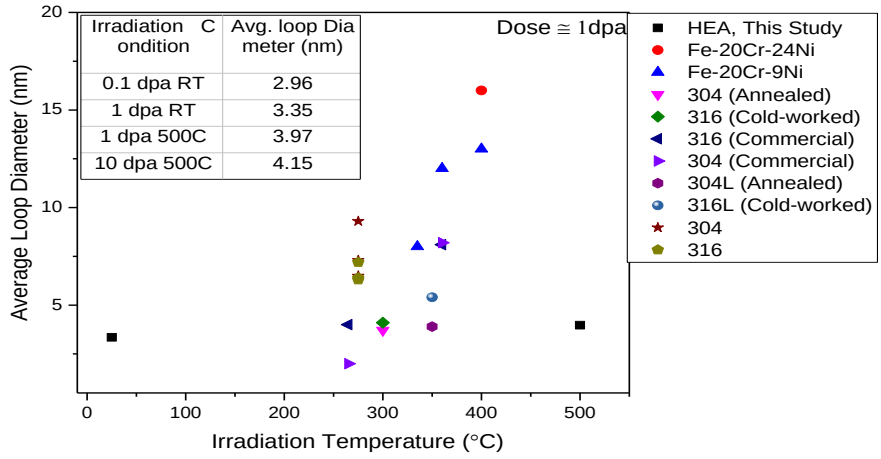

(a)

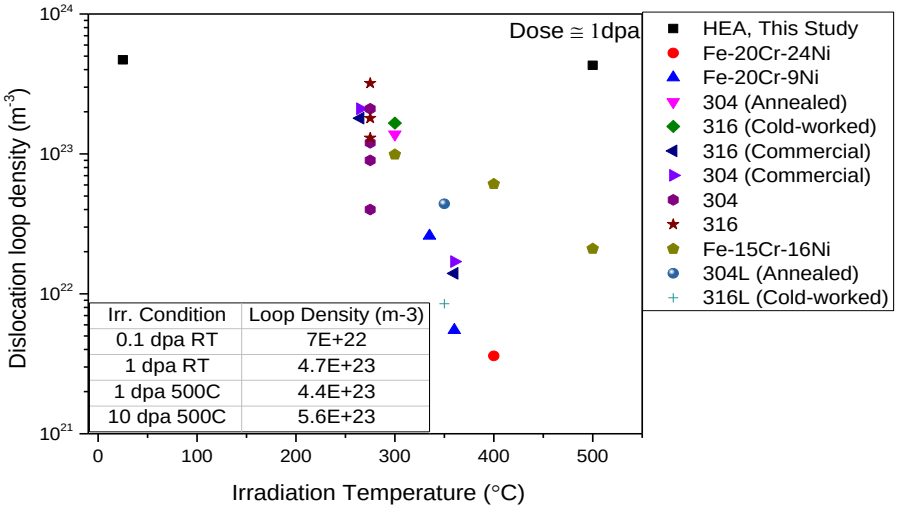

(b)

Figure 3. Effect of irradiation temperature on a) Loop diameter b) Dislocation loop density. (Loop diameter and loop densities of HEA are compared with Fe-Ni-Cr steels).

3.2 ION IRRADIATION EFFECTS IN $Zr_{52.5}Cu_{17.9}Ni_{14.6}$ $Al_{10}Ti_5$ BULK METALLIC GLASS

A.G. Perez-Bergquist, H. Bei, J. Brechtl and S.J. Zinkle (zinklesj@ornl.gov)

OBJECTIVE

The key objective of the present study is to examine the basic radiation resistance of bulk metallic glass structural alloys, as part of exploratory studies on several classes of structural materials that may have the potential for very good resistance to neutron-induced property degradation.

SUMMARY

Bulk metallic glasses (BMGs) exhibiting attractive mechanical properties in as-cast forms are potential candidates for fusion structural applications. However, there is practically nothing known about their radiation resistance. During the past year, samples of a $Zr_{52.5}Cu_{17.9}Ni_{14.6}$ $Al_{10}Ti_5$ BMG were ion irradiated at room temperature and at 500°C to doses ranging from 0.1 dpa to 10 dpa. Transmission electron microscopy (TEM) and scanning transmission microscopy with energy diffraction spectrometry (STEM/EDX) were used to examine the microstructural changes associated with irradiation. Instrumented nanoindentation hardness testing was used to examine the hardness and elastic modulus.

PROGRESS AND STATUS

Bulk metallic glasses (BMGs) are potential candidates for fusion reactor structural material and plasma facing armor components due to their combination of good mechanical properties, high thermal conductivity and ability to be directly cast into a variety of shapes. The lack of long-range crystalline structure is postulated to potentially provide improved radiation resistance and reduced tritium sequestration compared to crystalline alloys. However, there is very limited experimental data on irradiated BMGs.

A series of scoping ion irradiation studies have recently been completed on BAM-11 ($Zr_{52.5}Cu_{17.9}Ni_{14.6}$ $Al_{10}Ti_5$) bulk metallic glass fabricated at ORNL. Initial scoping studies examined as-cast samples ion irradiated with 3 MeV Ni ions to 0.1 and 1 dpa at room temperature and 200°C. Hardness and elastic modulus data generated through nanoindentation tests at 0-1 dpa are shown as a function of depth in

Figure 4. Since the indentation stress and strain fields are sensitive to material properties up to ~5-10 times the indentation depth, the indentation depths of greatest interest are 100-150 nm, where the indentation properties are entirely confined to the ion irradiated region that extends to a depth of ~1.2 micrometer. The hardness and elastic modulus was observed to continuously decrease with increasing dose following room temperature irradiation, whereas no significant change in properties was observed after irradiation at 200°C.

In order to examine whether further mechanical property changes would occur at higher doses during room temperature irradiation, as-cast and stress-relieved (300°C/48 h) samples were ion irradiated to 1 and 10 dpa at room temperature. For both heat-treated and as-cast samples, hardness and modulus dropped for the irradiated specimens as compared to the sample in the unirradiated condition. The drop in hardness following irradiation for both the as-cast and heat-treated samples was about 15%, while the drop in modulus was about 10%. While hardness and modulus values were observed to drop after low dose irradiation (0.1-1 dpa), the irradiation-induced change does not markedly differ between the samples tested at 1 and 10 dpa, indicating a saturation of irradiation damage in the BMG. This indicates that BAM-11 may be resistant to much higher radiation doses than those tested here.

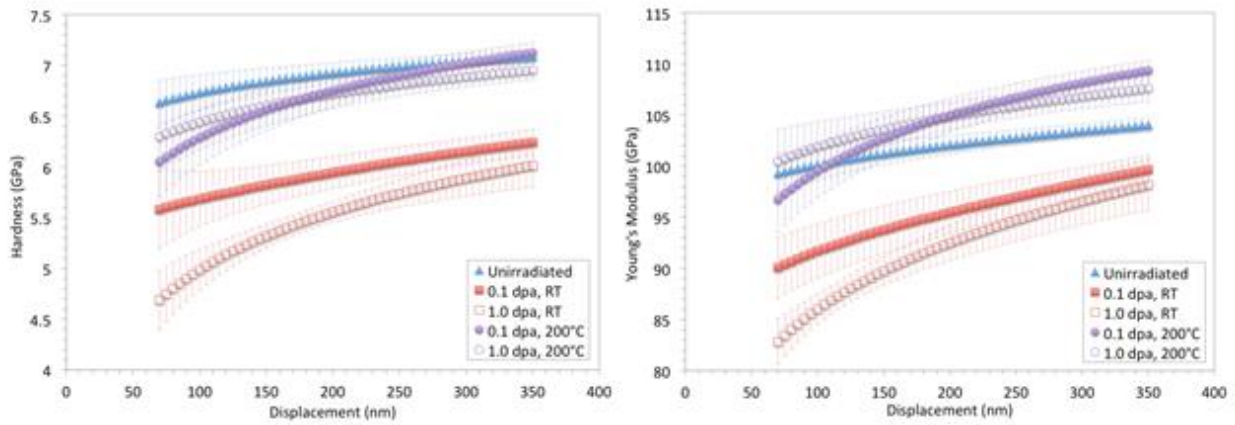

Figure 4. Hardness and elastic modulus data shown as a function of indenter depth for 3 MeV Ni ion irradiated BAM-11 specimens.

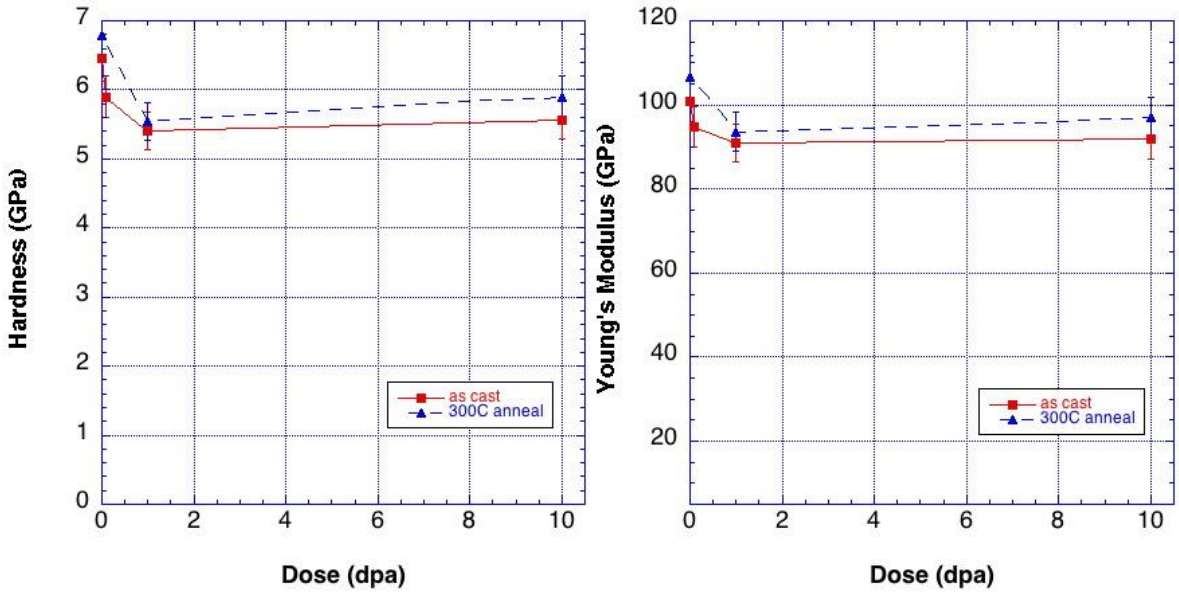

Figure 5. Hardness and elastic modulus vs. irradiation dose for 3 MeV Ni ion irradiated BAM-11 specimens.

Microstructural examination of the unirradiated and irradiated BMG specimens revealed in all cases amorphous and defect-free structures. High resolution transmission electron microscopy (HRTEM) confirmed that no crystallites were present in the samples. Figure 6 shows an example of the microstructure of BMG after irradiation to 1 dpa.

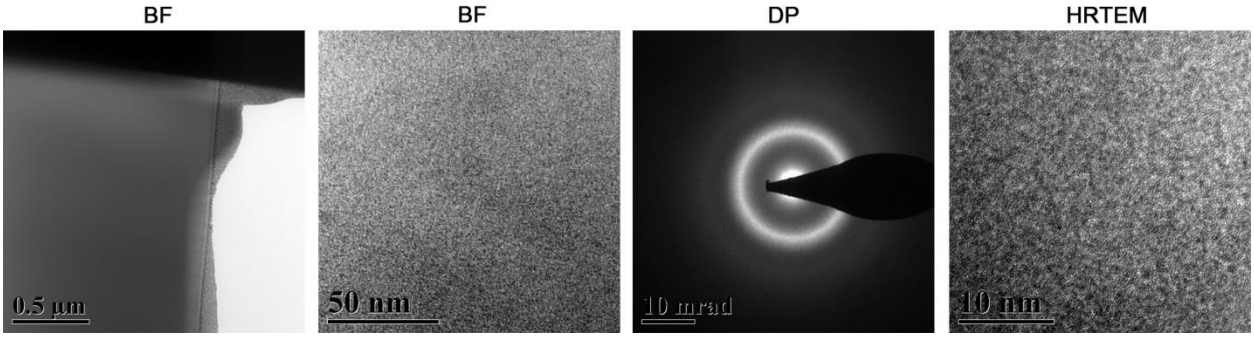

Figure 6. TEM images of BAM-11 BMG irradiated with 3 MeV Ni^{2+} ions to 1 dpa. Included are bright field (BF) images at the surface and at a depth of ~2 microns, a diffraction pattern (DP) of the irradiated region, and high resolution TEM (HRTEM) of the affected region.

FUTURE PLANS

Microstructural, mechanical and physical property measurements will be performed on neutron-irradiated BMG samples to better interrogate irradiation effects in these materials. BMG specimens have been irradiated in HFIR to 0.1 dpa at 70°C, and these low dose neutron irradiated samples have been shipped to the LAMDA facility for examination. Post irradiation examination including density change, elastic modulus, flexural strength and nano-hardness testing has been initiated on the neutron-irradiated samples.

3.3 IRRADIATION EFFECTS IN MAX PHASE CERAMICS

A.G. Perez-Bergquist, C. Shih, Y. Katoh and S.J. Zinkle (zinklesj@ornl.gov)

OBJECTIVE

The purpose of this work is to investigate neutron irradiation effects on MAX phase materials (Ti-Si-C and Ti-Al-C systems).

SUMMARY

Postirradiation characterization has been performed on several MAX phase ceramics following neutron irradiation. Neutron irradiation to 2 dpa at nominal irradiation temperature of 400 °C produced significant strength degradation in the Ti-Al-C material.

PROGRESS AND STATUS

Several room temperature equibiaxial fracture tests on the 2 dpa, 400°C neutron irradiated MAX phase materials were conducted. Severe (~ 90%) strength degradation of the Ti-Al-C was observed. Under the same irradiation conditions, the Ti-Si-C showed only about 30% strength degradation when tested at room temperature. Detailed analysis of the sample of Ti-Si-C MAX phase ceramic (microstructurally Ti_3SiC_2/Ti_5Si_3 dual-phase) following neutron irradiation to 3.4 dpa at 500°C indicated the presence of only titanium silicide (Ti_5Si_3, Ti_3Si_2) and titanium carbide (TiC) phases, with no Ti_3SiC_2 phase detected. Further microstructure observation using a scanning electron microscope is underway in order to determine the root cause of the strength degradation.

The high temperature (up to 1400°C) equibiaxial fracture test fixture and the load train components machining are complete. Several high temperature equibiaxial fracture tests utilizing non-irradiated samples were successfully conducted. This test setup will be used to determine the ductile to brittle transition temperatures (DBTTs) of the two MAX phase materials used in the study and to evaluate whether radiation caused any change in the DBTTs.

A focused ion beam (FIB) was used to prepare a transmission electron microscope (TEM) sample of a Ti_3SiC_2/SiC composite. The sample was prepared via a tape calendaring process and was pressed and heated between two SiC plates at 1425°C at 30 to 40 MPa applied pressure for 2 hours. Afterwards, the sample was neutron irradiated to 5.0 dpa at 800°C in HFIR. As reported in the 2013 annual report, the mechanical properties of this joint showed a moderate degradation due to neutron irradiation (16% drop in shear strength for the Ti_3SiC_2/SiC joints and no change for the Ti_3SiC_2/Ti_5Si_3 joints). BF imaging was used to look at defect structures in grains, which showed evidence of black spot damage as well as stacking faults. Small microcracks were also noticed throughout. Diffraction showed that samples retained their crystalline nature, and X-ray energy dispersive spectroscopy (EDS) was performed in scanning TEM (STEM) mode to help distinguish between small Ti_3SiC_2 and SiC grains. Selected TEM micrographs of the material are shown in Figure 7.

A paper summarizing the microstructural effects of neutron irradiation in the tested MAX phase materials (both 5.0 dpa, 800°C Ti_3SiC_2/SiC samples and 3.4 dpa, 500°C Ti_3SiC_2/Ti_5Si_3 samples) is in preparation. It is tentatively entitled “Microstructural Effects of Neutron Irradiation in Ti_3SiC_2”.

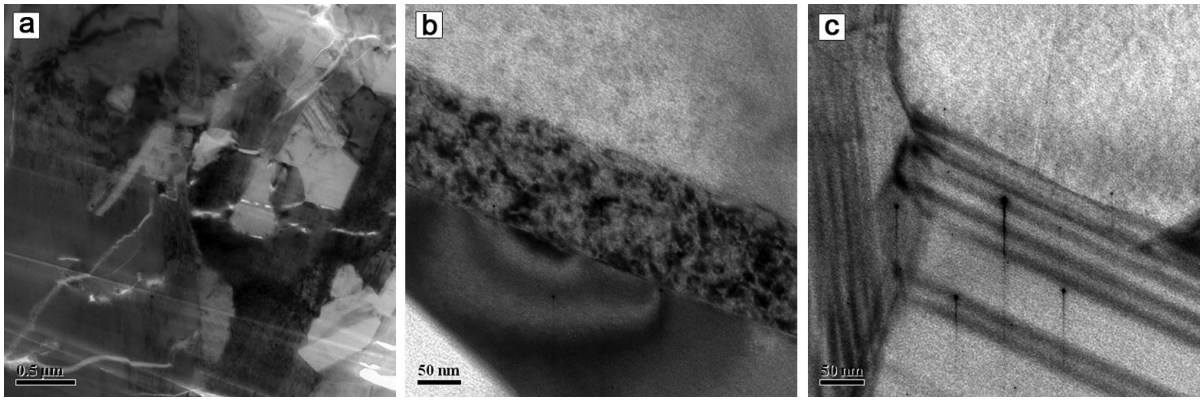

Figure 7. Defects in MAX phase grains irradiated to 5.0 dpa at 800°C. a) Microcracking. b) Black spot damage. c) Stacking faults. Notice the change in magnification between a and b, c.

FUTURE PLANS

Microstructural, mechanical and physical property measurements will be performed on neutron-irradiated MAX phase samples to better interrogate irradiation effects in these materials. The specimens have been irradiated in HFIR to 2, 6, and 10 dpa at 400, 700, and 1000°C, and all the 2 dpa irradiated samples have been shipped to the LAMDA facility for examination. Post irradiation examination will include density change, elastic modulus, flexural strength, XRD, thermal expansivity, thermal conductivity, and electrical resistivity.

4.0 ADVANCED STEELS

4.1 FOA – DEVELOPMENT OF ODS FeCrAl FOR FUSION REACTOR APPLICATIONS

B. A. Pint (pintba@ornl.gov), D. T. Hoelzer, K. A. Unocic and S. Dryepondt

OBJECTIVE

The dual coolant (He and Pb-Li) system is the leading U.S. blanket concept for DEMO. Oxide dispersion strengthened (ODS) ferritic alloys are candidate structural materials due to their superior high-temperature mechanical properties and radiation tolerance. However, conventional ODS Fe-Cr alloys have not shown good corrosion resistance in Pb-Li. The objective of this project is to develop an ODS Fe-Cr-Al alloy with improved compatibility with Pb-Li above 550°C, while retaining the inherently attractive properties of ODS alloys.

SUMMARY

In the second year of this project, prior results on alloy and oxide chemistry were incorporated into fabricating the first batch of new ODS FeCrAl alloys. The project focused on Fe-12Cr-5Al compositions with three different oxide dispersions: Y_2O_3 co-doped with ZrO_2, HfO_2 or TiO_2. The microstructure and the tensile properties were evaluated before and after ageing at 800-1200°C. The alloys were reasonably stable at 800°C. Creep testing was performed at 800°C and the alloys with ZrO_2 and HfO_2 showed excellent creep rupture strength. Compatibility studies with Pb-Li are in progress. The initial results indicated less mass loss for the Y_2O_3-ZrO_2 alloy, similar to prior results for PM2000.

PROGRESS AND STATUS

Three alloys with a base composition of Fe-12Cr-5Al were fabricated with oxide dispersions of Y_2O_3-HfO_2 (125YH, 0.17wt%Y, 0.68%Hf), Y_2O_3-ZrO_2 (125YZ, 0.18wt%Y, 0.30%Zr) and Y_2O_3-TiO_2 (125YT, 0.16wt%Y, 0.20%Ti). Figure 8 shows representative images of the ODS microstructure as-extruded and after annealing. Some defects are present including oxide stringers and voids but a fine dispersion of oxides is evident at higher magnification. Considerable effort has gone into identifying the precipitate chemistry and phase constituents using high resolution transmission electron microscopy, Figure 9. The tensile properties were measured from room temperature to 800°C, Figure 10. The 125YT alloy showed the highest room temperature and 400°C ultimate tensile strength (UTS) and PM2000 (extruded using the same process and not recrystallized) the lowest. However, the 125YT also had the lowest ductility, while PM2000 had the highest ductility at all temperatures compared to the new ODS alloys, Figure 10b. For comparison, the PM2000 data sheet properties from Plansee are shown in Figure 10. Properties are differentiated for small grain and large (recrystallized) grain commercial PM2000. The tensile properties correlated with the as-extruded hardness data shown in Figure 11. In order to evaluate the stability of the as-extruded microstructures, ageing experiments were conducted at 800-1200°C and hardness was used as an indication of the microstructure stability, Figure 11. The 125YT alloy showed the largest drops in hardness, while PM2000 showed the least changes. Most of the alloys showed minimal changes after 1000 h at 800°C, which is a good indication for the proposed first wall application.

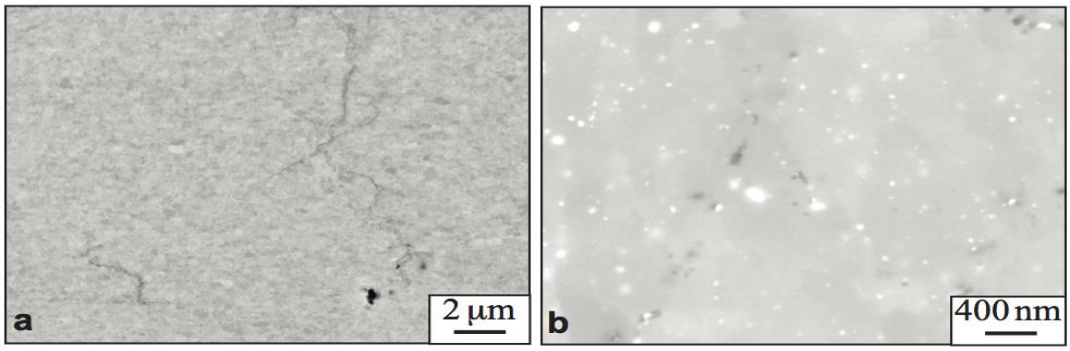

Figure 8. SEM backscattered electron images of (a) 125YT after extrusion and (b) 125YH after annealing for 1000h at 800°C

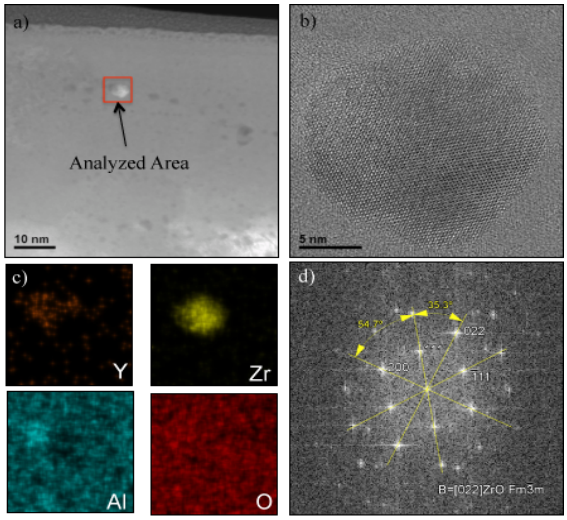

Figure 9. a) STEM HAADF image of the 125YZ as-extruded (lift-out FIB) microstructure. b) High resolution BF-STEM of the Zr-rich particle (from the area marked in a) identified as ZrO using c) EDS maps and d) FFT.

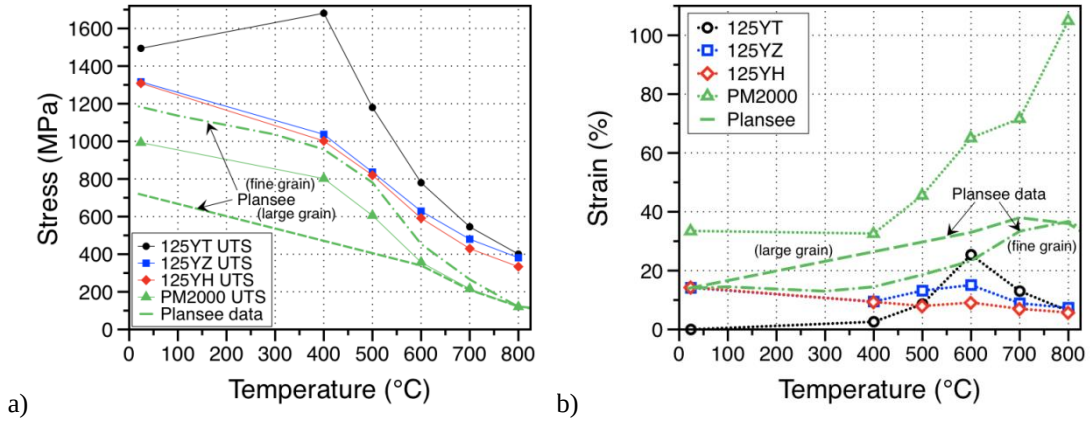

Figure 10. Tensile properties of the ODS FeCrAl heats as a function of test temperature. (a) ultimate tensile strength and (b) total elongation. Data sets from Plansee for PM2000 with two different grain sizes are shown for reference.

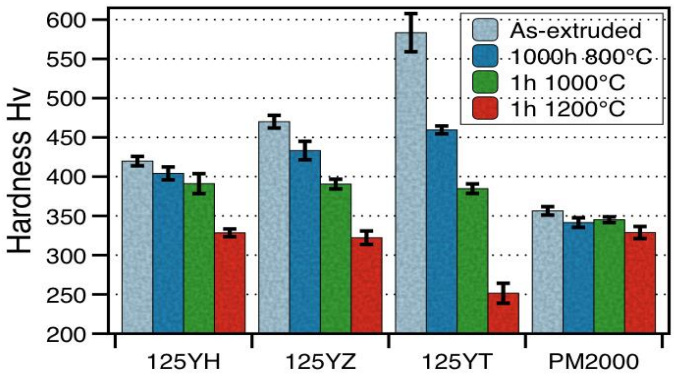

Figure 11. Average Vickers hardness values as extruded and after various anneals. One standard deviation is shown for each bar.

The most interesting results were the creep properties of the new alloys, this time compared to recrystallized PM2000 (unrecrystallized PM2000 failed after 10 h at 60 MPa), Figure 12. The load was increased on the PM2000 specimen until failure occurred quickly at 90 MPa. A remarkably better creep resistance was observed for the 125YH specimen with the co-addition of Hf. A lifetime over 1200 h was observed with a load of 100 MPa. Under the same conditions, a 125YZ specimen has reached ~1100 h. These results support data in the literature suggesting that co-doping with Zr or Hf is beneficial, presumably due to precipitates forming on the alloy grain boundaries and inhibiting grain boundary sliding during creep. In general, the mechanical properties of these new ODS alloys benefit from the low (950°C) extrusion temperature, again supporting prior work on ODS FeCrAl showing a benefit of lowering the extrusion temperature from 1150 to 1050°C.

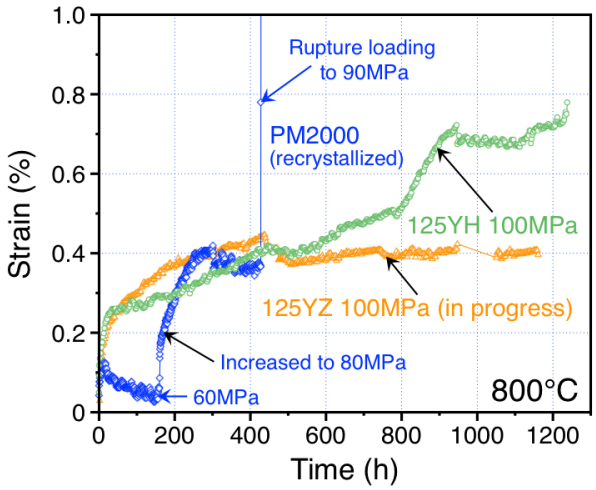

Figure 12. Strain as a function of exposure time for ODS specimens tested at 800°C.

Two of the new ODS alloys have been evaluated in PbLi and the third (125YT) is currently in test. Coupons were exposed isothermally at 700°C for 1000 h in individual welded shut Mo capsules. Figure 13 shows the mass loss for 125YH and 125YZ compared to other ODS materials and cast FeCrAlY specimens. Without an Al addition, the mass losses are much higher for the ODS FeCr specimens, 14YWT and ODM401, similar to prior results for Grade 92 steel (9Cr-2W), which is limited to < 500°C in flowing Pb-Li due to the high solubility of Fe and Cr in the liquid. With Al present in the wrought or ODS FeCrAl specimens, a $LiAlO_2$ layer formed on the specimens from O impurities in the Pb-Li (200-400 ppmw as cast) and this layer inhibited dissolution into the liquid metal, Figure 14. The first year results for cast/wrought FeCrAlY showed the lowest mass losses with alloys containing 5%Al, with higher mass losses observed for 4%Al alloys, as shown in Figure 13. While 125YZ and 125YH have similar Al contents (4.8 wt%), they showed much different mass change behavior. This result may be anomalous

as some variability has been observed in this type of experiment. One concern is that Al tied up in oxides in the ODS alloys is not available to form a protective scale in this environment. Thus, the effective Al content in the ODS alloys is lower than for a comparable Al content in a wrought alloy. It is also possible that the Hf and Zr additions are affecting performance. XRD confirmed that both alloys formed $LiAlO_2$ after exposure. EPMA line profiles in the substrate showed <1 at.%Al gradient below the $LiAlO_2$ reaction product in both alloys. In general, the small mass change for 125YZ supports the general strategy that a low Cr ODS FeCrAl can be protective in Pb-Li.

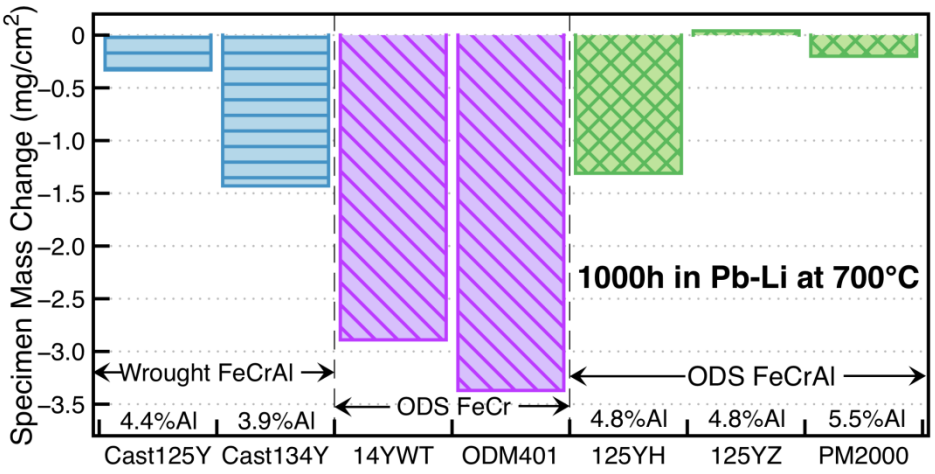

Figure 13. Specimen mass change for alloy specimens exposed for 1000 h at 700°C in static Pb-Li.

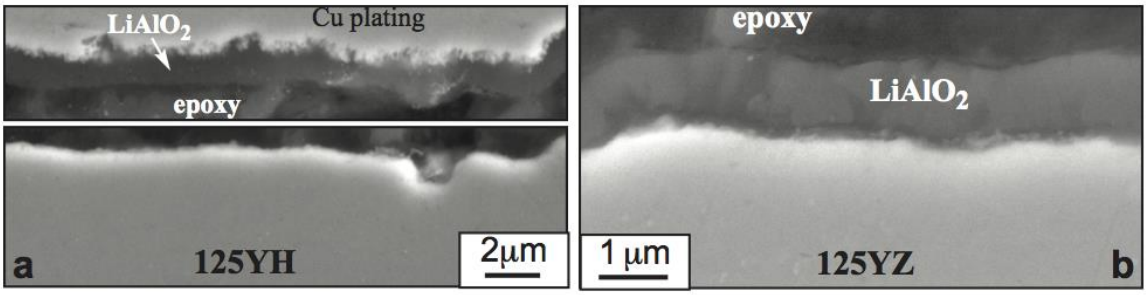

Figure 14. Specimen mass change for alloy specimens exposed for 1000 h at 700°C in static Pb-Li.

FUTURE PLANS

During the coming year, 1-2 new powder compositions will be purchased in order to further optimize the microstructure and properties by adding Hf and/or Zr to the powder rather than adding as an oxide. The mechanical properties, ageing behavior and isothermal PbLi compatibility will be evaluated. With the successful operation of a PbLi loop this year, another goal will be to expose these new ODS materials to flowing PbLi.

4.2 DEVELOPMENT OF ADVANCED RAFM STEELS

L. Tan (tanl@ornl.gov), Xiang Chen

OBJECTIVE

Traditional RAFM steels suffer noticeable strength reduction at temperatures above ~500°C, which limits their high temperature applications. The objective of this project is to develop advanced RAFM steels having optimized alloy composition and thermomechanical treatment to produce high density of stable nanoprecipitates for superior high temperature performance.

SUMMARY

A new RAFM steel has been designed to favor the formation of MC (M = metal) carbides based on our recent study showing superior stability of TaC over TaN and VN nanoprecipitates under thermal aging, creep testing, and Fe^{2+} ion irradiation at 500°C conditions. An experimental lab heat (~0.45 kg) of the new alloy has been fabricated in two conditions, i.e., conventional normalization and tempering (N&T) and thermomechanical treatment (TMT) conditions. The selected TMT condition was based on a TMT study conducted on Grade 92, which has an excellent balance between tensile strength and Charpy impact resistance. The tensile data on the new alloy in the two conditions exhibited significantly improved strength with decent ductility as compared to Eurofer97 at testing temperatures up to 800°C. Additionally, microstructural characterization of the high dose Fe^{2+}-irradiated TaC, TaN, and VN samples (up to ~246 dpa at 500°C) has been initiated.

PROGRESS AND STATUS

The stability of MX-type nanoprecipitates TaC, TaN, and VN has been evaluated by means of thermal aging at 600 and 700°C for up to 5000 h, creep testing at 600°C, and Fe^{2+} ion irradiation at 500°C and up to ~49 dpa. Transmission electron microscopy (TEM) in both conventional and scanning modes was primarily used to characterize the evolution of the nanoprecipitates. The results indicate different levels of stability of the nanoprecipitates under the three types of experimental conditions. Selected particle degradation modes, e.g., dissolution, growth, re-precipitation, and fragmentation, were observed for the nanoprecipitates. Basically the carbide (TaC) exhibited superior stability over the nitrides (TaN and VN). The results have been reported in two recent papers. The same type of TEM characterization has been initiated on the high dose (up to ~246 dpa) Fe^{2+}-irradiated samples. Preliminary results from the TaC sample indicated the introduction of a few ultrafine cavities and noticeable dissolution of TaC nanoprecipitates under high dose irradiation at 500°C. Further characterization including the TaN and VN samples are in progress.

Due to the observation of inferior stability of nitrides as compared to carbides, new RAFM steels have been developed to primarily favor the formation of MC-type carbides, with the assistance of computational alloy thermodynamics. An experimental lab heat (~0.45 kg) has been fabricated using vacuum arc melting and drop casting. Half of the ingot was subjected to traditional normalization and tempering (N&T) heat treatment. In the meantime, four types of thermomechanical treatment (TMT) conditions, involving the application of warm rolling and tempering, were developed using Grade 92 (9Cr FM steel) due to the limited material of the new alloy. Tensile and Charpy impact tests were conducted on the TMT-ed Grade 92 samples, which led to the selection of a TMT condition that favored a balanced strength and Charpy impact resistance. The down-selected TMT was applied to the other half of the new alloy ingot. Figure 15 exhibits the temperature-dependent yield strength and total elongation of the new RAFM steel (TT1) in the N&T and TMT conditions at testing temperatures up to 800°C. The data for Eurofer97 are included for comparison. The new alloy has noticeably higher yield strength than Eurofer97 at the test temperatures. It also has adequate total elongation considering the significantly smaller type SS-3 specimens used in this work. [The SS-3 has only ~5.9% of the gauge cross-section of the Eurofer97 specimens as shown in the Figure 15 inset.] The new alloy in the TMT condition exhibited an excellent

combination of strength and ductility.

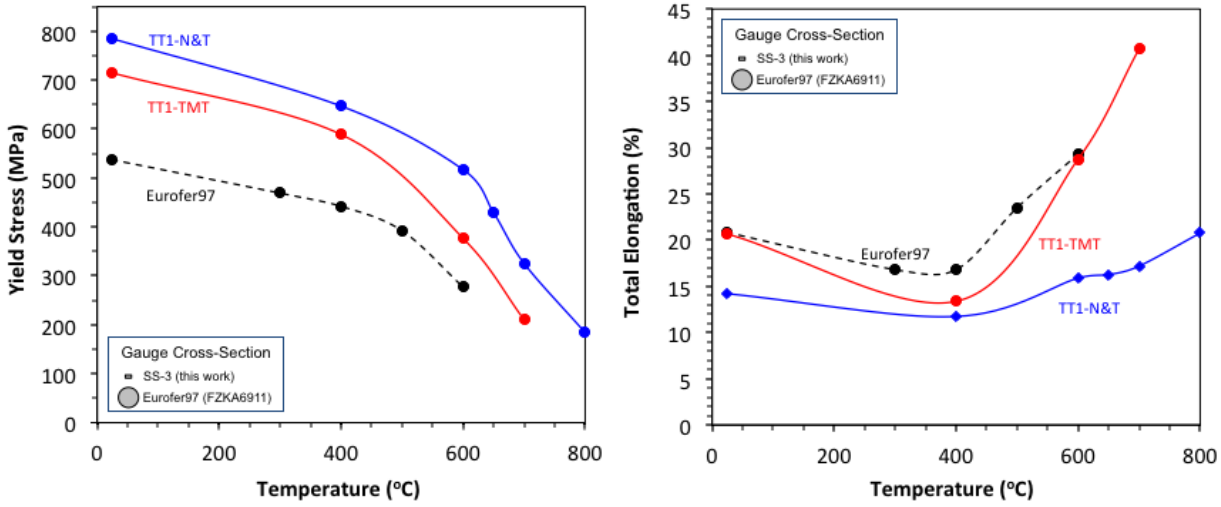

Figure 15.Temperature-dependent yield strength and total elongation of a newly developed RAFM steel TT1 in the N&T and TMT conditions as compared to Eurofer97 at testing temperatures up to 800°C.

Electron backscattered diffraction (EBSD) was used to characterize the TMT specimens of the processed Grade 92. Figure 16 shows an inverse pole figure (IPF) of the selected TMT condition, with the colors denoting the orientation of the grain components. Regular prior-austenite grain structures, and martensite packets and blocks are deformed by the TMT, leading to increased interweaving of the microstructures. This may explain the TMT-induced improvements in ductility and Charpy impact resistance.

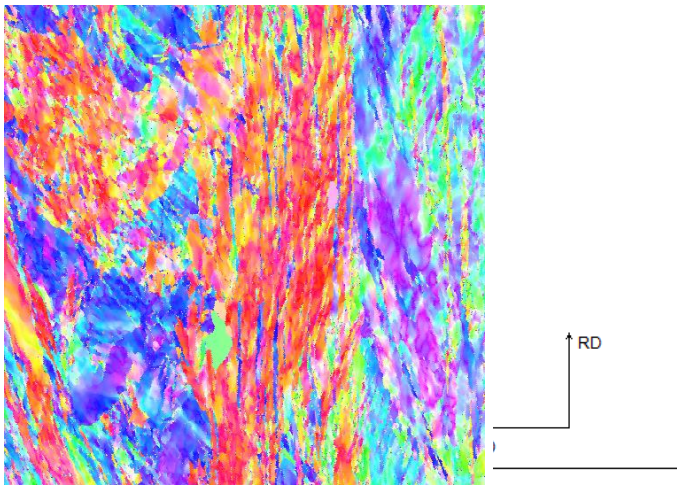

Figure 16. EBSD IPF map (100×100 μm^2) of the Grade 92 sample subjected to the selected TMT.

FUTURE PLANS

Development of the new RAFM steels will continue. The creep resistance will be screened. Additionally, neutron irradiation of the TaC, TaN, and VN containing samples in HFIR at 300, 500, and 650°C for up to about 20 dpa has recently been completed. Post-irradiation examination (PIE) of selected samples from these experiments, together with the high dose Fe^{2+}-irradiated samples, will be conducted.

4.3 IRRADIATION EFFECTS IN F82H

M. Ando (JAEA, andom@ornl.gov), H. Tanigawa (JAEA), Y. Katoh, and L.L. Sneed

OBJECTIVE

Higher-dose irradiation data on RAFM is needed for the design of a fusion DEMO reactor. However, mechanical property data for RAFM after high-dose neutron irradiation, above 80 dpa, are not available. The objective of this collaborative work in the DOE-JAEA program was to disassemble ten tensile specimen holders from the JP28&29 HFIR irradiation capsules (~85 dpa; 44 reactor cycles) and perform Vickers hardness measurements on 573 K-irradiated SS-J3 specimens.

SUMMARY

Ten tensile specimen holders from HFIR irradiation experiments JP28 and JP29 were successfully disassembled in the ORNL 3025E hot cell facility. Some holders needed to be cut along corners of the holder because specimens could not be easily pushed out of the holder. All tensile specimens from the disassembled holders were recovered and identified. Vickers hardness was measured on some of the tensile specimens irradiated at 573 K.

PROGRESS AND STATUS

Table 2 summarizes the results of disassembly of JP28&29 tensile specimen holders. Some holders were cut along the corners of the holder in hot cell if they could not be disassembled easily.

Table 2. Disassembly results for JP28&29 tensile holders

No	Holder No.	Irrad. Temp. (K)	Dose (dpa)	Cut	SS-J3	APFIM/MMPC	Passive TM
				Number of specimens (missing), [broken]			
1	JP28 #7	673	85.4	1	16 (0)	17 (0)	8 [0]
2	JP28 #9	773	81.8-83.4	2	16 (0)	16 (0)	8 [0]
3	JP29 #7	573	85.9-86.8	-	16 (0)	16 (0)	8 [0]
4	JP29 #10	573	76.9-79.9	1	17 (0)*	17 (0)	8 [0]
5	JP29 #13	573	46.9-52.9	3	16 (0)	16 (0)	8 [0]
6	JP29 #2	673	45.7-51.8	1	16 (0)	16 (0)	7 [1]
7	JP28 #3	573	66.8-70.8	-	16 (0)	13 (3)	7 [1]
8	JP28 #1	673	41.7-47.9	1	16 (0)	15 (1)	7 [1]
9	JP29 #3	773	58.7-63.7	1	16 (0)	15 (1)	8 [0]
10	JP29 #12	573	58.7-63.7	-	16 (0)	14 (2)	8 [0]

* Including 3 SSJ2 specimens

After disassembly of holders, Vickers hardness measurements were performed in the hot cell on tensile specimens irradiated in position 7 of JP29 capsule. The materials of tensile specimens in this position were F82H IEA heat, F82H Modification-3 and 1.4% Ni doped F82H, which were provided by JAEA. Currently, Vickers hardness measurements were completed for eleven SS-J3 specimens. The irradiation hardening data are shown in comparison to data from the JP25, 26 and 27 capsules in Figure 17. It is believed that the irradiation hardening has almost saturated at 80 dpa. On the other hand, the 1.4% Ni doped F82H showed strong hardening for irradiation below 573 K . However, the hardening of 1.4% Ni doped F82H tended to decrease at 80 dpa irradiation. Moreover, these results need to be compared to results from specimens from another holder which has a similar irradiation condition. Additionally, 50 dpa irradiation data for F82H will be also obtained in the future from recently completed high dose (50 dpa) rabbit capsule irradiation experiments with similar materials.

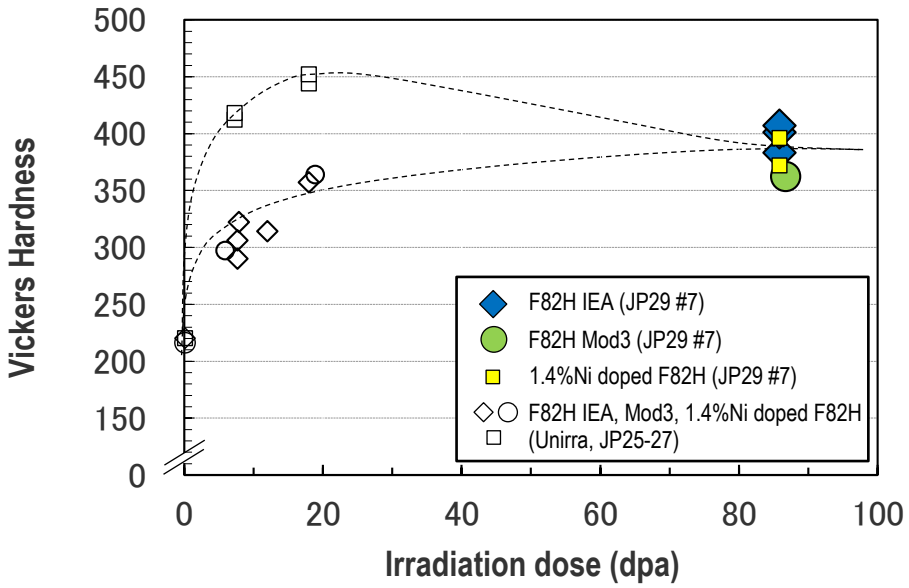

Figure 17. Dose dependence of Vickers hardness for F82H IEA, F82H Mod3 and 1.4%Ni doped F82H irradiated at ~573 K in HFIR.

FUTURE PLANS

The hardness testing will be completed on all SS-J3 specimens prior to tensile testing for JP28&29 in FY 2015, and then the tensile tests will be started. Disassembly of remained JP28&29, JP30&31 and several rabbit holders will be also started. In addition, the low-cycle fatigue tests of the remaining RB15J irradiated material will be continued in FY2015.

4.4 INVESTIGATION OF 9Cr-ODS RADIATION TOLERANCE

C. M. Parish (parishcm@ornl.gov), T.-S. Byun, Y. Katoh, and S. Kondo (Kyoto University)

OBJECTIVE

Irradiation effects in nanostructured ferritic alloys (NFAs) and oxide dispersion strengthened (ODS) steels are not well understood. In particular, high-temperature irradiation effects have not been studied but will be important to determine if materials designed for improved resistance to high-temperature creep will be suitable for an irradiation environment. The objective of this task is to begin characterizing the response of NFA/ODS alloys, particularly the new 9Cr-based alloys, to high-temperature/high-dose irradiation.

SUMMARY

Samples of conventional reduced activation ferritic/martensitic (RAFM) steel F82H and 9Cr ODS steel 9YWTV were ion-irradiated at 650°C. Subsequent electron microscopy examination was used to compare the irradiated regions to unirradiated regions of the specimens. Gross differences were not apparent between the deep (unirradiated) and shallow (irradiated) regions of the material, which indicates most of the irradiation-induced defects (vacancies, interstitials, dislocation loops, etc.) either recombined, migrated to sinks, or were annealed out at the high temperature. Analytical scanning transmission electron microscopy (STEM) indicated a wide range of precipitates were present in the irradiated and unirradiated regions, including large carbides, small carbides, and nanoclusters (NCs). NCs appeared to coarsen, and suffer slight changes in chemistry during irradiation.

PROGRESS AND STATUS

The ORNL nanostructured ferritic alloy 9YWTV-PM1 (Fe–9Cr–2W–0.4Ti–0.2V–0.12C–0.3Y_2O_3) was subjected to heavy-ion irradiation (6.4 MeV Fe, 1.5×10^{21} ions/m^2, ~150 dpa peak, ~2 μm range) at 650°C, using the DuET facility at Kyoto University. This temperature was chosen as near the most extreme expected for future ferritic steel applications in first wall or other high neutron-damage environments. STEM samples were prepared by focused ion beam (FIB) liftout from the irradiated bars and examined in a Titan ChemiSTEM advanced analytical electron microscope at North Carolina State University.

STEM imaging and large-area high-speed STEM-X-ray mapping, coupled with multivariate statistical analysis (MVSA) datamining, provides comprehensive characterization of the entire depth of the irradiation (Figure 18). As expected at this high temperature (650°C), little traditional radiation damage is observed, because defects such as black spots and dislocation loops were annealed away during the irradiation. Large (~100 nm) Cr-W-rich carbides (cyan in Figure 18c) are visible both above and below the irradiation depth, indicating they were likely present prior to the irradiation. Similarly, smaller Ti-carbides (yellow) and Ti-Al-oxides (green) are present in both the irradiated and unirradiated regions. (The Al-oxides are surprising given the non-intentional addition of Al to the alloy).

Higher resolution mapping (Figure 19) of both irradiated (shallow) and unirradiated (deep) regions show the individual nanoclusters, which are very Ti-Y rich. A denser dispersion of smaller NCs is observed in the unirradiated specimen. It is possible (indeed, likely) that high-temperature irradiation causes coarsening of the NCs, which would be consistent with the observations in (Figure 19. However, because it is also possible that if the irradiated foil region was thicker than the unirradiated foil region, smaller NCs would be rendered invisible due to the finite-foil-thickness effects, so coarsening cannot yet be concluded with 100% certainty; further TEM experiments (EFTEM imaging, foil thickness measurements) and atom probe tomography (APT) would be needed for confirmation of this result. However, it is likely that the NCs are indeed coarsening with

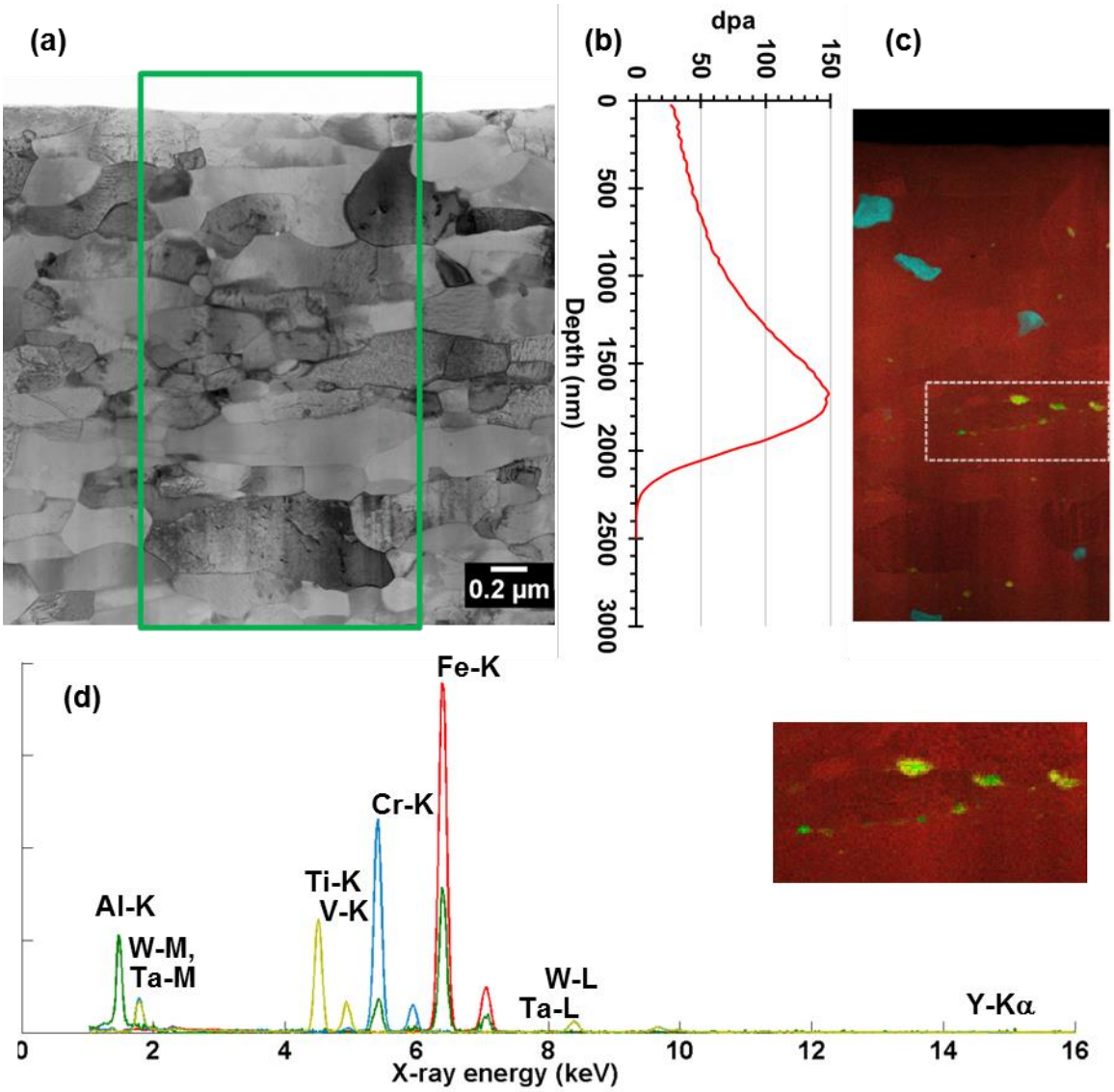

Figure 18. Large area X-ray mapping of Fe-ion irradiated 9YWTV. (a) bright field STEM (b) Calculated dpa profile. (c) False-colored multivariate statistical analysis (MVSA) score images of X-ray map marked by green box in (a). (d) MVSA loading spectra associated with the score images in (d). Inset is detail of the white boxed region, showing small features. Red: matrix (Fe-Cr). Cyan: carbides (Cr-W-C). Yellow: carbides (Ti-Cr-C). Green: oxides (Al-Ti-O).

irradiation. Also, a slight Al-K peak is observed in the MVSA loading spectrum for the irradiated NCs, which has been previously observed in 14YWT alloy and would be entirely invisible without the application of the advanced data analysis and high-efficiency hardware used here.

FUTURE PLANS

We are comparing the data to identically-irradiated F82H and 14YWT. Further characterization will include TEM, EFTEM, and possibly APT for quantitative NC sizing.

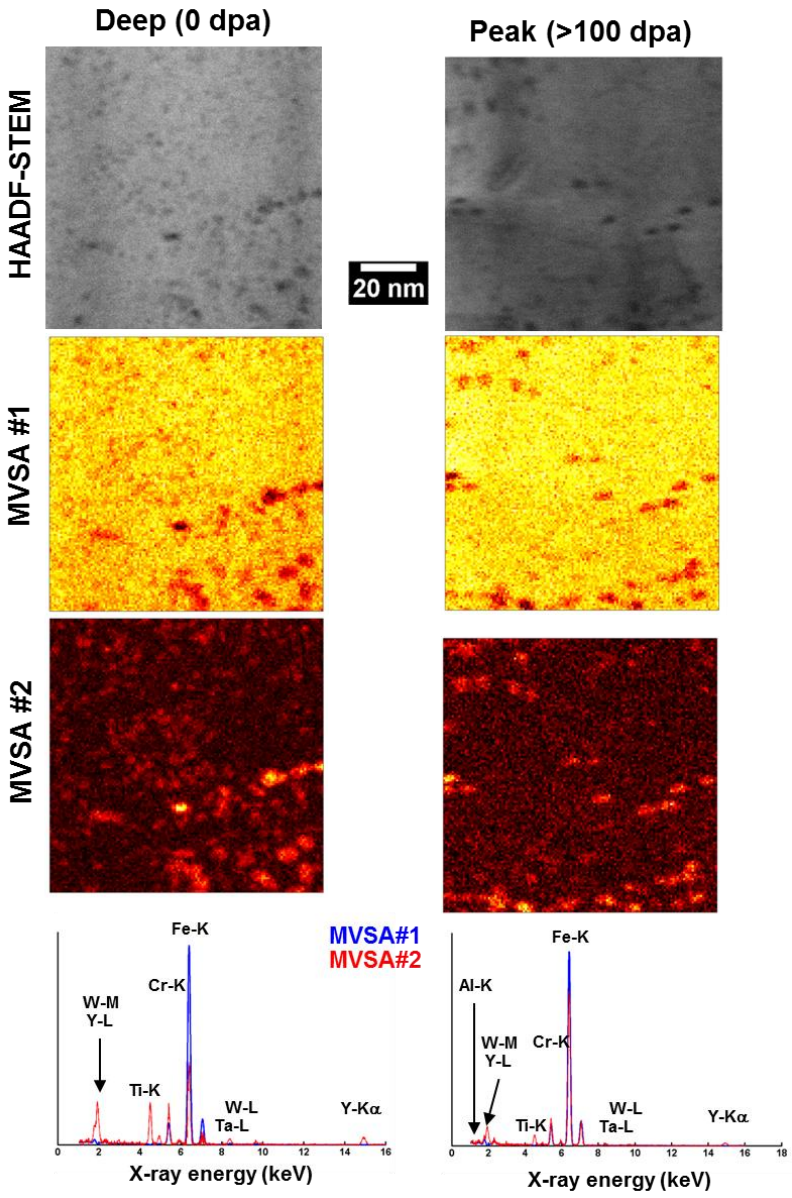

Figure 19. Left column, unirradiated. Right column, near-peak irradiated (~1500 nm depth, >100 dpa). HAADF: high-angle annular dark field. MVSA: multivariate statistical analysis.

ACKNOWLEDGEMENT

The authors acknowledge the use of the Analytical Instrumentation Facility (AIF) at North Carolina State University, which is supported by the State of North Carolina and the National Science Foundation.

4.5 FOA - FRICTION STIR WELDING AND COMPUTER MODELING OF ODS STEELS AND ADVANCED FERRITIC STRUCTURAL STEELS

Z. Feng (fengz@ornl.gov), W. Tang, X. Yu, G. Chen, D. Hoelzer, and L.T. Tan

OBJECTIVE

Friction stir welding (FSW) is an advanced technology, a solid phase thermal-mechanical process, used to join nuclear structural alloys. This project aims to develop FSW technology to join oxide dispersion strengthened (ODS) steels, nanostructured ferritic alloys (NFAs), reduced-activation ferritic/martensitic (RAFM) steels, and dissimilar metals joining between ODS/NFAs and RAFM steels. The specific goals include FSW parameters study and process development, fundamental understanding of weld region strengthening phase stability, bonding mechanisms between different steels, as well as FSW thermal-mechanical coupled computer modeling.

SUMMARY

Our research focused on (1) developing FSW process to produce defect free joints between similar and dissimilar ODS and RAFM steels, (2) investigating FSW heat input and post weld heat treatment (PWHT) effects on joint microstructures and properties, (3) understanding the effect of the extreme thermal and deformation conditions of FSW on the nano oxide strengthening particles in MA956 and 14YWT/14WT ODS alloys, (4) thermal-mechanical computer modeling of FSW process to obtain temperature and strain rate fields, and (5) producing RAFM/ODS and RAFM/9Cr FSW joints for future study. Major findings included the development of a PWHT schedule to produce uniform microstructure and a homogeneous hardness distribution in the weld region that is identical to base metal. Initial atom probe maps of FSWed MA956 revealed complete dissolution of the nano oxide particles, which has major implications on the fundamental understanding the stability of nano-oxide particles under extreme thermal-mechanical process conditions, as well as on potential solutions to restore the creep strength in the weld region. Preliminary computer modeling showed reasonable predictions of temperature fields during FSW.

PROGRESS AND STATUS

Friction Stir Welding and Post Weld Heat Treatment of Similar and Dissimilar Materials

Previously, defect free FSW joint were made with RAFM steels, using certain set of process parameters. Additional RAFM steel FSW joints were made with different parameters in an attempt to better understand effects of FSW conditions on joint microstructures. Combining all conditions, a clear relationship has been observed between the FSW tool rotation rate and the power input, see Figure 20. Power input is a reasonable indictor of the

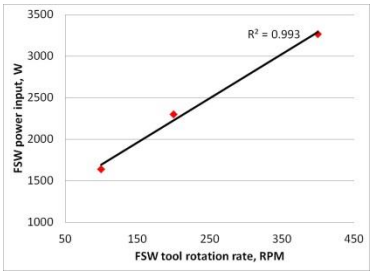

Figure 20. Relationship of FSW power input and tool rotation rate

FSW temperature in the stir zone, and temperature is the major factor affecting microstructures, properties and performance of welded structures. On dissimilar materials joining, we have successfully joined, in butt joint configuration, 14YWT, an oxide dispersion strengthened ferritic alloy, and an experimental ferritic/martensitic (FM) steels processed with improved thermal mechanical treatments (TMT) to give improvement in high temperature creep resistance over the conventional steels. Both steels were 4.3 mm in thickness and they were placed on top of a 4.9 mm thick F/M backing plate. A PCBN tool with 25.4 mm diameter shoulder and 6.5 mm long tapered pin was adopted for the FSW. The welding direction was not along the two materials interface but at about 9° angle in an attempt to understand the effect of tool offsite on the bonding between dissimilar materials, as shown in Figure 21. The FSW shoulder is represented by the solid circle and the pin by the doted circle. Such experiment design made it possible to investigate the material flow and mixing to guide joining dissimilar materials. Preliminary examinations indicated good weld quality without any defect. Further investigation of this joint will be reported later.

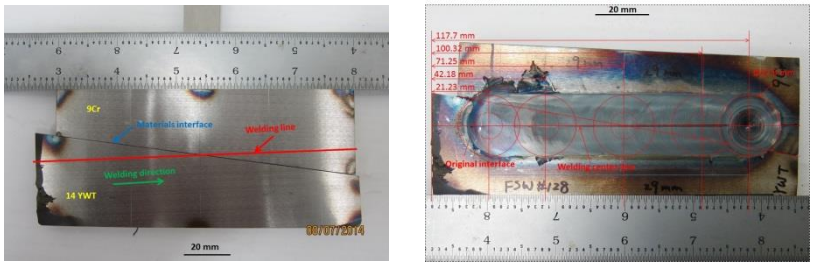

Figure 21. Dissimilar materials 14 YWT and F/M steel FSW plan and the welded joint

Earlier results on RAFM FSW showed that, similar to RAFM steel production heat treatment, 980°C × 0.5hr + quenching + 760°C × 0.5hr + air cooling, will restore joint microstructure and micro-hardness to base metal levels. An additional FSW parameter study was carried out aimed at joining RAFM steel with lower heat input to reduce the process temperature. By applying different tool rotation rates, different FSW heat inputs were achieved as shown in Figure 20. For conditions studied, the average stir zone hardness essentially was the same (404.4 VHN at 3266 W vs. 392.4 VHN at 2303 W). On the other hand, the stir zone width is considerably narrower and, as shown in Figure 22, the grain size for low heat input FSW is much smaller than that of high heat input. The hardness and microstructure results indicate that FSW temperature indeed dropped with low power input but remained in the fully austenitic temperature region. More investigations are planned to reveal relationship among FSW parameters, heat input, temperature, weld microstructure and mechanical properties.

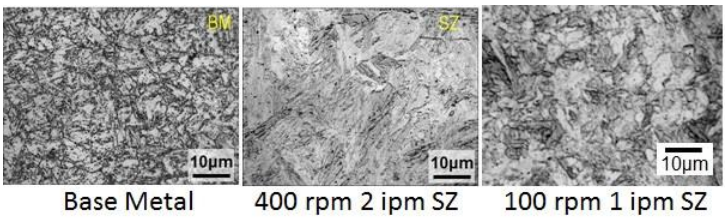

Figure 22. Microstructure of Eurofer'97 base metal and stir zone of FSW made with different heat inputs

Microstructure Characterization of FSW ODS Alloy

Earlier FSW was used to join 3 types of ODS alloys: MA956, 14WT and 14YWT. Since ODS is mainly strengthened by oxygen enriched nano-clusters, it is important to determine the influence of the thermal-mechanical FSW process on those nano-clusters. Previous studies by the project team and others in literature using TEM have been challenging and often inconclusive, due to the fine size of the nano-

clusters. As a result, we used the atom probe tomography (ATP) technique to characterize nano-cluster in the stirred zone and base metal. Figure 23 summarizes the ATP results. 2% O concentration iso-surfaces and 5% Ti concentration iso-surfaces were used to represent nano-clusters in MA956 and14WT/14YWT respectively. Figure 23 clearly shows near full-

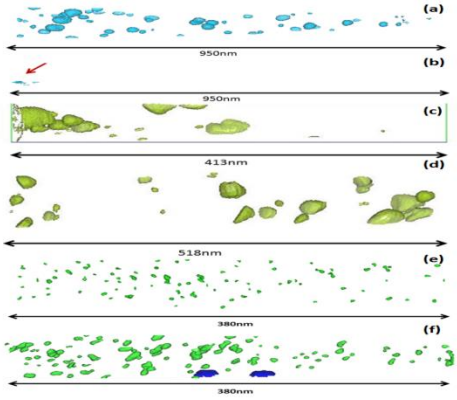

Figure 23. 2% O concentration isosurfaces for (a) MA956 base metal and (b) MA956 stir zone; 5% Ti concentration isosurfaces for (c) 14WT base metal, (d) 14WT stir zone, (e) 14YWT base metal and (f) 14YWT stir zone.

dissolution of nano-cluster in the stir zone of MA956. In contrast, nano-clusters in 14WT and 14YWT stir zones are more stable, but their sizes are larger than those in the base metal. Quantitative analysis showed the mean radius increased from 9.13 ± 8.3 nm in the base condition to 11.21± 8.2 nm in the stir zone for 14WT and from 1.9 ± 0.6 nm in the base condition to 2.7 ± 1.4 nm in the stir zone in 14YWT. In addition, electron backscattering diffraction study also showed 2-3 times increase of ferrite grain size in the stir zone for both 14WT and 14YWT. About 30% strength decrease in the stir zone is observed compared with base metal. Strengthening model shows coarsening of both the nano-clusters and the ferrite grains in stir zone contribute to the strength reduction. Therefore, FSW is a viable method for joining these unique materials without significant microstructure change or strength degradation. Future work will adjust FSW parameters to minimized nano-cluster and grain coarsening.

FSW 3D Thermal Mechanical Coupled Computer Modeling

The two fundamental parameters controlling the thermal-mechanical conditions experienced by FSW are temperature and material deformation, which affect joint microstructure and properties. However, it is extremely difficult to determine the thermal-mechanical fields accurately in FSW because they are coupled dynamic processes surrounded by solid metals. Computational models, when appropriately constructed, can simulate the complicated processes and provide insights on the temperature and deformation during FSW, to guide process development and optimization. To study the fundamental variables of FSW in joining ODS and RAFM steels, such as temperature, strain, strain rate and flow stress, 3D thermally and mechanically coupled numerical models were developed based on Computational Fluid Dynamics (CFD). In the model presented here, basic variables describing the heat flow and material flow in FSW are temperature and material velocity, which are obtained by solving governing equations in Eulerian formulation. The conservation equations of mass and momentum for incompressible single-phase flow are given by,

$$\nabla \cdot (\rho \vec{v}) = 0 \quad (1)$$

$$\nabla \cdot (\rho \vec{v} \vec{v}) = -\nabla p + \nabla \cdot \left(\mu(\nabla \vec{v} + \nabla \vec{v}^T)\right) \quad (2)$$

Where ρ is the density, μ is the viscosity, p is the pressure and $\vec{v}$ is the fluid velocity.

The energy conservation equation is given by,

$$\nabla \cdot (\vec{v}H) = \nabla \cdot (k\nabla T + S_V) \quad (3)$$

Where H is the enthalpy, T is the temperature, k is the thermal conductivity and S_V is a spatial source term regarding the heat generation due to plastic deformation.

Two tool pin configurations were chosen in this modeling, with step spiral and without step spiral, which are shown in Figure 24. Temperature fields from modeling results, Figure ***25*** , show that welding temperature for both conditions are lower than the material melting temperature but higher than the austenite temperature (about 850°C). Isothermal zones shown in Figure 24 reflect FSW joint metallurgical zones, and they match the metallurgical zones shown in FSW cross sections. Moreover, the step spiral pin tool caused more material deformation and resulted in higher welding temperature in FSW than the smooth pin tool.

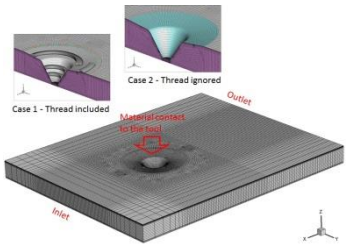

Figure 24. FSW process CFD computer model.

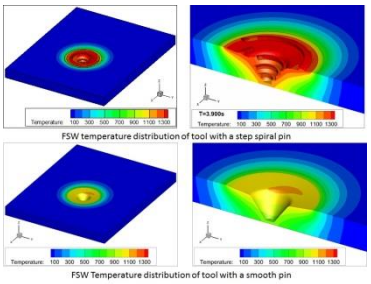

Figure 25.FSW temperature field modeling results

The initial modeling results show the model developed so far can reasonably simulate the temperature and material flow during FSW of ferritic steel, a major achievement in this project. More FSW conditions will be applied in the model, such as transient state modeling, different alloy FSW, different tool features and geometries, as well as various control parameters. Our ultimate goal is to fully understand all the physical and metallurgical phenomena happening in FSW of ODS alloys and advanced ferritic structural steels.

FUTURE WORK

The project is on schedule, without major technical issues. The following major activities are planned:

- Produce additional RAFM steels as well as ODS and ferritic steels dissimilar materials FSW joints with fine-tuned welding process conditions to further develop the basic understanding of process-microstructure-property relationship.
- Prepare for mechanical property testing of FSW joints, including long-term creep testing, under the as-welded and different PWHT conditions.
- Perform additional in-situ DIC and IR measurements during FSW to obtain the temperature and stress information under different process conditions.
- Implement further APT characterization of nano particles/clusters in the friction stir welded ODS alloys (MA956 and 14YWT) including the effect of post weld heat treatment.
- Further investigate the bonding mechanisms between ODS alloys and RAFM steels through detailed microstructure characterization.
- Continue computation modeling of the temperature and deformation history experience by the ODS and RAFM alloys.

4.6 MIXING OF ODS AND 9Cr F/M STEELS IN FSW JOINTS

D.T. Hoelzer (hoelzerd@ornl.gov), L. Tan, W. Tang and Z. Feng

OBJECTIVE

One of the challenges with deployment of advanced dispersion strengthened alloys and steels in components of fusion reactor cores, such as divertor and structural rings, is development of suitable joining technologies that will not degrade the high temperature properties and radiation tolerance of these materials. The objective of this project is to join advanced ODS ferritic alloys of 14YWT (14Cr), 9YWTV (9Cr) and FeCrAl (12Cr-5Al) to 9Cr ferritic/martensitic (F/M) steel by friction stir welding (FSW) and to characterize the solid-state mixing behavior of these dissimilar materials along a varying angle butt joint.

SUMMARY

Plates of 5 mm thickness were fabricated from the ODS 14YWT ferritic alloy and 9Cr F/M steel with one side cut with a tapered angle of 7.4º to form a varying angle butt joint. The two dissimilar materials were successfully joined along the varying angle butt joint by friction stir welding using a tapered pin tool made of polycrystalline boron nitride. Cross section samples for future microstructural characterization studies were extracted from three sections of the joined plates representing solid-state mixtures of: 1) ~80%/20%, 2)~50%/50% and 3)~20%/80% by volume fraction of the ODS 14YWT and 9Cr F/M steel, respectively.

PROGRESS AND STATUS

Figure 26 shows the experimental procedure for joining plates of the ODS 14YWT and 9Cr F/M steel along a varying angle butt joint. The plates were fabricated to 5 mm thickness followed by cutting one side of each plate at an angle of 7.4ºC relative to the reference travel direction of the pin tool. The FSW experiment is performed by having the pin tool travel along the center of the two adjacent plates resulting in varying volume fractions of the adjacent dissimilar alloys along the butt joint. Near the beginning, the pin tool will lie mostly in the 14YWT plate and overlap slightly with the 9Cr F/M steel plate to produce ~80%/20% mixture of the 14YWT and 9Cr F/M steel, respectively at the joint. At the mid-point, the pin tool will have roughly the same amount of each plate in the mixture, or 50% 14YWT and 50% 9Cr F/M steel in the butt joint. Finally, near the end of the FSW joint, the pin tool reverses the mixture of the butt joint so that it will include ~20% 14YWT and 80% 9Cr F/M steel.

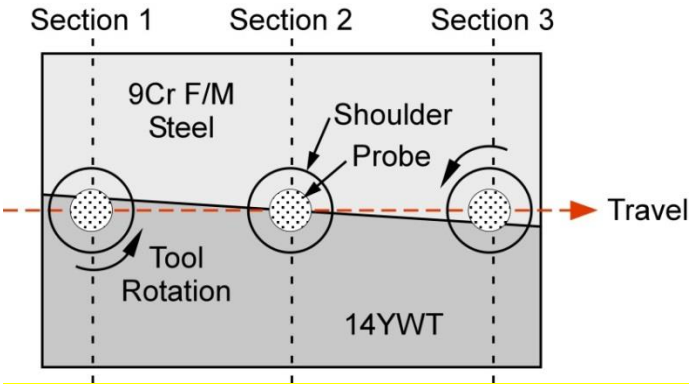

Figure 26. Illustration of the FSW experiment for joining 14YWT and 9Cr F/M steel along a varying angle butt joint.

Figure 27 shows the successfully joined plates of ODS 14YWT (bottom) and 9Cr F/M steel (top) along the varying angle butt joint by FSW. The ascending and descending directions including the rotation of the pin tool are shown. The first run was performed using a polycrystalline boron nitride (PCBN) pin tool that was 6.5 mm long and tapered from 10 mm dia. at the base of the 25 mm dia. shoulder to 3.5 mm dia. at the tip. The pin tool first entered the ODS 14YWT plate on the left side of the image and traveled to the right side where it exited (concentric rings) from the 9Cr F/M steel plate. Cross section samples for microstructural characterization were extracted from three sections of the joined plates shown in Figure 26 and are being prepared by metallographic procedures.

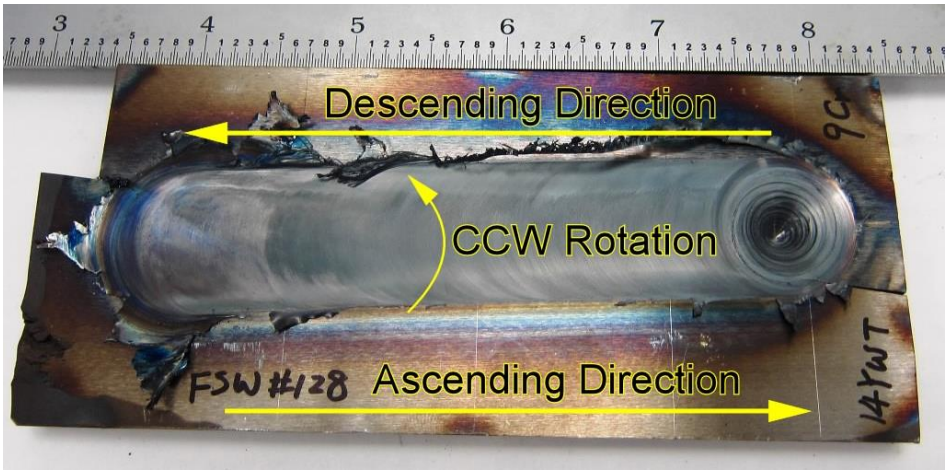

Figure 27. Digital image showing the successfully joined plates of 14YWT and 9Cr F/M steel by FSW along the varying angle joint. The ascending, descending and rotation directions of the pin tool are shown. The ruler shown at the top is in inches.

FUTURE PLANS

This project was initiated in April, 2014 and has resulted in the successful joining of ODS 14YWT and 9Cr F/M steel. Going forward, detailed microstructural studies will be conducted on the samples prepared from three sections along the varying angle butt joint to investigate the solid-state mixing that occurs between the two dissimilar materials and the effect that the different volume fractions of each material in the mixtures have on the overall integrity of the butt joint. Additional joints will also be produced by FSW joining of ODS 9YWTV and ODS FeCrAl alloys to 9Cr F/M steel using the same varying angle butt joint approach.

4.7 LIQUID METAL COMPATIBILITY IN FLOWING SYSTEMS

S. J. Pawel (pawelsj@ornl.gov), B. A. Pint

OBJECTIVE

The objective of this task is to identify potential structural materials having sufficient compatibility with flowing Pb-Li eutectic that the maximum metal temperature for operation can be increased to improve overall system efficiency.

SUMMARY

A thermal convection loop (TCL) fabricated using dispersion strengthened FeCrAl (Kanthal APMT) tubing – known for high strength and creep resistance at elevated temperature and, based on capsule testing, also anticipated to have excellent resistance to Pb-Li – was operated continuously for 1000 h at a peak temperature of 550 ± 1.5˚C and an average temperature gradient of about 116˚C. The resulting flow rate was approximately 0.4 m/min, as evaluated by periodic "hot-spot" testing which measured the amount of time required for a torch-imposed temperature spike to move sequentially among the thermocouple positions around the loop. The TCL contained chains of APMT specimens spanning the length of both the hot leg and cold leg to facilitate the compatibility assessment.

Following 1000 h of operation, the loop was terminated with the initial attempt to drain the Pb-Li into the dump tank positioned at the bottom of the cold leg. Unfortunately, problems were encountered with a cold spot within the very thick lid of the dump tank and, as a result, this attempt to drain the loop was unsuccessful. After allowing all of the remaining Pb-Li to freeze in place within the loop, it was confirmed that the Pb-Li froze in the dump tank lid after only partially draining from the loop. Other difficulties were encountered upon reheating of the loop to liquefy the Pb-Li and again attempt to drain it from the loop, including a small leak that developed – apparently in the thermowell weld at the top of the cold leg (analysis underway) – and a somewhat surprising incomplete draining of the hot leg (despite thermocouple data indicating drainage had occurred). The latter difficulties substantially delayed removal of specimens from the hot leg of the TCL, but analysis of the specimens and components of the loop is now underway.

To facilitate analysis, specimens (and pieces cut from the loop itself at key locations) were thoroughly cleaned in a 1:1:1 mixture of ethanol, hydrogen peroxide, and acetic acid – while within the loop as an assembled chain and again upon removal as individual specimens. The cleaning solution readily dissolves residual Pb-Li without attacking APMT, thus rendering weight change measurements more meaningful. Following exposure to the cleaning solution, the specimens were ultrasonically cleaned in acetone followed by air drying prior to photography and weighing.

PROGRESS AND STATUS

Figure 28 shows the mass change as a function of temperature for the specimens following cleaning. The approximate temperature of each specimen location was estimated by linear extrapolation as a function of position between thermowell locations at which the temperature was known. In Figure 28, all the specimens represented were given a pre-oxidation treatment (8 h in air at 1050˚C, slow cool) to stabilize the alumina-rich oxide film that forms on this alloy (the fabricated loop received the same treatment). Note that, except for the single specimen exposed at the lowest temperature in the loop (at the bottom of the cold leg), all specimens exhibited a net weight loss as a result of exposure, with greater weight losses occurring at higher exposure temperatures, although the pattern is somewhat irregular.

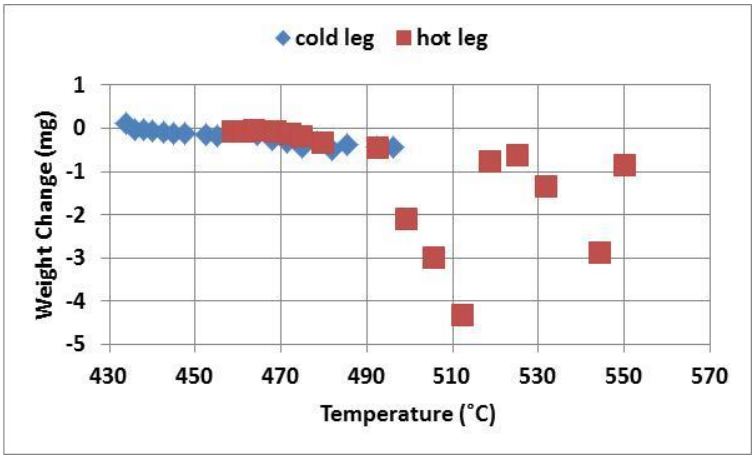

Figure 28. Weight change for pre-oxidized APMT specimens as a function of Pb-Li temperature following 1000 h exposure. Specimens from the hot leg and cold leg are differentiated by color and shape in the graph. Specimens originally weighed approximately 500 mg after heat treatment, with a surface area of 2.0 cm^2.

The data in Figure 28 excludes a few specimens that were included in the test. Two pre-oxidized specimens from the hot leg were discovered to be fractured upon opening the loop and removing the specimen chain. The time(s) associated with the fracture of these specimens is not known, but it is suspected to be during the reheating event at the end of loop operation (perhaps resulting from stresses related to the large volume change in the Pb-Li freeze-thaw cycle). In addition, two specimens in each of the hot leg and cold leg did not receive the pre-oxidation heat treatment, but were exposed with only the air-formed film at room temperature that develops after the specimen machining process. The latter specimens exhibited weight losses a factor of 5 to 25 times greater than the immediately adjacent pre-oxidized specimens in the loop.

These observations associated with Figure 28– that all specimens reveal at least a modest weight loss, and that specimens without an alumina-rich film exhibit much greater weight loss – suggest that the pre-oxidation film is partially protective but that eventually, at higher temperatures or longer times, the protective qualities are compromised in flowing Pb-Li. Surface analysis has been initiated, and preliminary results suggest that the alumina-rich oxide film is either being dislodged or dissolved in irregular patterns on specimen surfaces. Figure 29 shows a representative specimen surface following the 1000 h exposure. The specimen appears somewhat mottled, with most areas appearing relatively dark (remnant of the pre-oxidized surface) with isolated areas that appear relatively light (oxide-free APMT). Although the significance of the observation is not yet understood, also note that the pre-oxidation film appears to have been removed preferentially from the specimen edges (around number stamps, around the hole, at specimen corners, etc.), suggesting the initiation sites for the alumina-rich film degradation reaction. Element maps generated from the designated area of Figure 29 are shown in Figure 30 which confirm the dark areas represent a constituent rich in Al and O (alumina or a transition product resulting from exposure) and the light areas represent essentially bare metal (rich in the primary elements of APMT, with the exception of perhaps selectively dissolved Al). Mo deposits of any kind were observed on the specimens.

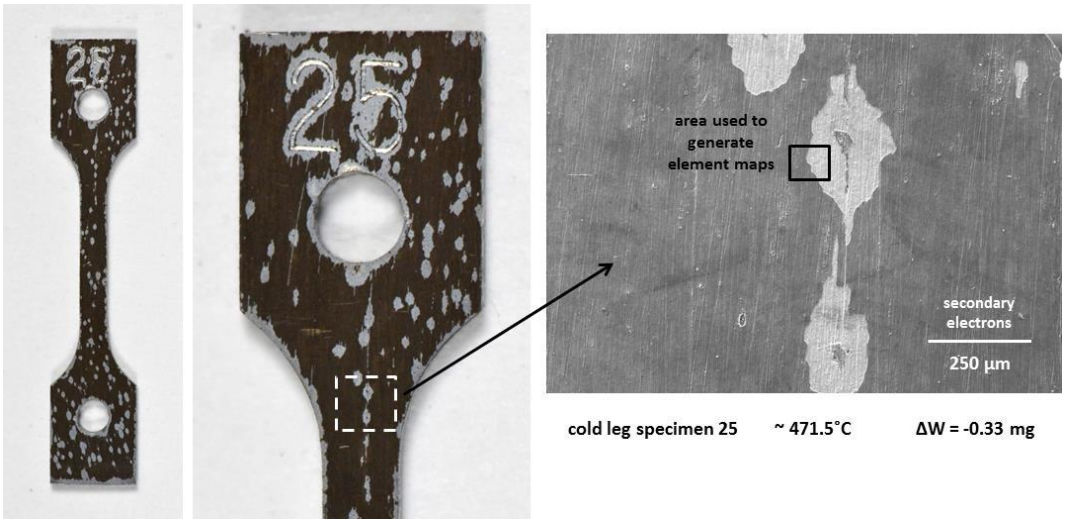

Figure 29. Representative loop specimen surface following exposure to flowing Pb-Li for 1000 h at approximately 471.5˚C. Element maps were generated from the area designated in the photograph at right.

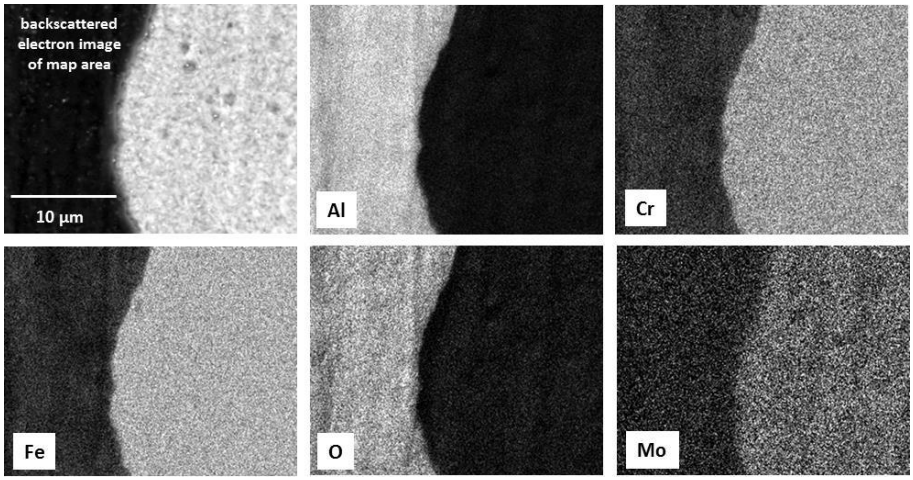

Figure 30. Element maps indicating the relative concentration of key constituents of APMT and the alumina film formed during the pre-oxidation step. Relatively lighter areas correspond to higher concentrations of the element being surveyed.

Figure 31 shows three flow loop specimens representing a wide range of temperature exposures. The appearance of these specimens suggests that as the Pb-Li exposure temperature is increased, less of the relatively dark regions (alumina-rich film) remain in favor of essentially bare metal.

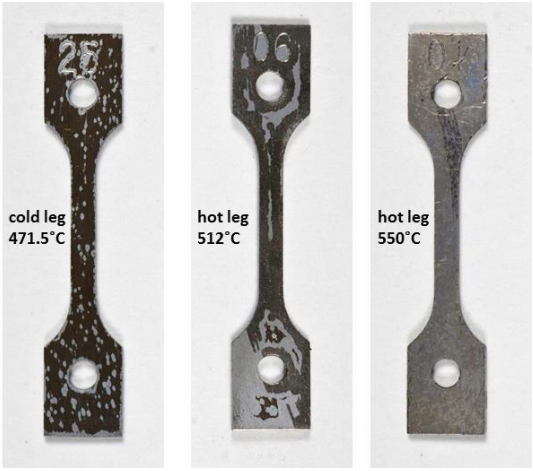

Figure 31. Appearance of loop specimens following exposure at the indicated temperatures. Note that as the temperature increases, less of the surface is covered by the relatively dark aluminum-rich film.

FUTURE PLANS

Following additional surface analyses such as x-ray diffraction to examine the residual oxide film (and any potential transformation that has occurred), the individual loop specimens will be tensile tested to assess changes in mechanical properties as a result of time-at-temperature exposure as well as chemical changes resulting from interaction with Pb-Li. Metallographic cross sections – of individual specimens as well as selected sections of the loop tubing – will be assessed for structural and chemical changes. Analysis will include an attempt to examine the leak location at the top of the cold leg to determine both the cause and possible improvements in loop fabrication. Subsequent loops will be fabricated and operated based on the results of the analyses described here.

5.0 COMPOSITE MATERIALS

5.1 FOA - DEVELOPMENT OF SiC JOINING TECHNOLOGIES FOR FUSION

Y. Katoh (katohy@ornl.gov), T. Koyanagi, J.O. Kiggans, C. Shih, L.L. Snead, T. Hinoki (Kyoto University), M. Ferraris (Politecnico di Torino), and C.H. Henager, Jr. (PNNL)

OBJECTIVE

Joining is a key technology for integration of silicon carbide (SiC) composite-based fusion blanket components. This project is developing radiation-tolerant joining technology for SiC materials. The main tasks are 1) process development to fabricate robust SiC joints, 2) development of test methods to determine the strength of ceramics joints, and 3) irradiation experiments to understand the radiation tolerance of SiC joints.

SUMMARY

1) Two types of SiC joints with robust strength were demonstrated. These joints were made by the pressureless MAX phase process and pressureless transient-eutectic (TEP) process. The TEP joint promises irradiation tolerance due to the SiC-based bonding layer with limited second phases.
2) Drafting of a new ASTM standard test method for torsional shear strength of adhesive joints of ceramics was complete.
3) The torsional test is deemed promising for evaluating irradiation experiments using miniature joint specimen, based on comparison of four different shear test methods.
4) Candidate SiC joins were irradiated under various neutron irradiation conditions in HFIR. Post-irradiation evaluation is planned in the next fiscal year.

PROGRESS AND STATUS

Process development for silicon carbide joints
Robust SiC joints have been fabricated with pressurized methods such as titanium and molybdenum diffusion bonding. Pressureless joining technologies for SiC materials were developed by reaction forming MAX phase process and TEP process, which are applicable to joining of large and complex shaped components. For the pressureless MAX phase bonding, dense microstructures with SiC and Ti_3SiC_2 phases were demonstrated with commercially available Ti-Si-C powder. The pressureless TEP joint was fabricated by sintering using SiC nano-sized powder and small amount of Y-Al-O additives without external stress following pre-densification by moderate cold-pressing. Both joints exhibited robust strength, determined by double notch shear test. Figure 32 shows the microstructures of high strength pressureless MAX phase and TEP joints.

Test method development
A torsional shear test using hourglass-shaped specimen was developed in our previous work. We are working to make this method the standard in ASTM Committee C28 on Advanced Ceramics. The first draft of a new ASTM standard test method for torsional shear strength of adhesive joints of ceramics was completed. Moreover, additional shear tests on miniature ceramics joints were studied for irradiated specimens formed using robust MAX phase joints by double notch shear (DNS), asymmetrical four point bend using metal extensors (A4PB), and Iosipescu tests with metal extensors. The results revealed that 1)DNS test showed higher stress concentration at the notch base and a lower nominal shear strength, 2) A4PB and Iosipescu tested joints exhibited tensile type of failure due to failure of the extensor, and 3) the

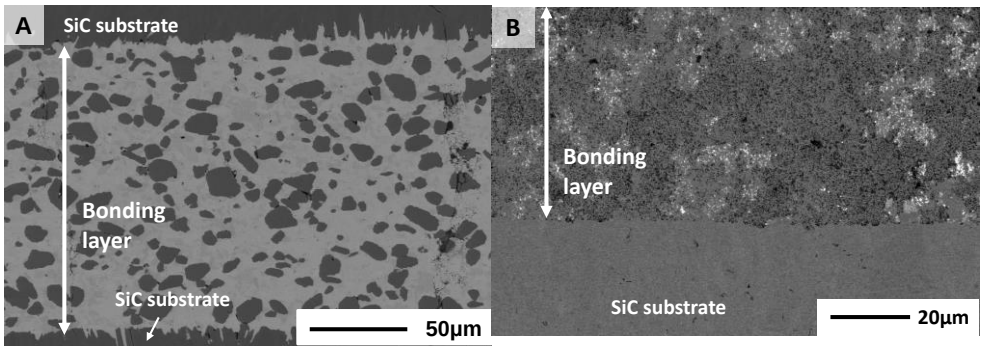

Figure 32. Backscattered electron images of pressureless MAX phase (A) and TEP (B) joints.

torsion test can deliver true shear loading. None of the tests can successfully induce true shear failure of the joint because the joint is stronger and tougher than the SiC substrate. Torsion tests appears to be promising for testing of high strength miniature joint specimens because of the pure shear loading, less stress concentration, and easy alignment. The setup for new torsion system introduced in this period is shown in Figure 33.

Figure 33. Torsional shear test apparatus.

Irradiation effects on various SiC joints

Our previous works revealed irradiation tolerance of various SiC joints formed by Ti and Mo diffusion bonding, pressurized TEP process (tape and slurry), calcia-alumina glass ceramics, and pressurized MAX phase processes, following irradiation at 500 and 800°C to low fluence. This study was extended to higher irradiation temperature (~1000°C) and higher does (>10 dpa) for these promising joints. In addition, newly developed SiC joints including pressureless TEP, pressureless MAX phase, Ti spark plasma sintered, and metal brazed joints were also irradiated at ~500°C to 3 dpa for screening evaluation. The irradiations are still ongoing in HFIR, and post irradiation testing is planned in FY2015. The experiments will include torsional shear tests using miniature hourglass-shaped specimens, microstructural observation by optical and scanning electron microscopes, phase identification by X-ray diffraction, and evaluation of SiC irradiation temperature monitors. Table 3 shows the test matrix for this irradiation experiment.

Table 3.Test matrix for neutron irradiation experiment of various SiC joints.

Joining Method	Expected Joint Phases	Target Irradiation Conditions		
		500C 3dpa	500C 10dpa	1000C 3dpa
Ti diffusion	Ti_3SiC_2, TiC	√		√
PressurelessMAX phase	Ti_3SiC_2, SiC	√		√
MAX phase	Ti_3SiC_2, SiC		√	
Ti SPS	Ti	√		
PressurelessNITE	SiC, Y-Al-O	√		√
NITE slurry	SiC, Y-Al-O		√	√
NITE tape	SiC, Y-Al-O		√	√
Mo diffusion	Mo_5Si_3C, Mo_2C	√		√
CA glass	$12CaO·7Al_2O_3$, $3CaO·Al_2O_3$		√	√
Brazing	Al-Si-C-O	√		√

FUTURE PLANS

Joining process development: Optimization of the pressureless TEP process will be pursued for the joining of SiC materials to achieve defect-free microstructures and potential irradiation tolerance by reducing the amount of secondary phases.

Test method development: Further development of the torsional shear test will be conducted. Specimen size effects on the test will be investigated utilizing brittle ceramics joints, which can contribute to the ASTM testing standard.

Irradiation effects: Post-irradiation evaluation of various SiC joints will be conducted to investigate the irradiation tolerance and to understand the damage mechanisms in the bonding layers.

5.2 IRRADIATION CREEP OF NUCLEAR GRADE SiC MATERIALS

Y. Katoh (katohy@ornl.gov), T. Koyanagi, T. Hinoki (Kyoto University) and L.L. Snead

OBJECTIVE

This research is to investigate the irradiation creep of nuclear grade SiC, which often defines the design limit stress for thermo-structural fusion components. The main focus this fiscal year was on the irradiation creep of high-purity SiC in the steady-state stage up to ~30 dpa and the creep behavior of nuclear grade generation III SiC fibers.

SUMMARY

1) The measurement of irradiation creep strains up to ~30 dpa was complete for high-purity SiC materials, revealing that the irradiation creep compliances of SiC are very small in the steady-state region at 300 to 800°C.
2) An irradiation creep experiment for nuclear grade SiC fibers was developed, and the creep strain was successfully evaluated. The important finding included that Hi-Nicalon Type-S fiber was less creep resistant than other nuclear grade fibers at 500°C for low neutron fluences.

Steady-state creep of SiC ceramics under irradiation

Systematical investigations of irradiation creep of SiC materials have been achieved by development of bend stress relaxation (BSR) method for rabbit capsule irradiation in ORNL. The early work revealed irradiation creep behavior and the underlying mechanism relating anisotropic swelling in SiC in the transient region (up to ~1 dpa). Recently, the interest is in the steady-state creep behavior after the transient region. Initial evaluation of the irradiation creep for high-purity chemical vapor deposited (CVD) SiC at 300, 500, and 800°C to up to ~30 dpa found that 1) irradiation creep still operated until high dose at 300 and 500°C, 2) the stress exponent of the creep remained unity, and 3) material quality of CVD SiC affected the creep behavior at high does. Data analysis revealed the existence of steady-state irradiation creep in CVD SiC and the creep compliance was very small. The linear average creep compliances were of order 10^{-8} to 10^{-7} dpa^{-1} MPa^{-1} for irradiation to 10–30 dpa, a appeared to vary depending on grain size, pre-existing defects, and anisotropy of material structure. Figure 34 shows BSR creep behavior of CoorsTek CVD SiC irradiated under various conditions.

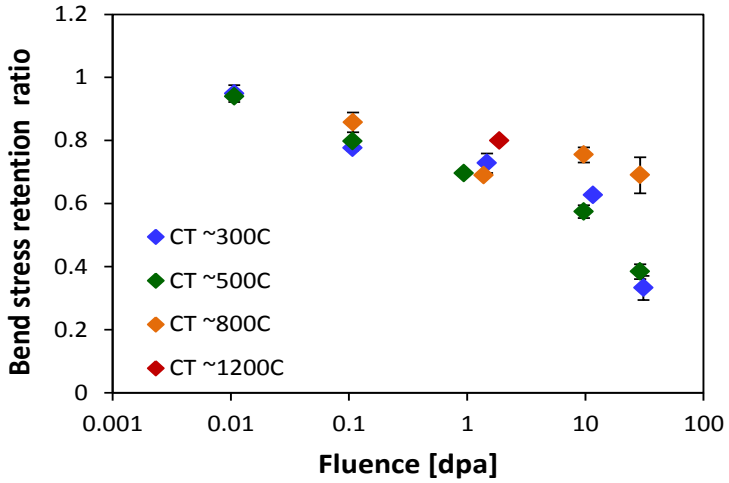

Figure 34. Bend stress retention ratio of high-purity CoorsTek CVD SiC during various irradiation conditions. The initial bend stress applied was up to ~300 MPa.

Irradiation creep of generation III SiC fibers

The irradiation creep of SiC fibers is poorly understood, though it is important to understand the creep behavior of SiC composites. The BSR method used for CVD SiC in this program was modified, and then used for nuclear grade generation III SiC fibers including Hi-Nicalon Type-S, Tyranno SA3, developmental Sylramic, and developmental Sylramic iBN fibers. Note that the Sylramic and Sylramic iBN fibers were isotopically-controlled, with enhanced ^{11}B instead of ^{10}B to reduce transmutation helium production from nuclear reactions during irradiation. The test fixture developed is shown in Figure 35. The fixture was made of nuclear grade graphite to avoid chemical reaction between the fibers and the fixture. The initial bending stress systematically ranged from ~200 to ~1400 MPa. The irradiations at ~500 and ~1200°C to up to 10 dpa were complete this fiscal year.

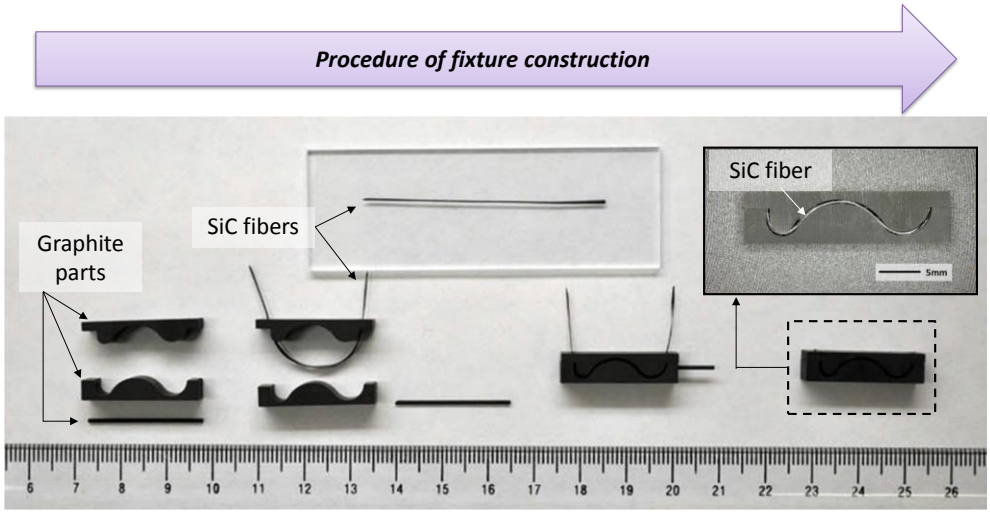

Figure 35. BSR fixture for irradiation creep experiment on SiC fibers.

Irradiation creep was clearly observed for all types of fibers at ~500°C to ~1dpa; the curved appearance of irradiated fibers in Figure 36 is the evidence of irradiation creep. If there is no irradiation creep, the fibers would remain straight. The creep strain was obtained from measurement of the curvature of the fiber, which revealed that Hi-Nicalon Type-S fiber has less creep resistant than other fibers for that irradiation condition.

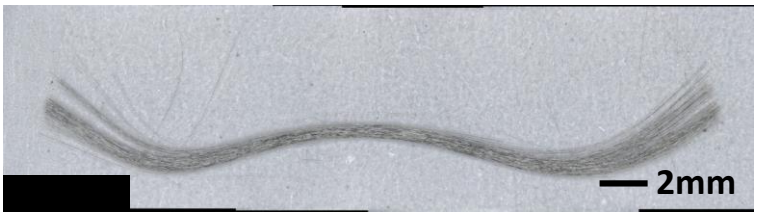

Figure 36. Optical micrograph of crept Sylramic fibers following BSR experiment at 500°C to ~1 dpa.

FUTURE PLANS

Further examination of irradiation creep of the nuclear grade SiC fibers will be conducted by measurement and microstructural observation to understand the effects of material quality, irradiation temperature, and neutron fluence on the creep behavior. The implication for performance of SiC fiber-reinforced composites under irradiation will be evaluated based on the irradiation-creep resistance of SiC fibers. Consequently, the understanding of the fiber creep will provide basic knowledge for the selection of fiber to fabricate irradiation-tolerant fiber-reinforced composites.

5.3 MICROSTRUCTURES AND MECHANICAL PROPERTIES OF IRRADIATED SiC

Y. Katoh (katohy@ornl.gov), A.G. Perez-Bergquist1, T. Koyanagi, C.M. Parish, T. Nozawa (JAEA), K. Ozawa (JAEA), S. Kondo (Kyoto University,) and L.L. Snead

OBJECTIVE

The objective of this task is to obtain a further understanding of effects of high fluence and/or high temperature neutron irradiation on mechanical properties and microstructures of silicon carbide (SiC) and SiC fiber reinforced SiC matrix (SiC/SiC) composites for fusion structural applications.

SUMMARY

1) Detailed microstructural analysis of Hi-Nicalon Type S fiber in SiC/SiC composites irradiated to >70 dpa were conducted, and the results are in an accepted journal article.
2) Mechanistic understanding of irradiation creep of high purity SiC was obtained by microstructural observation; a stress induced preferential nucleation/absorption mechanism contributed to irradiation creep of high purity SiC.
3) Ultrahigh-resolution microscopy of individual Frank loops in ion-irradiated SiC was used to test the feasibility of measuring the atomistic structure of single defects via aberration-corrected electron microscopy.

PROGRESS AND STATUS

Effects of high dose irradiation on SiC/SiC composite

Previous ORNL-JAEA collaborations on fusion materials have accomplished neutron irradiations to greater than 70 dpa at 300, 500, and 800°C in HFIR, and provided extensive understanding of irradiation effects on thermomechanical properties of early nuclear grades of Hi-Nicalon Type S fiber SiC/SiC composites. Recent evaluation of this material strongly indicated the degradation of Hi-Nicalon Type S fiber for low irradiation temperatures. Detailed analysis of microstructures of this fiber, especially for the secondary phase of free carbon, was conducted using transmission electron microscopy (TEM). The summarized data is included in an accepted article in Journal of Nuclear Materials in 2014. This work revealed instability of the secondary phases in the Type S fiber, which is suspected to relate to the strength degradation. Figure 37 shows micrograph of the secondary phase in the Type S fiber irradiated at 300°C to ~70dpa.

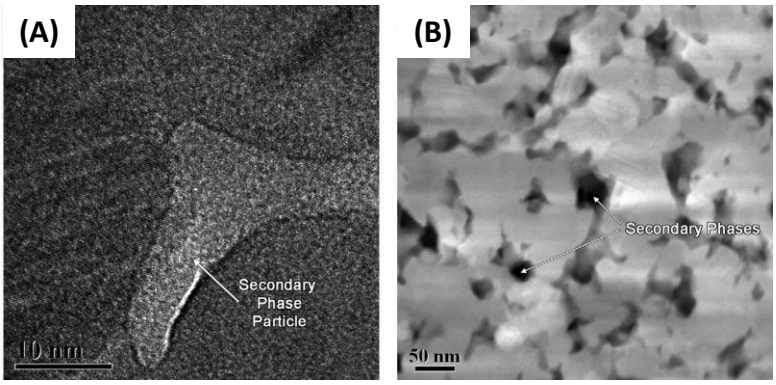

Figure 37. TEM images of the secondary phase in Hi-Nicalon Type-S fiber irradiated at 300°C to ~70 dpa: (A) high resolution TEM image, (B) high-angle annular dark field image.

Effects of stress on microstructural evolution during irradiation of SiC

In-pile stress tests for SiC and SiC/SiC composites have been developed utilizing bend stress relaxation experiment in ORNL. This series of experiment has provided systematical data of irradiation creep of various SiC materials, and revealed that irradiation creep rates in SiC are very small compared to metals. In this period, extensive investigation of the stress effect (creep behavior) was pursued by microscopic observation of irradiation-induced defects of interstitial loops in high purity chemical vapor deposited SiC irradiated at 300 and 800°C to ~10 dpa. A small portion (< ~10%) of irradiation creep strain can be explained by deformation due to observed anisotropic defect formation (Figure 38), which is known to be the stress induced preferential nucleation/absorption mechanism. This result strongly indicates that the dominant mechanism of irradiation creep in SiC was attributed to defects invisible and/or unidentified in conventional TEM images. The requirement of further microscopic level analysis motivated observation using a state-of-the-art TEM instrument, which is described in the next section.

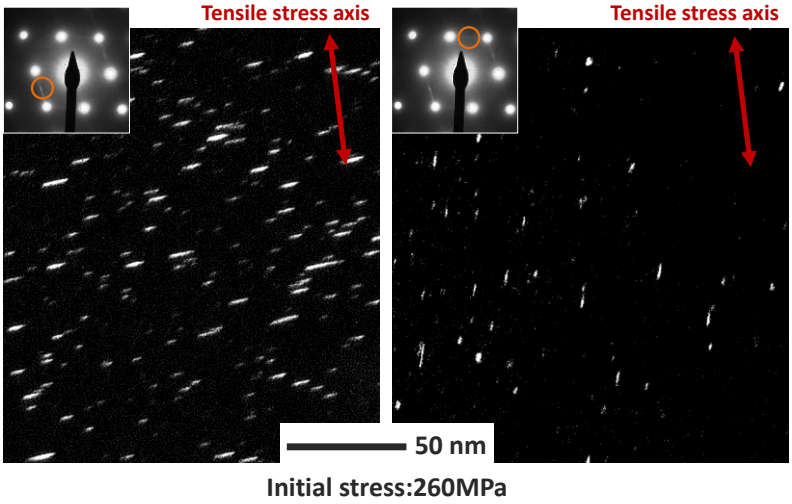

Figure 38. Dark field TEM images of high-purity chemical vapor deposited SiC irradiated with applied stress at 800°C. Both images were taken from the same area, but taken using different diffraction spots.

Atomistic defect structures in irradiated SiC

Microstructural observation using TEM has provided mechanistic and quantitative understanding of irradiation effects in SiC materials. However, defects visible in the conventional instrument can explain only a small part of the irradiation phenomena such as creep and swelling in SiC. For better understanding of mechanisms in irradiated SiC, a new attempt at atomistic scale observation was conducted using ultrahigh-resolution imaging in the aberration-corrected scanning transmission electron microscope, STEM, coupled with image simulation theory.

β-SiC samples were irradiated to ~4.8×10^{21} ions/m^2 with 5.1 MeV Si^{++} at 1200°C at the DuET facility at Kyoto University, and TEM samples were prepared using gallium focused ion beam (FIB) methods followed by cleaning with low-energy argon ions. Peak dpa was ~150 and mean dpa ~30-60. Samples were examined in the ORNL Titan STEM instrument. When on <101>-oriented grains, dense dislocation loops were observed at atomic resolution, Figure 39, strain is visible around the Frank loop in Figure 39b, indicating the misfit from the defect.

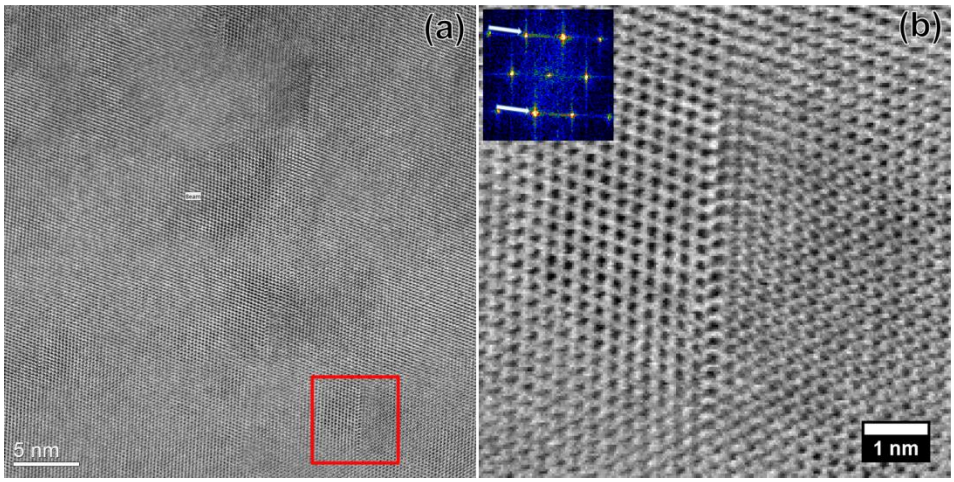

Figure 39. (a) bright-field aberration-corrected STEM image of dislocation loops in irradiated β-SiC. (b), enlarged view of the region boxed in (a). Inset to (b) is a 101-type diffractogram (Fourier transform) showing streaking associated with the faults.

Higher-resolution imaging can be compared to calculated images. Bright features in high-angle annular dark field (HAADF) images are Si atomic columns, and a two-layer-wide defect is visible at high resolution (Figure 40). This indicates an extrinsic fault (interstitial-type) Frank loop, an atomic model of which is projected onto the columns in Figure 40. Comparisons to simulated STEM images (using the multislice method and frozen-phonon approximation) are favorable (Figure 40, inset), but some features are not captured, which implies strain or point defects not accounted for in the model are contributing to experimental contrast.

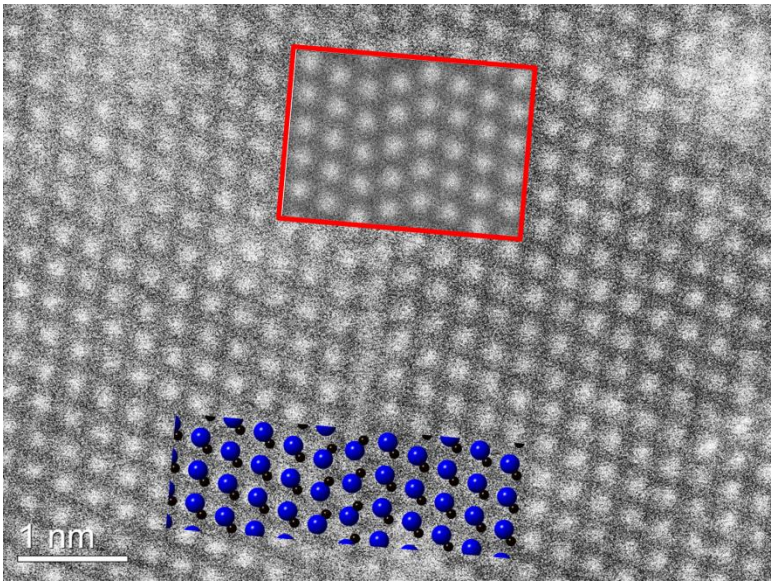

Figure 40. High-angle annular dark field STEM image in <101>-axis of a single Frank loop in irradiated β-SiC. The atomic structure of the extrinsic fault is overlaid (blue atoms: Si, black atoms: C) and a simulated STEM image is inset in the red border.

FUTURE PLANS

Additional thermomechanical tests of SiC/SiC composites with Hi-Nicalon Type-S fiber irradiated to > 100 dpa are planned. Because degradation of strength of this early nuclear grade SiC/SiC composite was demonstrated, current nuclear grade SiC/SiC composite with Tyranno-SA3 fiber will be irradiated to high doses. Regarding microstructural observation in SiC, evaluation of defects will be extended to high dose irradiated specimens to understand the creep behavior in the steady-state region. In addition, certification of the ORNL Advanced Microscopy Laboratory building, and in particular the Titan STEM, for radiological specimens has been requested. If this request is granted, the ultrahigh-resolution techniques developed here will enable us to perform atomic-level characterization of defects in neutron-irradiated SiC and SiC-based composites, which will provide new insight into the defects underlying all irradiation-induced behavior.

6.0 HIGH HEAT FLUX AND PLASMA FACING MATERIALS

6.1 FABRICATION OF FUNCTIONALLY GRADED TUNGSTEN STEEL LAMINATE

L. M. Garrison (garrisonlm@ornl.gov), E. Ohriner

OBJECTIVE

The goal of this project is to leverage the high heat flux capabilities of tungsten and the durability of steel to create a tungsten-steel functionally graded laminate material that can be used in plasma-facing components of a fusion reactor.

SUMMARY

Tungsten foils in thicknesses 0.010, 0.004, and 0.001 in. were acquired commercially. Steel sheets of thicknesses 0.010, 0.004, and 0.003 in. were cold-rolled from a block of grade 92 steel. Analysis of the mechanical properties and microstructure of the foils is in progress. Alternating foils of steel and tungsten were stacked such that the resulting material will be graded from a primarily steel side to a primarily tungsten side. The laminate is currently undergoing hot rolling to bond the layers and create the tungsten-steel laminate composite.

PROGRESS AND STATUS

While tungsten is desirable as a plasma-facing material, it is brittle and has a significantly different coefficient of thermal expansion than steel, which would be a likely choice for the structural material under the tungsten armor. Creating a functionally graded tungsten-steel laminate material attempts to overcome the challenges of the tungsten brittleness and the difficulty of joining it to the underlying structural material. Tungsten foil is known to be more ductile than standard powder metallurgy tungsten, and grading the composition of a material is a way to reduce the thermal expansion stresses.

Tungsten foils in thicknesses 0.010, 0.004, and 0.001 in. have been acquired commercially. Steel sheets of thicknesses 0.010, 0.004, and 0.003 in. were cold-rolled from a block of grade 92 steel. The steel foil was not able to be reduced below 0.003 in. due to cracking. After rolling, the steel foils were sectioned into 1 by 1 in. squares with electric discharge machining (EDM) to match the outer dimensions of the commercial tungsten foils. The surface of each of the steel and tungsten foils was observed in a digital optical microscope in the as-fabricated state. The rolling direction is clearly seen in the steel foils (Figure 41aand Figure 41b) but they also show some texture perpendicular to the rolling direction, more so than the tungsten foils of the same thickness (Figure 41c and d). The texture on the tungsten foils becomes finer as the thickness of the foils decrease. On the thinnest tungsten foil, 0.001 in. thick, the primary rolling direction is more difficult to distinguish because of the presence of other ridges running perpendicular to it (Figure 41e). It is possible the thinnest tungsten foil was rolled in multiple directions by the manufacturer to achieve the final thickness. Samples are currently being polished so that the grain size and structure can be examined with SEM and EBSD techniques.

All the foils, both steel and tungsten, were ductile and could be bent by hand. The thinnest tungsten foil, 0.001 in. thick (Figure 42a), was the most flexible and was able to be bent nearly in half without fracture (Figure 42b). When the foil was released it recovered elastically to near the original shape (Figure 42c). A tungsten foil 0.004 in. thick was bent to failure with the crease parallel to the rolling direction. The failure was primarily a delamination with large flat grains peeling apart (Figure 42d).

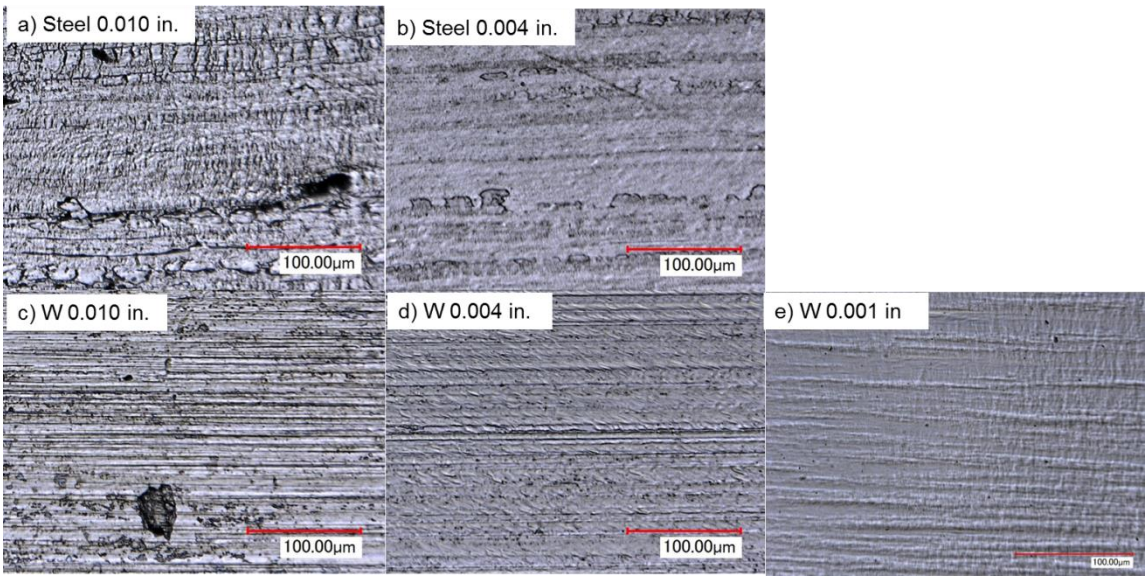

Figure 41. Surfaces of steel foils in thicknesses a) 0.010 in. and b) 0.004 in. with tungsten foils in thicknesses a) 0.010 in., b) 0.004 in., and c) 0.001 in. are observed as-fabricated in a digital optical microscope using the HDR imaging mode to enhance the texture.

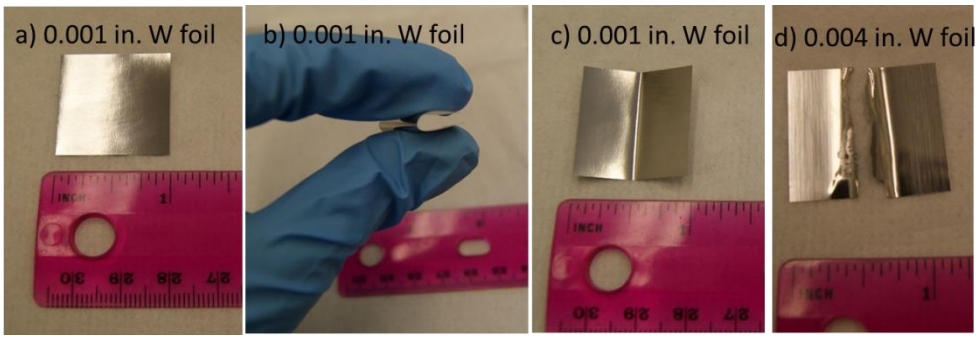

Figure 42. a) Tungsten foil 0.001 in. thick as-received. b) The foil can be bent almost in half without cracking. c) When released, the foil springs back to nearly flat. d) The 0.004 in. foil is less flexible than the 0.001 in. foil and was bent to failure.

The nanohardness of all the foils was measured with a Wilson nanohardness indenter using different loads from 0.050 to 1 kg each at a dwell time of 10 seconds. There was some dependence of the hardness value on load when the load was below 0.2 kg, so that load value is used for comparison between the materials. The 0.001 in. tungsten foil had a larger spread in the data than the other samples and showed a decrease in hardness with increasing load. The results of the 0.001 in. foil may not be accurate due to its extreme thinness, and methods to measure its hardness more accurately are being investigated. It would be expected that the hardness of the tungsten foils would increase with decreasing thickness due to work hardening from the rolling. However, the details of fabrication are not available from the manufacturer, so it is unknown if a manufacturing process for the thinnest foil accounts for its lowered hardness. The steel foil 0.003 in. thick has not been tested yet, but the trend for the other two steel samples is increased hardness with decreased thickness, corresponding to increased work hardening. The tungsten foils hardness values are approximately 350 higher than the steel hardness values (Figure 43).

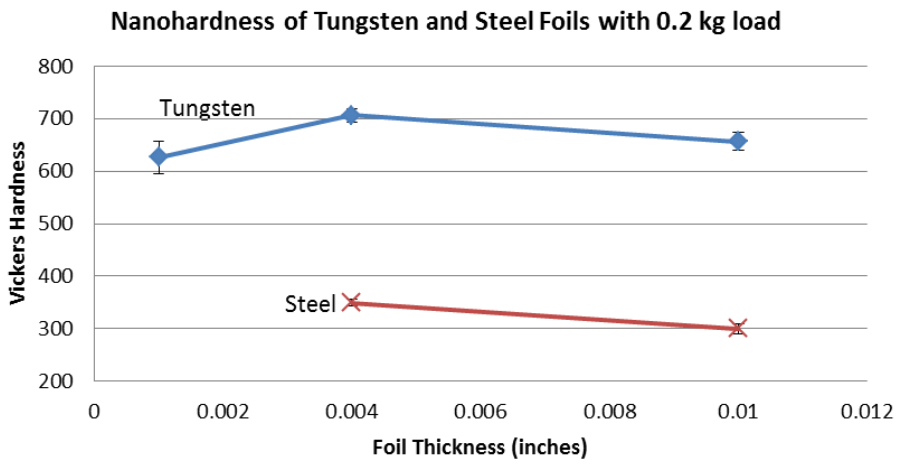

Figure 43. Hardness values for the tungsten and steel foils are compared for the case of 0.2 kg indentation load.

A stainless steel box was machined to hold the foils during the hot rolling joining process such that 0.75 in. of stainless steel surround the foils on all sides. Figure 44 illustrates the assembly process of the foils in the rolling box. The foils were all cleaned with ethanol at room temperature in an ultrasonic bath prior to assembling. The rolling direction of all the foils was aligned within the rolling box. The laminate material will be rolled further in this direction in an effort to maximize ductility of the laminate.

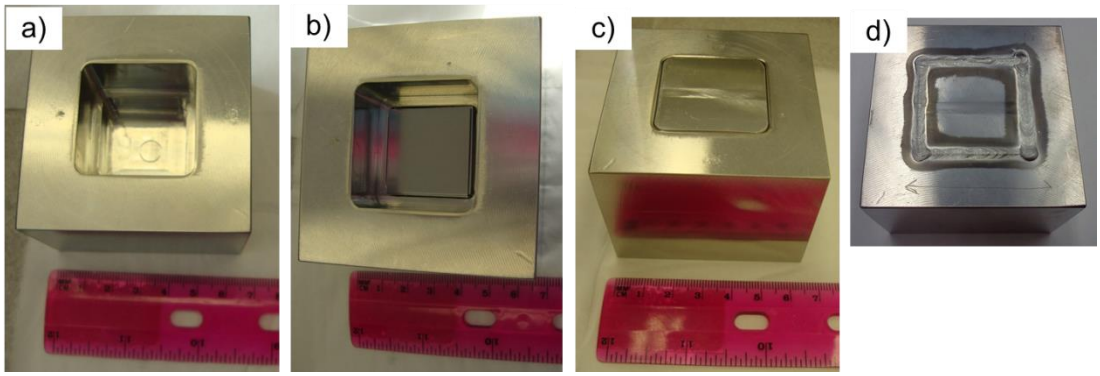

Figure 44. a) The stainless steel box for holding the foils during rolling is shown before assembly. b) The tungsten and grade 92 steel foils have been layered within the stainless steel box. c) The lid of the stainless steel rolling box fits flush with the top. d) The lid has been e-beam welded closed, and the arrow on the top surface indicates the rolling direction.

The foils were layered in three groups as illustrated in Figure 45. At the bottom, ten foils of 0.010 in. steel alternate with ten foils of 0.001 in. tungsten. In the middle, ten foils each of 0.004 in. steel and tungsten are stacked. At the top, ten foil layers of 0.010 in. tungsten alternate with 0.003 in. steel foils.

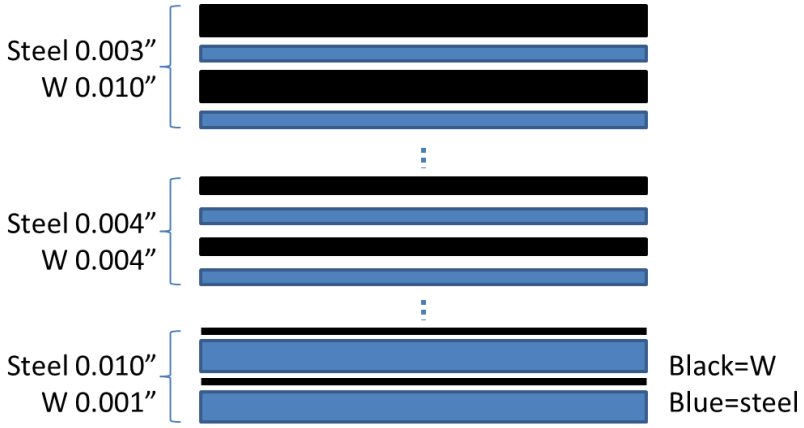

Figure 45. This illustrates the stacking pattern used to assemble the tungsten and steel foils within the rolling box. Each of the three sections consists of ten foils of each material.

The laminate is assembled and in the process of being joined by a combination of hot forging and hot rolling. The plan for joining starts with a 1 hour preheat to 1000°C followed by forging with 10% thickness reduction with half hour reheats to 1000°C until the thickness is 50% of the original thickness. The next steps will be hot rolling at 1000°C along the rolling direction with 10% reduction of thickness per pass. The goal is to achieve 80% reduction in thickness from the original value by the forging and rolling. The 1000°C temperature was selected because it is above the two phase temperature of the steel and below the recrystallization temperature of the tungsten.

FUTURE PLANS

Once the forging and rolling of the laminate has been completed, the mechanical properties and microstructure of the composite material will be investigated. Based on the results, the stacking pattern or joining process may be altered in future laminate fabrication to improve the tungsten-steel interface properties. The testing of the individual foils will include SEM, EBSD, and tensile tests.

6.2 ALLOYING AND NEUTRON IRRADIATION EFFECTS IN TUNGSTEN-RHENIUM

L. M. Garrison (garrisonlm@ornl.gov), L. L. Snead, E. Ohriner

OBJECTIVE

The purpose of this project is to de-couple the effects of neutron irradiation and rhenium additions on irradiated tungsten behavior. Tungsten transmutes to rhenium under neutron irradiation, therefore any neutron irradiated tungsten will contain some rhenium. To understand the effects of rhenium on tungsten, the mechanical properties of several tungsten-rhenium alloys will be measured before and after neutron irradiation.

SUMMARY

Six tungsten rhenium alloys with rhenium contents from 0 to 17.7 wt.% were fabricated by arc melting. The as-fabricated materials had large, 0.5-2 mm, grains as well as voids and cracks. The material in this state could not be machined into thin, 0.5 mm, disks needed for further experiments. Rectangular sections were machined from each alloy so that it could be hot-rolled to consolidate the microstructure. Rolling has been completed on two of the six alloys, with promising initial results, and will proceed with the other four alloys.

PROGRESS AND STATUS

Six samples of tungsten rhenium were fabricated by arc melting (Table 4). One control sample of unalloyed tungsten was fabricated as Alloy 6. The other five samples range in rhenium content from 0.033 to 17.7 wt.%. The as-fabricated buttons were round with diameters roughly 2 inches (Figure 46a). On the bottom side of the as-fabricated buttons, there are some voids or gaps visible (Figure 46b). Alloy 4 is shown, but is representative of the condition of all the as-fabricated alloys.

Table 4. W-Re alloy compositions.

Alloy number	Initial Re wt.%
Alloy 1	0.033
Alloy 2	0.165
Alloy 3	0.830
Alloy 4	3.440
Alloy 5	17.700
Alloy 6	0.000

Electric discharge machining was used to cut a sample from Alloy 4. The sample has very large grains on the order of ~0.5-2 mm (Figure 47a). As a comparison, a typically powder metallurgy tungsten sample will have grains on the order of 1-10 µm in size. Although a small piece of Alloy 4 was able to be polished and examined in the SEM, in general, all six of the as-fabricated materials were too difficult to machine into appropriately sized samples because they would crumble when thinly cut. It is believed that the large grain size, voids within the samples, and separation along grain boundaries, as seen in Figure 47b, contributed to the difficulty in machining samples.

To attempt to improve the material machinability, hot rolling was done on Alloys 1 and 4. A rectangular solid was cut by electric discharge machining (EDM) from the fabricated buttons. Molybdenum boxes were fabricated to surround the tungsten-rhenium pieces during rolling. The tungsten-rhenium alloy pieces were e-beam welded inside the molybdenum cans to prevent oxidation during the hot rolling. The molybdenum cans were then

Figure 46. The as fabricated tungsten rhenium alloy 4, with 3.44 wt.% rhenium.

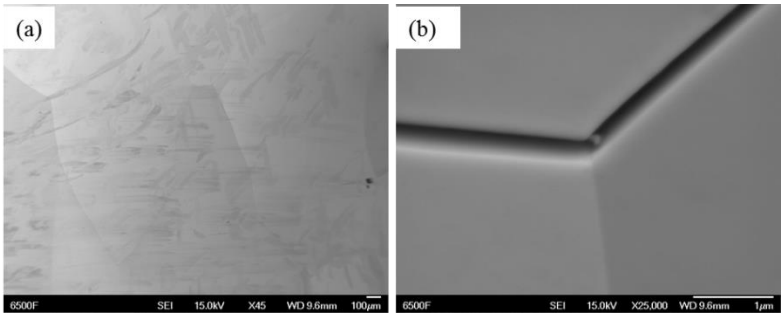

Figure 47. Microstructure of tungsten Alloy 4 with ~3 wt. % rhenium in the as-cast state had (a) large grains on the order of ~0.5-2mm and (b) separation along some grain boundaries.

covered with a molybdenum sheet of 0.62 inch thickness during the rolling process. The specimens were rolled with 1200°C preheat for 15 minutes and 15% reduction per pass with 15 minute reheats between rolling steps. Each specimen was reduced approximately 80% from its original thickness. After rolling, the molybdenum can was chemically dissolved to free the tungsten-rhenium sheet. The sections of both Alloy 1 and 4 had a rough, wave-like surface after rolling; Alloy 1 is shown in Figure 48a in the as-rolled state. Visual inspection showed the grains to be multiple millimeters wide, but thin, and with no visible voids in the specimens. Disks were successfully cut and polished from Alloy 4. In Figure 48b several disks from Alloy 4 are seen in different stages of finish ranging from as-cut with the rough surface finish to fully finished and polished. The hot rolling had a positive impact on the machinability of the alloys, so rolling will be completed for the other four tungsten-rhenium alloys.

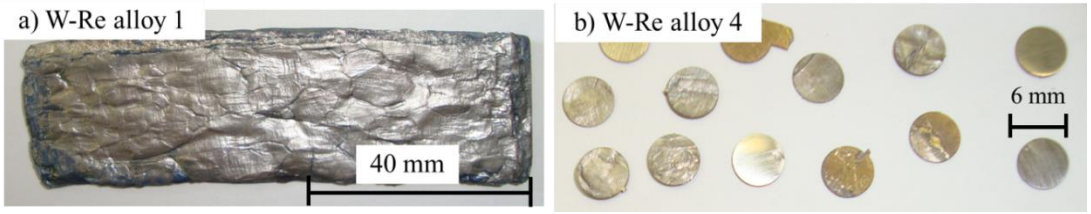

Figure 48. a) Tungsten-rhenium Alloy 1 after hot rolling. b) Alloy 4 sample disks cut from the rolled material in various stages of finish.

FUTURE PLANS

The remaining tungsten-rhenium alloys, numbers 2, 3, 5, and 6, will be hot rolled so that disk samples can be machined. Once the disks are produced, the thermomechanical properties and microstructure will be examined before irradiation in HFIR.

6.3 NEUTRON IRRADIATION EFFECTS IN TUNGSTEN

L.M. Garrison (garrisonlm@ornl.gov), L. L. Snead, N.A.P. Kiran Kumar, X. Hu, M. Fukuda (Tohoku University, Japan), T. Koyanagi, K. Yabuuchi (Tohoku University, Japan), T. S. Byun, M. R. McAlister, and W. D. Lewis

OBJECTIVE

The objective of this work is to evaluate the effect of neutron irradiation on the mechanical properties of tungsten with selected microstructures to aid in developing plasma-facing materials for fusion reactors.

SUMMARY

A total of 440 samples were irradiated in HFIR at temperatures from 70 to 900°C and fast neutron fluences of 0.01 to 20 $\times 10^{25}$ n/m^2, E>0.1 MeV. Types of tungsten irradiated in this study were [110] single crystal tungsten, [100] single crystal tungsten, wrought tungsten foils, annealed tungsten foils, and tungsten-copper laminate. Samples of single crystal tungsten that were irradiated to 2×10^{25} n/m^2 and below have been tensile and hardness tested at room temperature as well as at temperatures up to 650°C. The defect structure of selected low dose samples has been investigated by transmission electron microscopy. A subset of single crystal [110] samples was selected to study the effects of annealing on recovery of mechanical properties and defects through positron annihilation spectroscopy (PAS) and hardness testing.

PROGRESS AND STATUS

Samples of each different tungsten material--single crystal tungsten [110], single crystal tungsten [100], wrought tungsten foil, annealed tungsten foil, and tungsten-copper laminate--that received doses up to 2×10^{25} n/m^2 have been tensile and hardness tested. Tensile tests at temperatures up to 650°C for the low dose single crystal tungsten samples have been completed. Higher temperature tensile tests will be performed on tungsten-copper laminate samples as well. Selected samples from each different microstructure condition have been analyzed in the TEM. The higher dose samples have finished irradiation but have not yet been analyzed. Figure 49 illustrates the range of irradiation parameters.

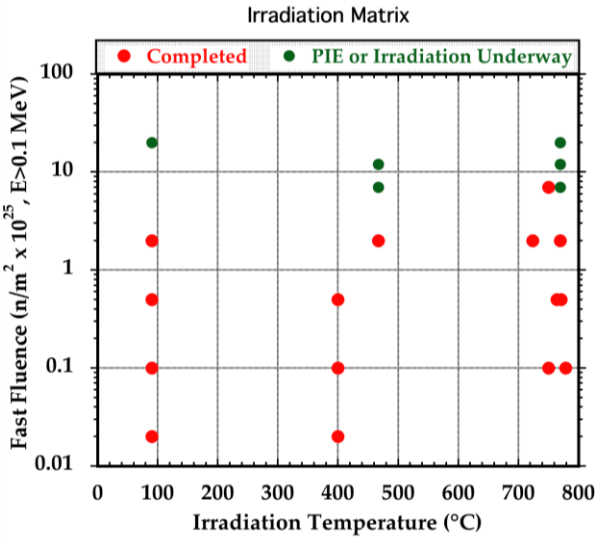

Figure 49. Irradiation matrix for the tungsten samples irradiated in HFIR in 2013.

Microstructural Analysis

In the unirradiated state, the wrought tungsten foil is composed of elongated, thin grains due to the rolling process used in production (Figure 50a). The annealed tungsten foil was subjected to a 1 hour anneal at 2700°C, well above the recrystallization temperature of tungsten; this created large grains within the foil before irradiation (Figure 50b). The tungsten-copper laminate consisted of alternating layers of copper and wrought tungsten foil (Figure 50c). The wrought tungsten foil, annealed tungsten foil, and tungsten-copper laminate materials were supplied by collaborators at Karlsruhe Institute of Technology, Germany.

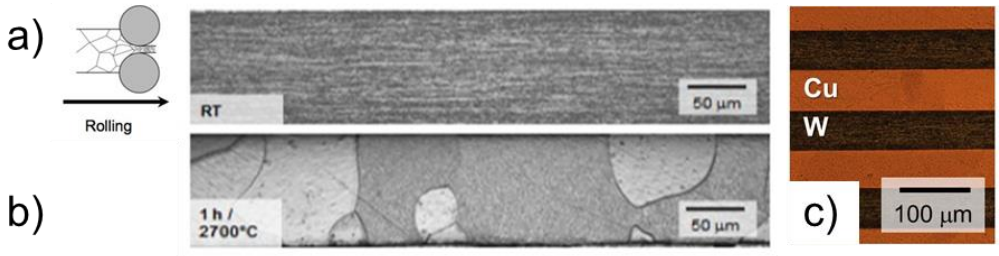

Figure 50. Microstructure before irradiation of a) wrought tungsten foil, b) annealed tungsten foil, and c) tungsten-copper laminate.

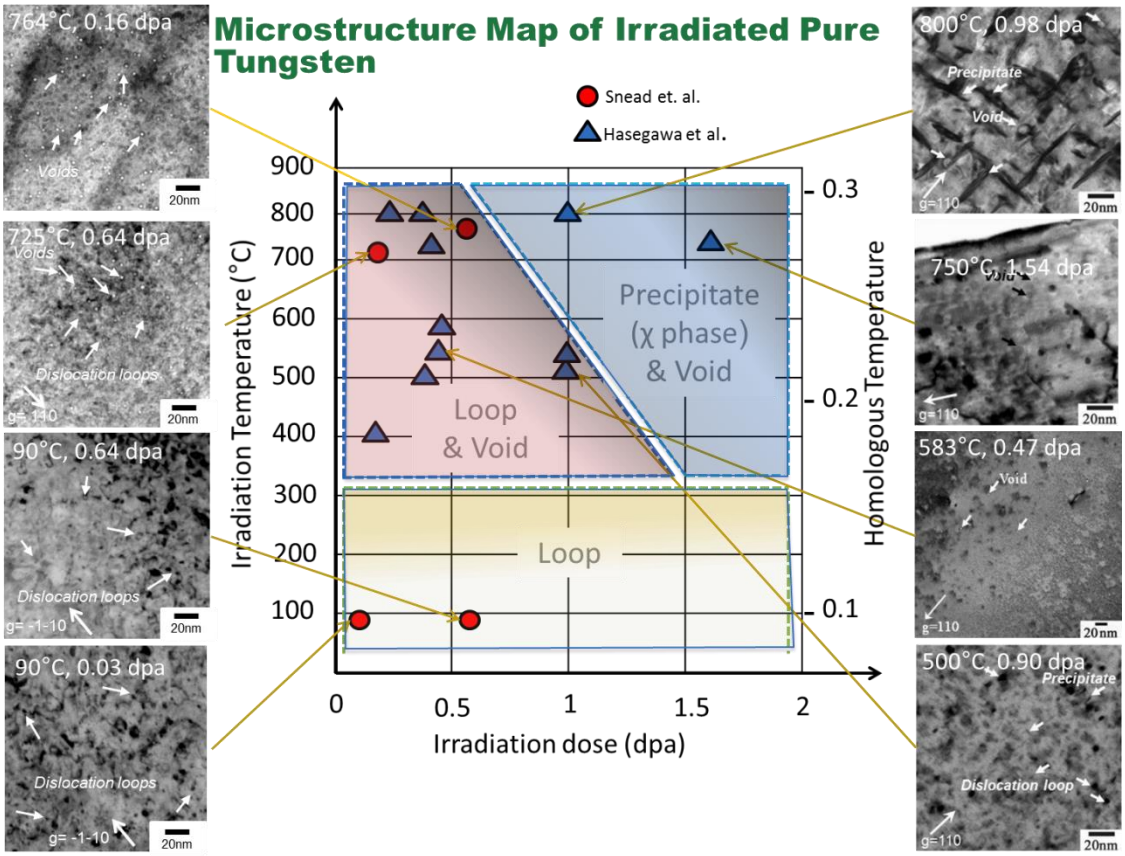

Figure 51. Comparison of irradiated tungsten defect structures.

After irradiation, microstructure and defects were analyzed using TEM. A summary of the microstructures of the single crystal tungsten samples and comparison with results for tungsten by Hasagawa et al. is presented in Figure 51. At low temperatures and low dpa, loops developed in the

tungsten. At low doses but higher temperatures radiation produced voids were observed. A sample irradiated to 2.2 dpa at ~725°C (not shown in Figure 51) showed fine needle or platelet-like rhenium-rich precipitates ranging from 2 to 28 nm with an average length of 20 nm.

A summary of dislocation loop statistics for analyzed tungsten microstructures is given in Table 5. For all types of tungsten materials, the dislocation loop size increased with increasing dose, but the most drastic increase in size was for the deformed (wrought) tungsten foil samples. The single crystal tungsten samples irradiated at higher temperatures had significantly lower loop density but larger average loop size than the samples irradiated to similar doses at lower temperatures.

Table 5. Summary of dislocation loop parameters measured in TEM analysis of single crystal, wrought foil, and annealed foil tungsten samples.

Material	Fluence in n/m² & (dpa)	Irr. Temp. in °C	Dislocation loop density (x 10^{22} m^{-3})	Average loop diameter in nm
Single Crystal -W	0.1 x 10^{25}n/m² (0.032)	80-100	2.97	4.85
Single Crystal-W	2 x 10^{25}n/m² (0.639)	80-100	4.55	4.98
Single Crystal-W	2 x 10^{25}n/m² (0.639)	724	1.41	6.37
Single Crystal-W	0.5 x 10^{25}n/m² (0.160)	764	Low	6.56
Annealed foil-W	0.1 x 10^{25}n/m² (0.032)	80-100	3.01	4.38
Annealed foil-W	2 x 10^{25}n/m² (0.639)	80-100	4.11	4.45
Deformed foil-W	0.1 x 10^{25}n/m² (0.032)	80-100	2.59	5.07
Deformed foil-W	2 x 10^{25}n/m² (0.639)	80-100	3.55	8.08

Mechanical Testing

Single crystal tungsten samples in [100] and [110] orientations were hardness tested. For both orientations, hardness increased with dose, but there was not a clear trend of hardness with increasing irradiation temperature. The indentation of the hardness test induced triaxial deformation in the samples, so there was little difference between the different orientations for the hardness values which ranged from 350-500 at low fluences below 0.5×10^{25} n/m^2 and 650-750 at fluence of 2×10^{25} n/m^2.

Single crystal tungsten samples in [110] and [100] orientations were tensile tested in an unirradiated state at temperatures from room temperature up to 650°C. In the unirradiated condition, both the [100] and [110] samples showed measurable ductility starting at 300°C. Samples of [110] tungsten irradiated to 0.006 and 0.03 dpa were tensile tested at room temperature, 90, and 300°C. At both doses, the [110] samples are also ductile at 300°C. Yield and ultimate tensile stress increased with irradiation dose. Additionally, total ductility started to decrease from 0.03 dpa. Samples of [100] single crystal tungsten that was irradiated to 0.02×10^{25} n/m^2 were also tensile tested at room temperature, 90, and 300°C. For the [100] orientation samples, some ductility is observed on the sample tested at 300°C. However, the overall elongation of the [100] sample at 300°C is much less than the [110] samples tested at the same temperature.

High temperature tensile testing was completed on samples irradiated to fluences up to 2×10^{25} n/m^2 at 300 and 500°C and for fluences up to 0.5×10^{25} n/m^2 at 650°C (Figure 52). For all temperatures, significant ductility loss results from irradiation, but there is not a direct correlation between decreased ductility and increased fluence. The samples irradiated to 2×10^{25} n/m^2 and tested at 300 and 500°C both exhibited completely brittle behavior, with the sample tested at 500°C having the highest ultimate tensile strength of all of the samples tested, approximately 1120 MPa. Ultimate tensile strength decreased from samples tested at 500°C to those tested at 650°C.

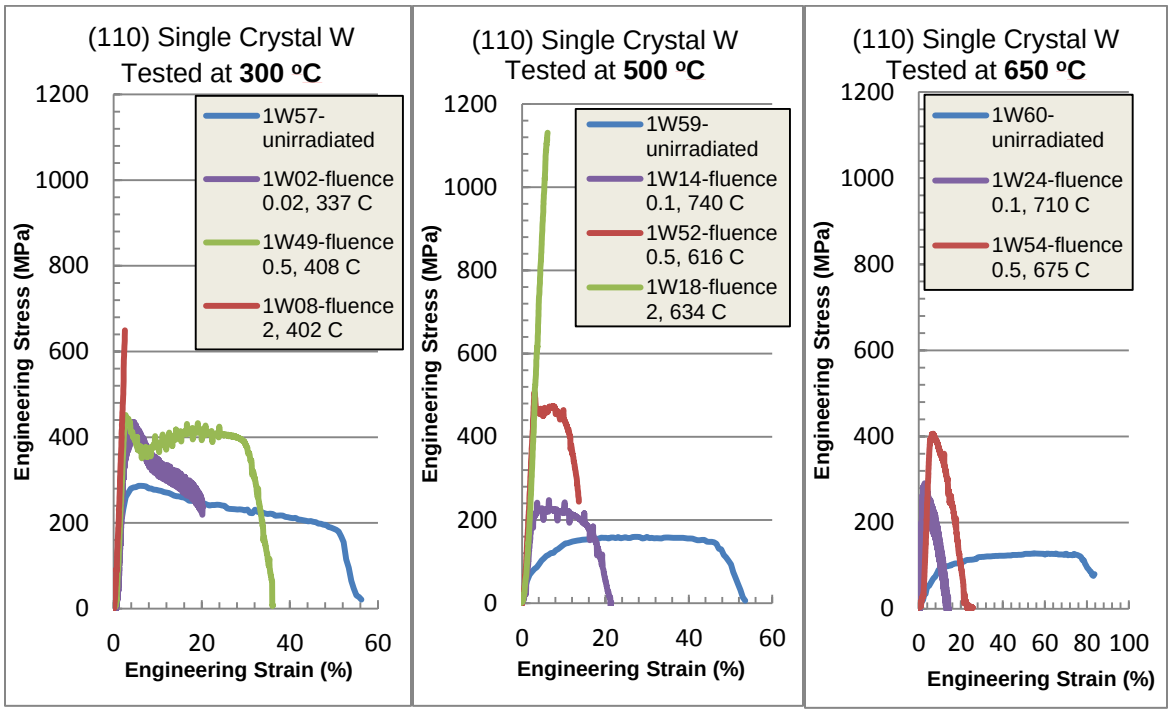

Figure 52. High temperature tensile properties at 300, 500, and 650°C. Irradiation conditions of each sample are indicated in the figure legends.

Annealing Study

A PHENIX collaboration task aims to understand how annealing changes the defect structure in irradiated tungsten and may repair the neutron irradiation damage, thereby recovering the mechanical properties to approach their unirradiated values. Samples 1W05 irradiated to 0.02×10^{25} n/m^2 at 90°C and 1W25 irradiated to 0.10×10^{25} n/m^2 at 90°C were selected for the annealing study. The samples were polished and hardness tested after irradiation. Then, each sample was annealed for one hour at 400°C. After the annealing, the hardness testing and PAS was repeated. The PAS and hardness testing will again be repeated after each one hour anneal at planned temperatures of 500, 600, 800, 1000, and 1200°C. The anneal temperatures used will be decided as the microstructure evolution is tracked.

Figure 53 compares the PAS analysis for the unirradiated, as irradiated, and after 1 hour anneal at 400°C for samples 1W05 and 1W25. The positron lifetime is related to the size of the voids in the samples. At the lower dose, sample 1W05 has a high concentration of 200 ps lifetime signal, while at the higher dose, the spectrum for sample 1W25 is starting to move to higher lifetimes. After annealing for 1 hour at 400°C, both samples showed a significant rise in the 500 ps signal.

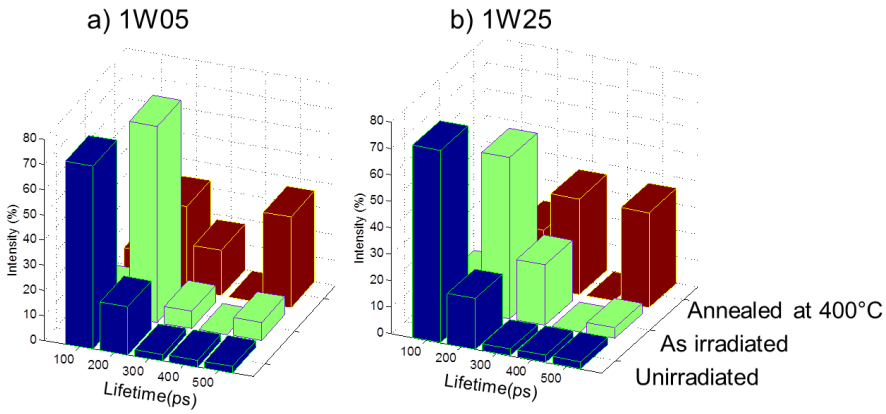

Figure 53. PAS spectra for samples a) 1W05 irradiated to 0.02×10^{25} n/m^2 at 90°C and b) 1W25 irradiated to 0.10×10^{25} n/m^2 at 90°C as irradiated and after being annealed at 400°C for 1 hour are compared to the PAS spectrum of an unirradiated single crystal tungsten sample.

The hardness results are presented in Figure 54. Both samples had nearly the same hardness value after irradiation, which was an increase from the unirradiated value. After annealing for 1 hour at 400°C, the hardness value continued to increase, with sample 1W25 irradiated to the higher fluence showing a larger increase in hardness.

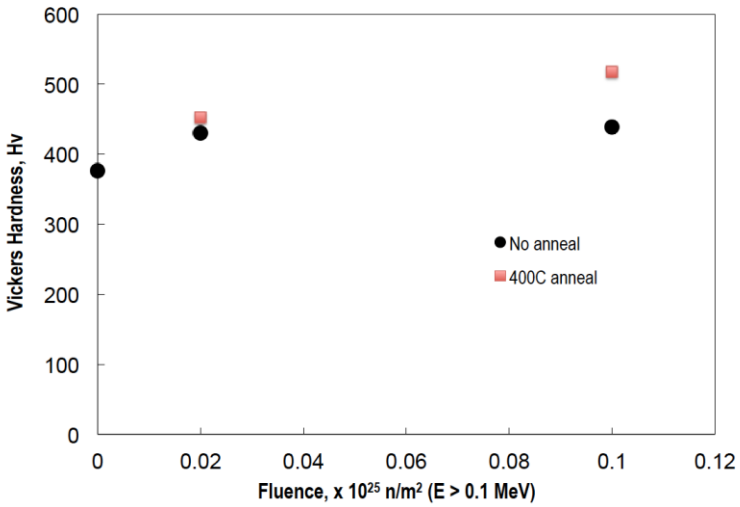

Figure 54. Hardness values for samples 1W05 irradiated to 0.02×10^{25} n/m^2 at 90°C and 1W25 irradiated to 0.10×10^{25} n/m^2 at 90°C as irradiated and after being annealed at 400°C for 1 hour.

FUTURE PLANS

High temperature tensile testing will be completed on pure tungsten and copper-tungsten laminate samples. There will be further analysis of copper-tungsten laminate samples irradiation induced defects and fracture surfaces. Samples from this set irradiated to higher fluences, 2-20×10^{25} n/m^2, E>0.1 MeV, will be examined. The annealing study will be continued to higher temperature anneals with TEM analysis to reveal the relationship between the defects, recovery processes, and hardness values.

6.4 UPGRADE OF THE ORNL PLASMA ARC LAMP FACILITY

A.S. Sabau (sabaua@ornl.gov) and L.L. Snead

OBJECTIVE

The objective of this work is to upgrade the Plasma Arc Lamps (PAL) at ORNL to enable the high-heat flux testing of a wide range of: (a) irradiated materials specimens for plasma facing components and (b) mock-up divertor components.

SUMMARY

Efforts on upgrade of the PAL facility were focused on: (1) enhancing safety during testing of irradiated specimens by reducing the footprint of the contaminated area and the level of contamination in the test section, and (2) increasing the incident heat flux from PAL.

PROGRESS AND STATUS

The enhancement of the radiation safety during testing of irradiated specimens was accomplished by employing an additional, smaller sealed chamber with a hemispherical cap, rated for vacuum systems, enclosing the cooling rod, specimen holder, and irradiated specimen (shown in Figure 55). The following activities were conducted:

- A high-vacuum system for the additional sealed chamber enclosing the specimen holder and irradiated specimen, including its own high-vacuum pumping system, was assembled and tested.
- Both the high-vacuum and low-vacuum systems were instrumented with appropriate vacuum pressure transducers.

The current status of the PAL facilities, together with the upgrade and maintenance needs, is shown in Table 6. The 750 kW PAL, rated at 4 MW/m^2, is fully operational. A preliminary diagnosis of the 300 kW PAL, rated at 27 MW/m^2, was conducted and it was decided that new electrodes are needed to further debug the system operation. The original equipment manufacturer (OEM) was contacted and it was found that electrode fabrication at the OEM was delayed due to the relocation of some of the facilities. The delivery of the electrodes is scheduled in time such that the 300 kW PAL will be operational in February 2015.

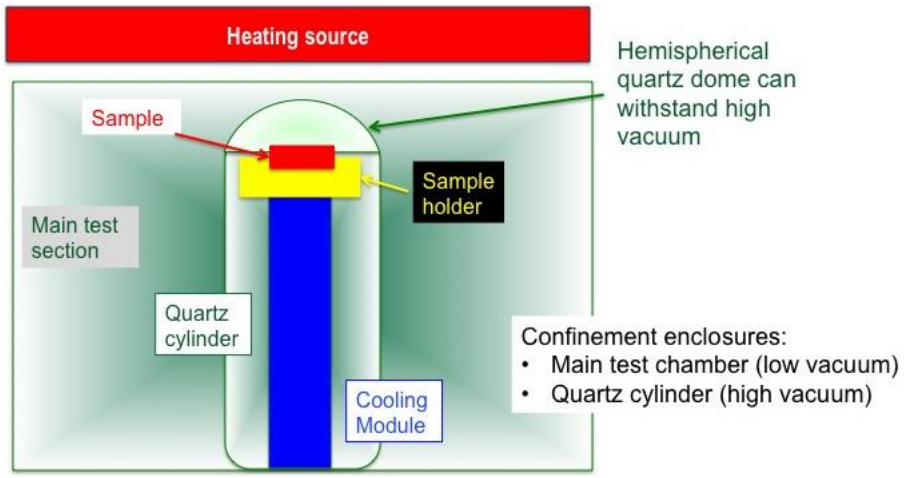

Figure 55. Schematic illustrating the use of two confinement enclosures in the test section.

Table 6. Capabilities related to the high-heat flux testing of the water-wall PAL systems available at ORNL.

System	Power [kW]	Profile of heat flux on sample	Pulse Duration [s]	Incident Max. Heat Flux [MW/m^2]	Total Heat Flux Area [cm^2]	Size @ Max Heat flux [cm^2 @ MW/m^2]	Status
Vortek 500	750	Uniform	0.02-30*	4.2	320	9x12 @4 12x14 @1	Operational
Vortek 300	300	Bell shape	0.01-30*	27	41	1x10	Need new electrodes
Vortek 300 (One Pulse)	300	Bell shape	0.001-0.005	200	41	1x10	Need new electrodes
Vortek 500	750	Bell shape (new refl.)	0.02-30*	10-15	200	2x15	New reflector, Option 2

* easily extended to 450 s by supplying additional coolant

FUTURE PLANS

The increase in the HHFT capability will be accomplished through either of the following steps:

(1) Bring online the 300 kW PAL, rated at 27 MW/m^2 with its own line-focus reflector, which is currently not operational.

(2) Employ a new line-focus reflector for the 750 kW PAL. Currently, the 750 kW PAL system uses a uniform reflector rated at over 4 MW/m^2. The line-focus reflector will distribute the 750 kW energy such that a higher maximum heat flux, e.g., 10-15 MW/m^2, will be attained but over a smaller region.

The current system pulse duration is limited by the cooling available to the PAL to 30-40 s. A 500 gallon chiller, which is adjacent to the PAL system, will be connected directly to the PAL to extend sustainable PAL pulses to 450 s.

6.5 HIGH-HEAT FLUX TESTING OF FUSION MATERIALS

A.S. Sabau (sabaua@ornl.gov), E. Ohriner, J. Kiggans, Y. Katoh, and L.L. Snead

OBJECTIVE

The objective of this work is high-heat flux testing (HHFT) of irradiated materials for plasma facing components and of mock-up divertor components using Plasma Arc Lamps (PAL). This will provide basic materials property information and constitutive equations for materials behavior in the harsh fusion environment.

SUMMARY

In FY14, two tungsten specimens and three W/F82H specimens were successfully tested at ITER-relevant high-heat flux conditions using Plasma Arc Lamp. Other efforts focused on: (1) enhancing the accuracy of the sample temperature measurement, (2) reducing oxidation of the sample during high-heat flux testing, and (3) setup of a model for the thermo-mechanical simulation of the high-heat flux testing.

PROGRESS AND STATUS

The FY14 efforts for enhancing the temperature measurement during testing of irradiated specimens included the design, fabrication, and testing of a system for bolting the specimens onto the cooling module. Bolting the specimen onto the specimen holder substrate is the best option for high-heat flux testing. However, due to the large area covered by the incident heat flux from the plasma-arc lamp, the design of the clamping fixtures had to strike the appropriate energy balance between the thermal radiation heating and limited cooling available to the fixtures, as, due to different thermal expansion, the clamping fixture cannot be bolted to both sample and cooling rod. Temperature results, which were obtained during the visit of Dr. Kazutoshi Tokunaga for the PHENIX program, indicated that accurate data was obtained by the bolted thermocouples as it showed the expected temperature range while the unbolted thermocouple indicate similar lower temperatures consistent with previous data (Figure 56b andFigure 57).

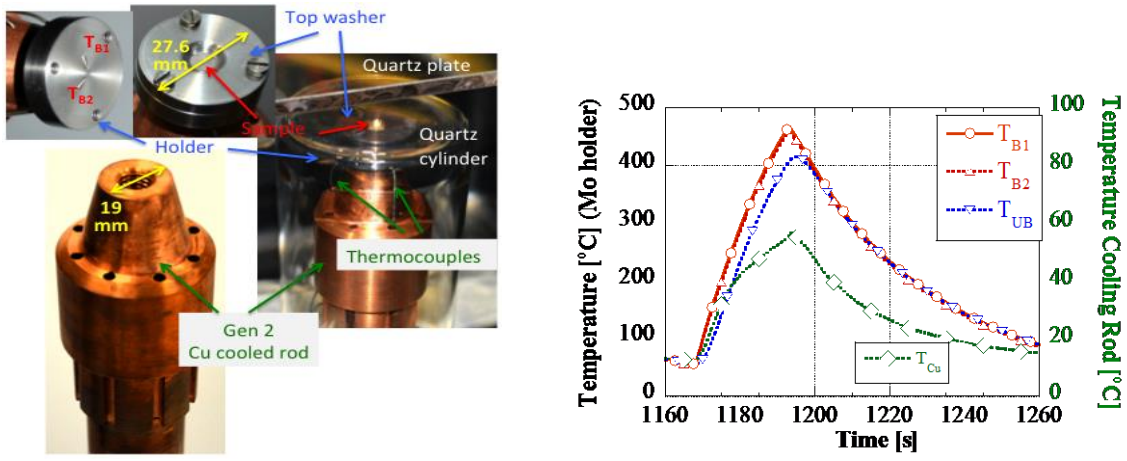

(a) (b)

Figure 56. Bolting of a W/F82H specimen (6mm diameter): (a) thermocouple location and clamped specimen fixtures, and final experimental arrangement, and (b) temperature results using bolted thermocouples (T_{B1}, T_{B2}) and an unbolted thermocouple (T_{UB}), and temperature in the cooling rod for the 12th cycle (525A lamp current, and incident heat flux of 1.4 MW/m^2).

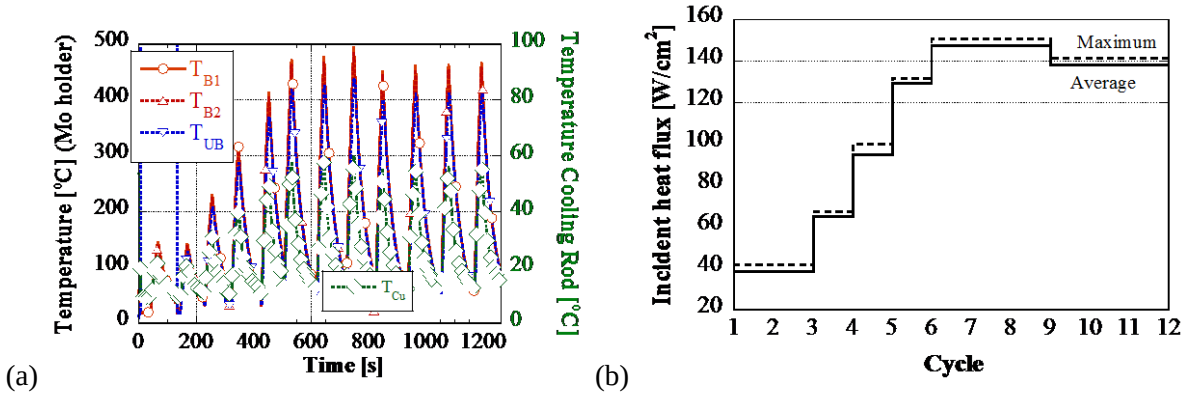

(a) (b)

Figure 57. (a) Temperature for the first 12 high-heat flux cycles for the 5th specimen (W/F82H, 6mm diameter) on the Gen 2 cooling rod. Bolted thermocouples (T_{B1}, T_{B2}) and an unbolted thermocouple (T_{UB}) (b) Incident heat fluxes for the first 12 cycles. W top surface was not oxidized while the Mo washer was slightly oxidized.

The reduction of specimen oxidation during testing of irradiated specimens was accomplished by employing an additional high-vacuum test section embedded within the main test chamber. The high-vacuum test section encloses the cooling rod, specimen holder, and irradiated specimen. The testing of an off-the-shelf sealed test section for the additional sealed chamber enclosing the specimen holder and irradiated specimen was completed (Figure 58a). Data acquired with a high-vacuum pressure transducer indicated that the absolute pressure varied during the HHFT (Figure 58b); the high pressure was found to be due to deficiencies in the sealing of the thermocouple wires. It was found that this easily available test section based on a fused glass to steel joint, would not be appropriate for the PAL setup as the steel flange heated during HHFT, and fused glass would eventually crack due to thermal cycling. Nonetheless, the sample oxidation was minimal to date.

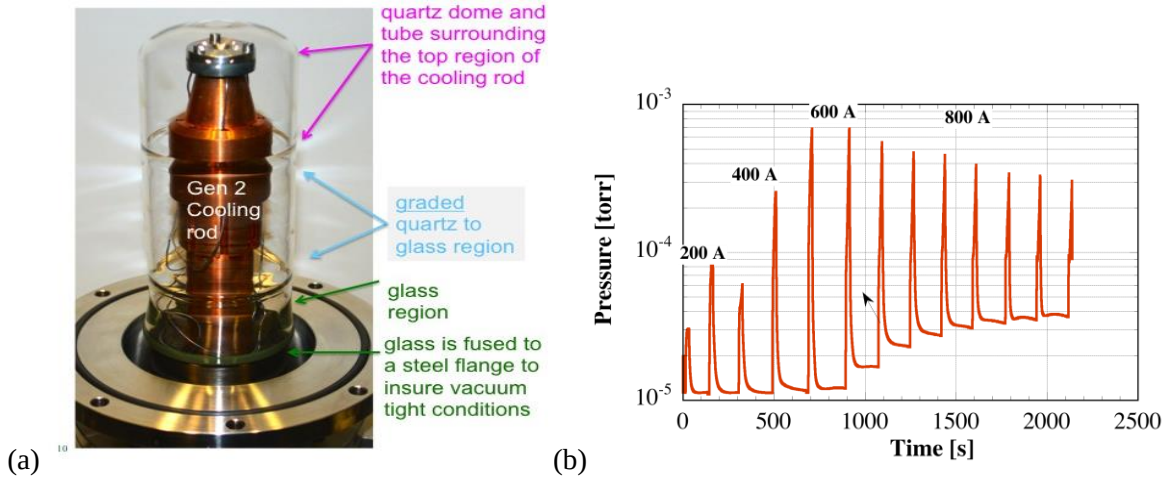

(a) (b)

Figure 58. (a) The sealed test section enclosing the specimen, and cooling rod, can be easily transported to LAMBDA for sample removal and reloading, (b) absolute pressure during a test run with an actual specimen.

FUTURE PLANS

Efforts are focused on: (1) increasing the thermal gradient through the specimen, (2) reducing oxidation of the sample during testing, and (3) conducting thermo-mechanical simulation of high-heat flux testing.

7.0 SPECIAL PURPOSE MATERIALS

7.1 IRRADIATION EFFECTS ON MICROSTRUCTURE AND OPTICAL PERFORMANCE OF MULTILAYERED DIELECTRIC MIRRORS

N.A.P. Kiran Kumar, K.J. Leonard (leonardk@ornl.gov), G.E. Jellison and L.L. Snead

OBJECTIVE

This study is an extension to our previous work on low dose dielectric mirrors. The overall objective is to elucidate the mechanisms for failure of two promising dielectric mirrors types, through an investigation of the radiation and thermally induced microstructural and optical property changes. Understanding the origin of coating damage would not only provide important information in the development of future multilayer mirrors but also helps in producing coating with improved irradiation stability.

SUMMARY

The present study was performed on specifically engineered Al_2O_3/SiO_2 and HfO_2/SiO_2 dielectric mirrors grown on sapphire substrates. They were exposed to neutron doses of 1 and 4 dpa at 458±10 K in the High Flux Isotope Reactor (HFIR). At higher doses of 1 and 4 dpa a drastic drop in optical reflectance occurred, indicating a failure of the multilayer coating. HfO_2/SiO_2 mirrors failed completely when exposed to 1 dpa, whereas the reflectance of Al_2O_3/SiO_2 mirrors reduced to 44%, eventually failing at 4 dpa. Transmission electron microscopy (TEM) examination of the Al_2O_3/SiO_2 specimens showed voids in the SiO_2 layers, which increases in size with irradiation dose. The typical size of each defect was ≈ 8 nm in 1 dpa and ≈ 42 nm in 4 dpa specimens. Buckling type delamination of the interface between the substrate and first layer was typically observed in both 1 and 4 dpa HfO_2/SiO_2 specimens. Composition changes across the layers were measured in high resolution scanning-TEM mode using energy dispersive spectroscopy. A significant interdiffusion between the film layers was observed in Al_2O_3/SiO_2 mirror and it is less evident in HfO_2/SiO_2. This investigation examines the radiation-induced failure mechanisms of these mirrors, which have demonstrated more than an order of magnitude greater tolerance for neutron irradiation than previously examined mirrors. Currently, these mirrors have extended the radiation limits such that their lifetime is consistent with inertial fusion applications, such as focusing and tuning mirrors.

PROGRESS AND STATUS

Al_2O_3/SiO_2 mirrors. Low temperature solid state diffusion phenomenon was observed in irradiated Al_2O_3/SiO_2 mirrors. Severe interdiffusion was observed in Al_2O_3/SiO_2 mirrors after HFIR neutron irradiation to 1 and 4 dpa at 458±10 K. Only a few Al_2O_3 layers were found to have Al-Si rich regions, whereas in the other Al_2O_3 layers less segregation was observed. In the 1 dpa TEM sample, the Si-rich Al_2O_3 layers were located near the substrate, film surface and also on the center layers of a multilayer stack. This may be the result of strain changes throughout the film stack, but the 4 dpa TEM sample did not show the same location preference for segregation as the 1 dpa sample. However, the cut of the sapphire was random and therefore the film strain in each sample may be slightly different. If this is true, then this is the first time this effect is being observed, as it was not seen in previously studied lower dose samples. The compositional plot in Figure 59 is representative of the region where less Al-Si segregation was observed, as the region with more segregation gives scattered results. Significant diffusion of Si was observed across the Al_2O_3/SiO_2 layer interface. Partial crystallization of α-Al_2O_3 layers to γ-Al_2O_3 could be the reason for this selective formation of Al-Si rich regions. In general, ionic material such as Al_2O_3 will have higher binding energy than covalent bonded SiO_2. Accordingly, irradiation would introduce nonstoichiometric numbers of Si, O and Al atoms, where more Si and O atoms will be displaced than Al atoms due to weak bonding structure of SiO_2. Therefore, during irradiation a gradual transformation of α-Al_2O_3 to γ-Al_2O_3 occurs by inward diffusion of excess oxygen atoms. Thus, the transformed γ-Al_2O_3, which in general is a defect structure with

cation vacancies, would act as precursors for diffusion of silicon atoms, where Si occupy the cation vacancies and stabilized the γ-Al_2O_3 phase. This implies that Al-Si rich regions form at α-Al_2O_3 to γ-Al_2O_3 transformed regions, whereas less segregation would be seen at other sites where the Al_2O_3 still shows amorphous structure.

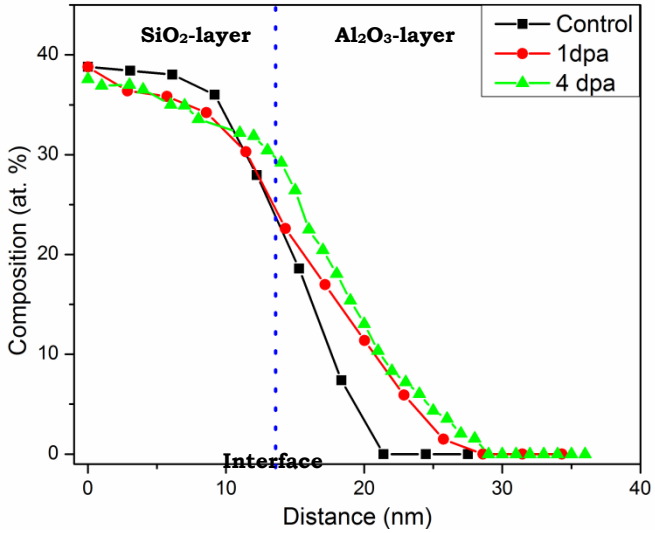

Figure 59. Energy dispersive spectrometry plots showing the change in Silicon concentration across SiO_2 -Al_2O_3 layers. (The Al/Si interdiffusion increasing with the increase in irradiation dose)

Crack formation was observed within some of the Al_2O_3 layers. It is interesting to note that no cracks were seen at the Al_2O_3/SiO_2 layer interfaces and cracks were mainly observed at Al-Si rich regions. This implies that Al-Si regions act as crack initiation sites. Although the exact mechanism involving the cracking and the role played by internal stress generated in each layer is still not clear, an imbalance between compressive stresses and tensile stresses developed in layers during irradiation could possibly lead to cracking at Al-Si rich regions. Figure 60 shows cracking of an Al_2O_3/SiO_2 mirror after exposure to 4 dpa.

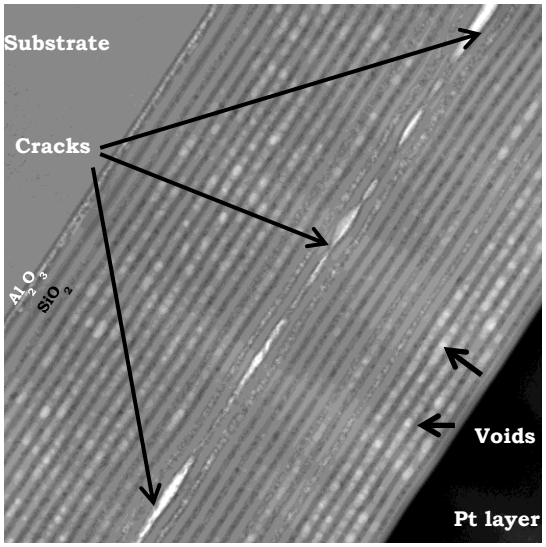

Figure 60. STEM micrograph showing the irradiation damage in Al_2O_3/SiO_2 multilayers exposed to a dose of 4dpa. (Cracks and moisture absorbed voids are pointed with arrows)

Void formation, which is sensitive to moisture pickup, was observed in SiO_2 layers of irradiated Al_2O_3/SiO_2 mirrors (see Figure 60 Figure 61). The voids in 1 dpa specimen were observed at the Al_2O_3/SiO_2 layer interface and further growth of voids occurs in the SiO_2 layer with the increase in

irradiation dose. The typical size of voids was ≈8 nm in 1 dpa and ≈ 42 nm in 4 dpa specimens. It is worth noting that voids were not observed in SiO_2 layers of HfO_2/SiO_2 mirrors exposed to the same irradiation doses. This indicates that the Al/Si interdiffusion observed in Al_2O_3/SiO_2 mirrors could possibly play a vital role in the formation these defects. At present further analysis is being performed on these defects to understand their influence on overall reflectance of the mirror.

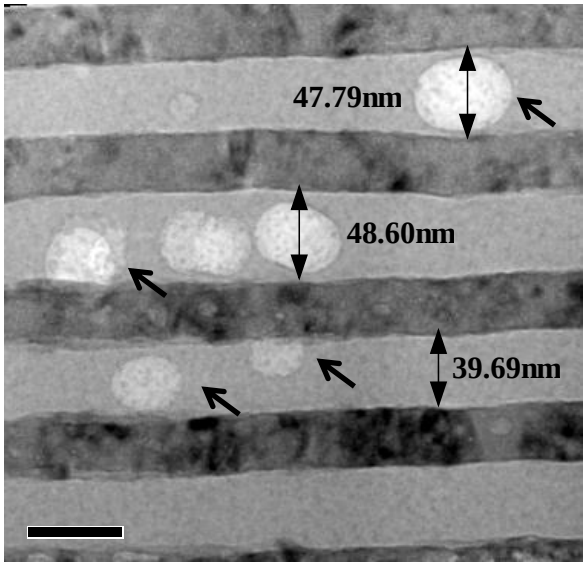

Figure 61. TEM micrographs showing the moisture-containing voids in Al_2O_3/SiO_2 mirror. (Voids are white spots marked with arrows)

HfO2/SiO$_2$ mirrors. The surface of the irradiated HfO_2/SiO_2 mirrors examined under the scanning electron microscope showed a damaged surface with much localized delamination. The current TEM specimens were prepared from the regions where the film is still attached. Figure 62 shows the low magnification TEM micrograph showing all the layers of HfO_2/SiO_2 mirror exposed to a dose of 4 dpa. In our earlier study, irradiation to 0.1 dpa produced localized amorphization of the sapphire at the interface with the first HfO_2 film. However, irradiation to 0.1 dpa was insufficient to produce delamination. This only occurred following post-irradiation annealing, with the severity of delamination increasing with annealing temperature. The additional time at temperature was sufficient to weaken the interfacial bonding to the first HfO_2 layer creating a buckled layer. These buckled layers created a defect structure that produced internal film stresses in the dielectric mirror stack on cooling. The 1 dpa irradiation provided enough damage and time at irradiation temperature to produce film buckling. However, the level of buckling was more significant than earlier observed, in that it has affected the film layers away from the substrate interface. During film buckling an amorphous Al-O layer of the sapphire forms under the buckled film. This was observed in the higher dpa films as well as in the post irradiation annealed 0.1 dpa film. The critical defect size was calculated as near 370 nm. Film buckle sizes in the 1 and 4 dpa mirrors were found to be between 100 and the critical flaw size, as they had not been large enough to delaminate the film stack, leaving a film stack from which TEM examinations could be made. Interestingly, the observed flaw sizes in TEM are close to the critical flaw size and they also created disturbance in the layers above the detached interface, leading to bending of the film.

The loss in reflectivity of HfO_2/SiO_2 mirrors exposed to 1 and 4 dpa can be attributed to the delamination mode of failure of the mirrors which lead to detachment and fracture of the multilayers. Additionally, the wrinkling of the film increased the surface roughness of the film which could diffuse the narrow reflection into a broader range of angles, diminishing the peak reflectivity of the HfO_2/SiO_2 mirrors.

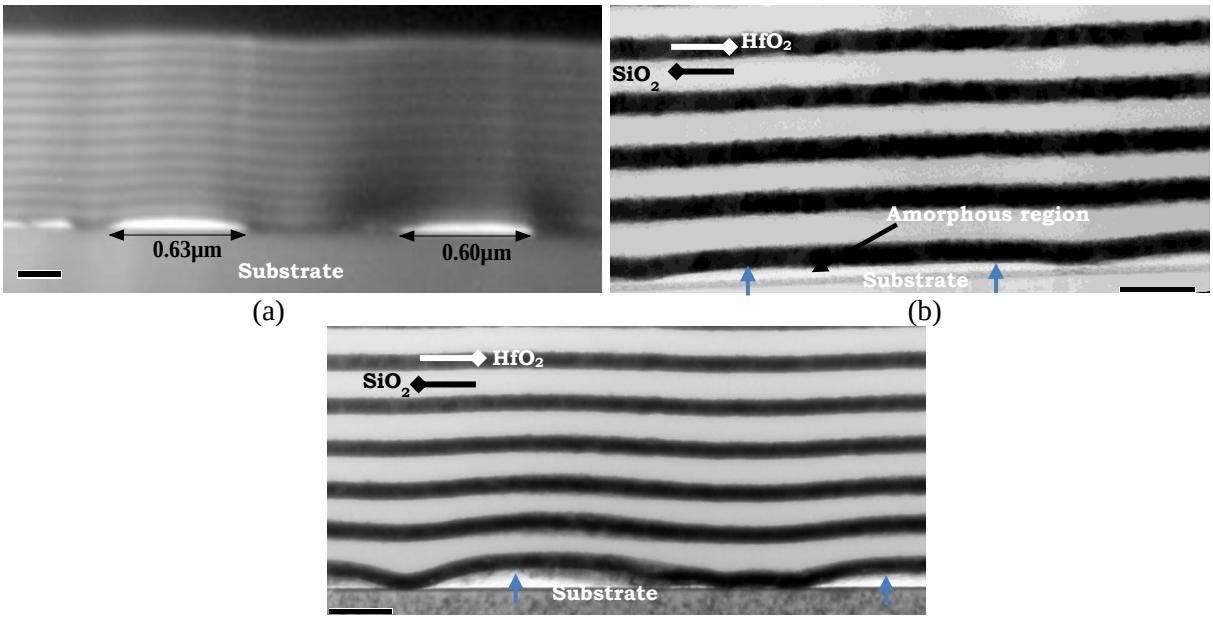

Figure 62. TEM micrographs showing a) Buckle-type delamination at the substrate layer interface and wrinkling of the subsequent film layers, b) delamination of the HfO_2 layer with amorphous layer in- the HfO_2/substrate interface, c) detachment of HfO_2 layer creating disruption in subsequent layers. (no amorphous layer at the HfO_2/substrate interface)

FUTURE PLANS

At present, we are in the process of completing this project. As expected these mirrors have failed at higher doses. The mechanism for failure of two promising mirrors has been explored. Further analysis using Electron Energy Loss Spectroscopy (EELS) is being performed on the film layers to map the moisture containing voids in order to understand the possible mechanism behind the defect formation. A publication titled "High Dose Neutron Irradiation Performance of Dielectric Mirrors" is in preparation and the results will be presented at the ANS winter conference- 21st Topical Meeting on the Technology of Fusion Energy (TOFE).

7.2 IRRADIATION RESPONSE OF NEXT GENERATION HIGH TEMPERATURE SUPERCONDUCTOR TAPES

K.J. Leonard (leonardk@ornl.gov), T. Aytug, A. Gapud, F.A. List III, W.J. Weber, and Y. Zhang

OBJECTIVE

The goal of this work is to evaluate the irradiation response of the newest generation of coated conductors based on rare earth doping of $YBa_2Cu_3O_{7-x}$ (YBCO) high temperature superconductors. The materials under investigation represent different methods for enhanced flux pinning for improved performance under externally applied magnetic fields. Current work concludes the ion irradiation work and continues with the start of neutron irradiation tests.

SUMMARY

The past year of this project concludes with a full characterization of the electrical properties of the three rare-earth doped YBCO base conductors following ion irradiation exposures. Effects of 5 MeV Ni and 25 MeV Au ion irradiation on the electrical transport current properties of the $GdBa_2Cu_3O_7$, Zr-$(Gd,Y)Ba_2Cu_3O_7$ and $(Dy,Y)Ba_2Cu_3O_7$ tapes were investigated, in view of potential applications in the irradiation environment of fusion reactors. Measurements using transport current determined the pre- and post-irradiation resistivity, critical current density, and pinning force density, yielding critical temperatures, irreversibility lines, and inferred vortex creep rates. Results show that at the irradiation damage levels tested, any detriment to as-grown pre-irradiation properties is modest; indeed in the $(Dy,Y)Ba_2Cu_3O_7$ already-superior pinning forces are enhanced, leading to higher critical currents. In general the irradiation response of the three conductors was found to be better than that of previous 1st and 2nd generation films under similar conditions.

PROGRESS AND STATUS

Figure 63 compares the change in critical density of the HTS samples as a function of dose and applied magnetic field. At low displacement damage the Zr-$(Gd,Y)Ba_2Cu_3O_7$ (Zr-YBCO) showed a decrease in critical current with magnetic field over the unirradiated value, which was regained at higher damage levels and may surpass that of the unirradiated condition as magnetic field strength is increased above 9 Tesla. The overall loss in critical current density of the Zr-YBCO material was relatively small compared to that of the $GdBa_2Cu_3O_7$ (GdBCO) conductor or that of un-doped $YBa_2Cu_3O_7$ films. The most impressive performance was observed in the $(Dy,Y)Ba_2Cu_3O_7$ (DyBCO) conductors that showed increased performance over the unirradiated base-line values with the exception of only a small loss in the high dose 25 MeV Au. However, for this irradiation condition the loss in conductor transport properties is only limited to low magnetic fields, with the irradiated conductor properties rapidly surpassing that of the unirradiated conductor for applied fields above 7 Tesla. The loss in properties of the GdBCO conductor was directly linked to the loss of Gd_2O_3 nanoparticles with increasing displacement damage.

While characterization of the electrical properties of the ion irradiated samples concludes, neutron irradiation work is beginning. During this reporting period a capsule design was developed to accommodate the HTS materials that would protect them during irradiation, ensure the lowest possible neutron irradiation temperature, and further protect them during post irradiation capsule disassembly. Irradiations are planned for the Zr-YBCO and DyBCO samples to $5x10^{17}$, $1x10^{18}$, $5x10^{18}$ and $1x10^{19}$ n/cm^2 (E>0.1 MeV). The GdBCO samples are not being included in this work based on their ion irradiation performance. The four irradiation capsules contain two specimens each of the Zr-YBCO and DyBCO samples.

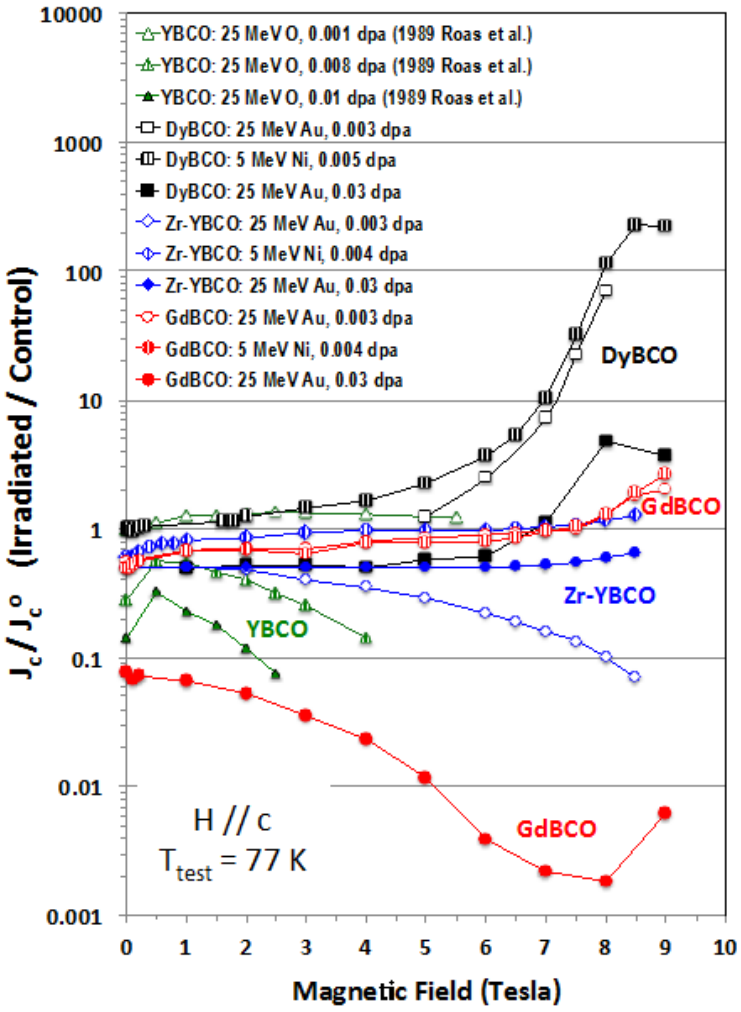

Figure 63. The change in critical current density as a function of applied magnetic field for different displacement damage of the conductors studied compared to conventional YBCO films irradiated under similar conditions.

The irradiation capsules utilize a square internal cross-section rabbit design that is loaded with internal packets containing samples. Additional samples of thermoelectric (TE) materials are also included in these irradiation capsules and will be introduced in another section of the report. These packets contain either the HTS or TE materials. The packets allow the samples to be unloaded from the rabbit capsule following dry cutting at the Irradiated Materials Examination and Testing (IMET) facility without direct handling of the HTS or TE samples by the cell manipulators. The packets can then be loaded into pigs packed with desiccant and transferred to LAMDA for further retrieval of the samples from the packets. High purity aluminum bars provide mechanical support for the flexible HTS tapes, with the tapes and bars over-wrapped with high purity aluminum foil to form a packet. The internal packet design for the $5x10^{17}$ and $5x10^{18}$ n/cm^2 (E>0.1 MeV) irradiations are similar and differ from the other two capsules in that they do not contain the additional TE samples. Examples of the two capsule configurations are shown in Figure 64Figure 65. For the $1x10^{18}$ and $1x10^{19}$ n/cm^2 (E>0.1 MeV) irradiation capsules, the thicknesses of the HTS support bars are reduced in order to accommodate a middle packet containing the TE materials. In both irradiation capsule-loading schemes, Mo-springs are inserted between the sample packets to hold the packets against the internal wall of the irradiation capsules. This ensures the lowest possible irradiation temperature for the HTS materials. SiC temperature monitors are included in the capsules and

can be loaded against the individual packets. Currently, sample loading is taking place for irradiations at the High Flux Isotope Reactor during the October 2014 operating cycle.

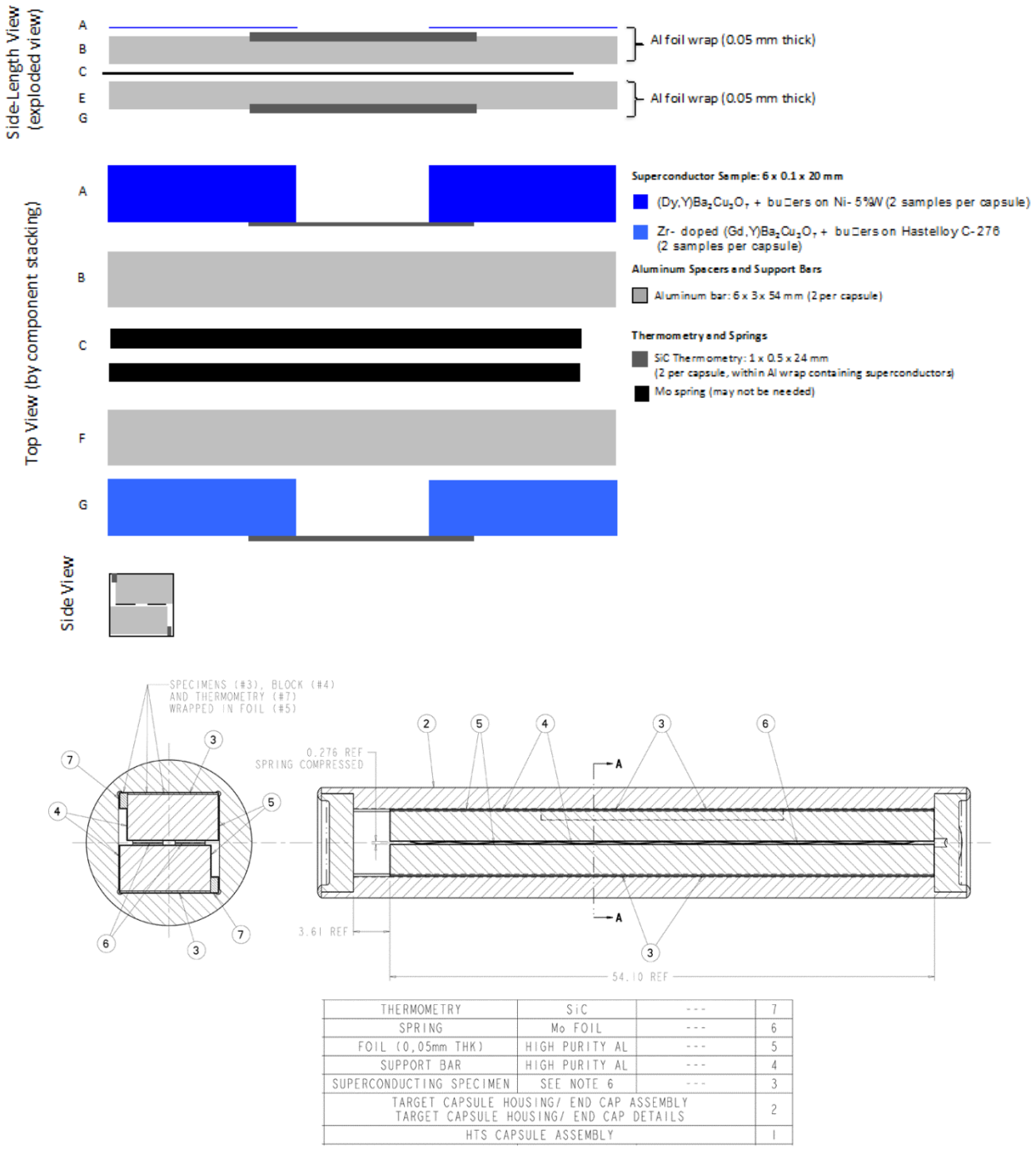

Figure 64. Schematic of the internal sample placement for the 5x10^{17} and 5x10^{18} n/cm^2 (E>0.1 MeV) capsules containing HTS samples, shown in side and top view by stacking sequence.

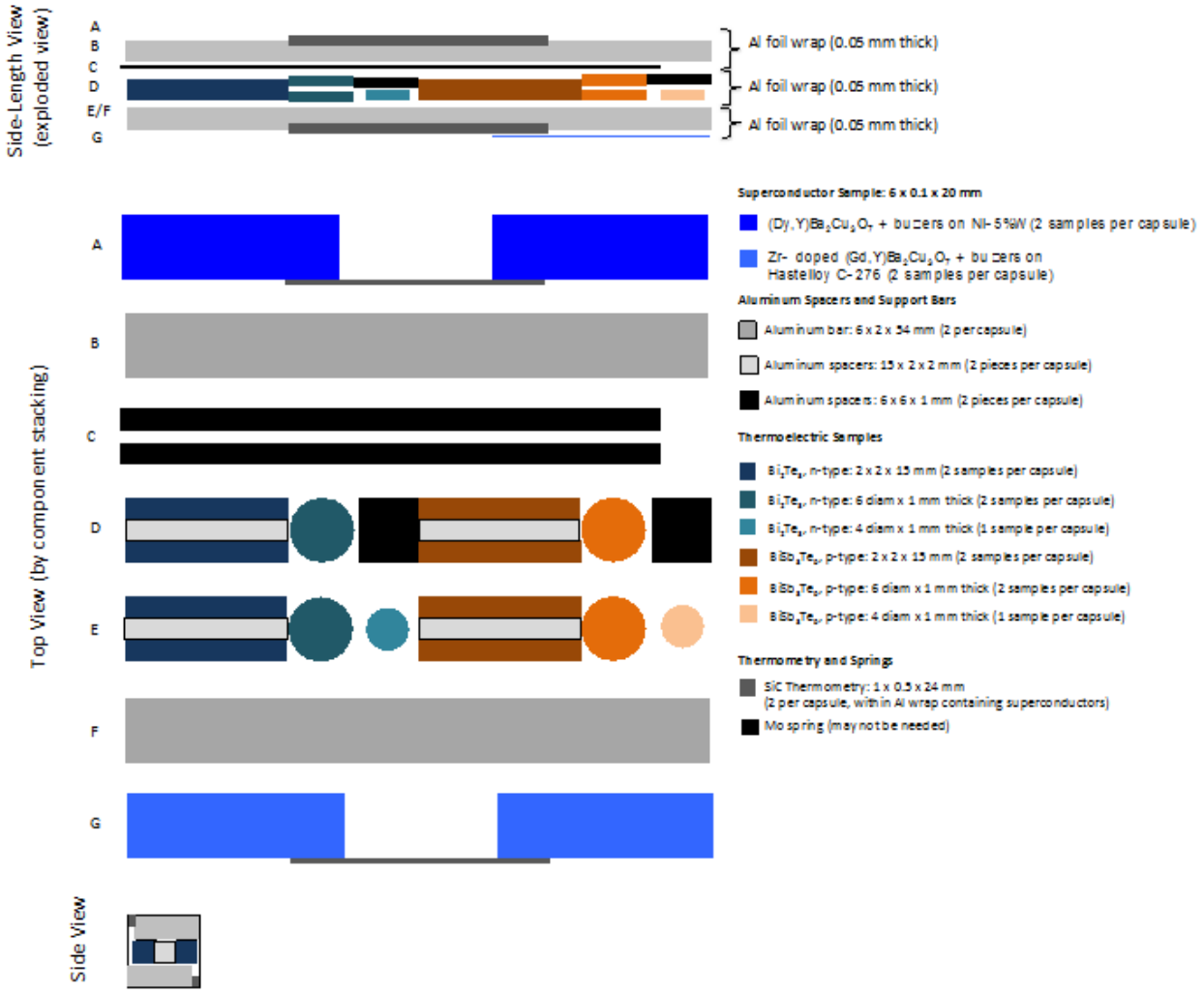

Figure 65. Schematic of the internal sample placement for the 1x10^{18} and 1x10^{19} n/cm^2 (E>0.1 MeV) capsules containing HTS and TE samples, shown in side and top view by stacking sequence.

FUTURE PLANS

The HTS and TE samples will be irradiated during the October 2014 HFIR cycle followed by capsule disassembly at both the IMET and LAMDA facilities, with electrical characterization of the materials to be performed. Following the conclusion of the electrical measurements, the HTS samples will be examined microstructurally. The damage mechanisms occurring in the neutron irradiated specimens will be compared to that occurring in the ion irradiated materials.

7.3 IRRADIATION PROPERTIES OF THERMOELECTRIC MATERIALS

K.J. Leonard (leonardk@ornl.gov) and H. Wang

OBJECTIVE

This is a preliminary scoping investigation of the performance of thermoelectric (TE) materials exposed to reactor irradiation conditions. These samples are being incorporated into the scheduled high temperature superconducting materials irradiation capsules. The TE irradiations will provide a first look at the changes in the efficiency of the materials at high neutron energy and high fluence conditions. For this initial investigation the irradiation behavior of Bi_2Te_3 and $BiSb_3Te_6$ will be examined, but the task may be later expanded to include other higher performance TE materials.

SUMMARY

The use of low power microelectronic sensors for monitoring system performance in nuclear applications is a continuing interest. To power these devices thermoelectric materials driven by waste heat may provide new monitoring capabilities not previously considered. Thermoelectric materials may also be used as passive cooling devices through the Peltier effect to maintain electronic component or sensor temperatures within design limits. However, much of the irradiation performance data for these devices has been assessed for low flux and low damage accumulation radiation environments. Therefore, a scoping experiment has been initiated to examine displacement damage effects on a pair (n and p-type) of common and well-studied TE materials. The Bi_2Te_3 compound is an n-type material, analogous to semiconductors where electrons are the majority carriers and the holes are minority carriers. The reverse of this is the p-type $BiSb_3Te_6$ material also included in this work. While TE materials with greater performance or capability for operating at higher temperatures are available, the goal of this work is to establish an initial understanding of the role both displacement damage and transmutation doping may have on the figure of merit (ZT), the dimensionless value that is a measure of materials ability to efficiently produce thermoelectric power. The figure of merit is given by,

$$ZT = \frac{\sigma S^2 T}{\lambda}$$

where, σ is the electrical conductivity, S is the Seebeck coefficient, λ is thermal conductivity and T is temperature.

PROGRESS AND STATUS

The TE materials are being included in two of the four planned irradiation capsules for the high temperature superconducting (HTS) materials investigation in another part of the ORNL Fusion Materials Program. The TE materials will be contained in the capsules exposed to $1x10^{18}$ and $1x10^{19}$ n/cm^2 (E>0.1MeV) fluences. The Bi_2Te_3 and $BiSb_3Te_6$ test samples are an assortment of disc and rod shapes that are sized for post-irradiation measurements of heat capacity, thermal diffusivity, electrical conductivity and Seebeck coefficient. Table 7 lists the loading sequence of the TE materials, and the type and size of samples in each of the four planned HTS irradiation capsules. The internal loading configuration of the samples within the irradiation capsules is illustrated and further detailed within section 7.2 of this annual report that discusses the HTS materials.

The TE and HTS samples are currently undergoing capsule loading and assembly and are slated for insertion into the hydraulic tube rabbit facility during the October 2014 HFIR cycle.

FUTURE PLANS

Post-irradiation examination will be performed in LAMDA and will utilize the ZEM-5 instrument as well as laser flash diffusivity instruments. The TE samples may be delayed in reaching LAMDA compared to their HTS counterparts due to the possible need for extending the cooling period for sample activity to be low enough for handling in the LAMDA environment. Calculations are being performed to determine the expected sample activity.

Pending results of this initial scoping exercise on Bi_2Te_3 and $BiSb_3Te_6$ samples, other TE type of materials that have higher ZT values may be studied, including doped skutterudite structures or oxide-based thermoelectrics. However, these materials typically contain Co, which will make post-irradiation examination difficult, unless an alternative compound is identified. One method of improving ZT and avoiding Co is through engineered nanostructured materials, which may include simple binary-layered Bi_2Te_3/Sb_2Te_3 thin film layer on a substrate and may offer a more favorable material for use in nuclear environments.

Table 7. The capsule number, irradiation condition, sample type and ID numbers for specimens in the planned HFIR irradiations set for the October cycle.

Capsule	Fluence (n/cm^2)	Sample ID	Sample type	Composition	Size
HTS-1	5x10^{17}	A-27	Superconductor	DyBCO	6 x 0.1 x 20 mm
		A-28	Superconductor	DyBCO	6 x 0.1 x 20 mm
		S-18	Superconductor	Zr-YBCO	6 x 0.1 x 20 mm
		S-19	Superconductor	Zr-YBCO	6 x 0.1 x 20 mm
HTS-2	1x10^{18}	A-29	Superconductor	DyBCO	6 x 0.1 x 20 mm
		A-30	Superconductor	DyBCO	6 x 0.1 x 20 mm
		BTN-1	Thermelectric n-type	Bi_2Te_3	2 x 2 x 15 mm
		BTN-2	Thermelectric n-type	Bi_2Te_3	2 x 2 x 15 mm
		BTN-3	Thermelectric n-type	Bi_2Te_3	6 mm diam x 1 mm
		BTN-4	Thermelectric n-type	Bi_2Te_3	6 mm diam x 1 mm
		BTN-5	Thermelectric n-type	Bi_2Te_3	4 mm diam x 1 mm
		BTP-1	Thermelectric p-type	$BiSb_2Te_6$	2 x 2 x 15 mm
		BTP-2	Thermelectric p-type	$BiSb_2Te_6$	2 x 2 x 15 mm
		BTP-3	Thermelectric p-type	$BiSb_2Te_6$	6 mm diam x 1 mm
		BTP-4	Thermelectric p-type	$BiSb_2Te_6$	6 mm diam x 1 mm
		BTP-5	Thermelectric p-type	$BiSb_2Te_6$	4 mm diam x 1 mm
		S-20	Superconductor	Zr-YBCO	6 x 0.1 x 20 mm
		S-21	Superconductor	Zr-YBCO	6 x 0.1 x 20 mm
HTS-3	5x10^{18}	A-31	Superconductor	DyBCO	6 x 0.1 x 20 mm
		A-32	Superconductor	DyBCO	6 x 0.1 x 20 mm
		S-22	Superconductor	Zr-YBCO	6 x 0.1 x 20 mm
		S-23	Superconductor	Zr-YBCO	6 x 0.1 x 20 mm
HTS-4	1x10^{19}	A-33	Superconductor	DyBCO	6 x 0.1 x 20 mm
		A-34	Superconductor	DyBCO	6 x 0.1 x 20 mm
		BTN-6	Thermelectric n-type	Bi_2Te_3	2 x 2 x 15 mm
		BTN-7	Thermelectric n-type	Bi_2Te_3	2 x 2 x 15 mm
		BTN-8	Thermelectric n-type	Bi_2Te_3	6 mm diam x 1 mm
		BTN-9	Thermelectric n-type	Bi_2Te_3	6 mm diam x 1 mm
		BTN-10	Thermelectric n-type	Bi_2Te_3	4 mm diam x 1 mm
		BTP-6	Thermelectric p-type	$BiSb_2Te_6$	2 x 2 x 15 mm
		BTP-7	Thermelectric p-type	$BiSb_2Te_6$	2 x 2 x 15 mm
		BTP-8	Thermelectric p-type	$BiSb_2Te_6$	6 mm diam x 1 mm
		BTP-9	Thermelectric p-type	$BiSb_2Te_6$	6 mm diam x 1 mm
		BTP-10	Thermelectric p-type	$BiSb_2Te_6$	4 mm diam x 1 mm
		S-24	Superconductor	Zr-YBCO	6 x 0.1 x 20 mm
		S-25	Superconductor	Zr-YBCO	6 x 0.1 x 20 mm

8.0 COMPUTATIONAL MATERIALS SCIENCE

8.1 STRENGTHENING DUE TO HARD OBSTACLES IN FERRITIC ALLOYS

Y.N. Osetskiy (osetskiyyn@ornl.gov) and R.E. Stoller

OBJECTIVE

The purpose of this research is to understand atomic level hardening mechanisms in materials with rigid precipitates such as ODS alloys. Because of the lack of interatomic potentials, direct modeling of such systems is not yet possible. We therefore have developed a model of rigid uncompressible precipitates embedded in a metallic matrix interacting via an empirical EAM potential.

SUMMARY

We have developed a molecular dynamics (MD) based model to simulated dislocation dynamics in the presence of rigid, impenetrable inclusions. These inclusions simulate rigid oxide particles as obstacles to dislocation motion. Interactions between a moving edge dislocation ½<111>{110} and rigid inclusions was modeled over a wide range of parameters such as inclusion size, temperature, strain rate and interaction geometry. It was found that interaction mechanism depends strongly on the inclusion size and interaction geometry. Some new mechanisms were observed and are now under detailed investigation.

PROGRESS AND STATUS

For the last ten months we have continued modeling of the largest at that time obstacles, 6 nm in diameter and have started a larger, 7 nm inclusion. The necessity of this came from the observation that the mechanism of interaction between a moving dislocation and rigid inclusion depends very much on the obstacle size. More precisely it depends on the inclusion curvature and therefore on the cross-section of the inclusion in the dislocation glide plane. We therefore investigate this particular effect and have found that it is more important for large inclusions. The results were treated and we have found that the obstacle critical resolved shear stress (CRSS) follows the dependence versus the effective obstacle size in the dislocation slip plane. A certain asymmetry was found for the obstacle above the slip plane, which is stronger than the equivalent obstacle below the slip plane. An example of CRSS dependence as a function of the interaction geometry is presented in Figure 66. We explain this by the fact that interatomic potentials are asymmetric as well and the absolute value of forces generated during compression is higher than that for tension and therefore affects the obstacle strength through the compression and tension regions around edge dislocations. It is interesting that not only CRSS depends on the interaction geometry but also the interaction mechanism itself. This is illustrated in Figure 67 and Figure 68. Thus Figure 67 shows the edge dislocation ½<111>(110) and 6 nm inclusion with its equator in the dislocation slip plane, (a) before and (b) after interaction. The Orowan sheared loop shown in Figure 67b is formed due to this interaction. This mechanism provides the maximum strengthening as shown in Figure 66.

Figure 68 show the same obstacle but in the configuration when its equator is half of the radius below the dislocation slip plane and the corresponding CRSS in Fig.1 is for R=0.5. The position of slip plane can be clearly seen on Figure 68a as a red line and it moves from the left to right.

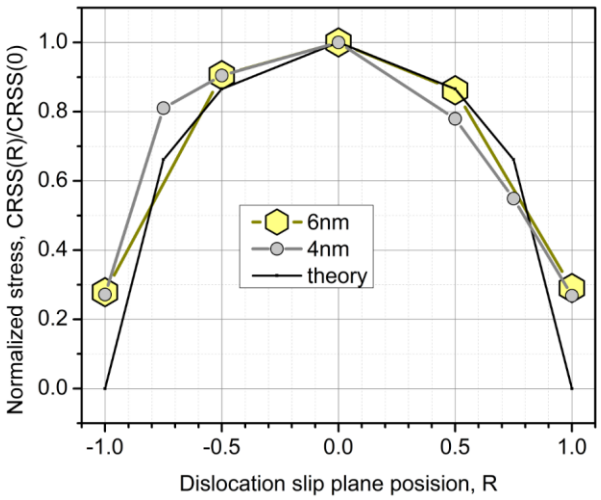

Figure 66. Dependence of the CRSS on distance between the inclusion equator and dislocation slip plane. Black solid line shows the estimation based on the area of the corresponding cross-section through the inclusion.

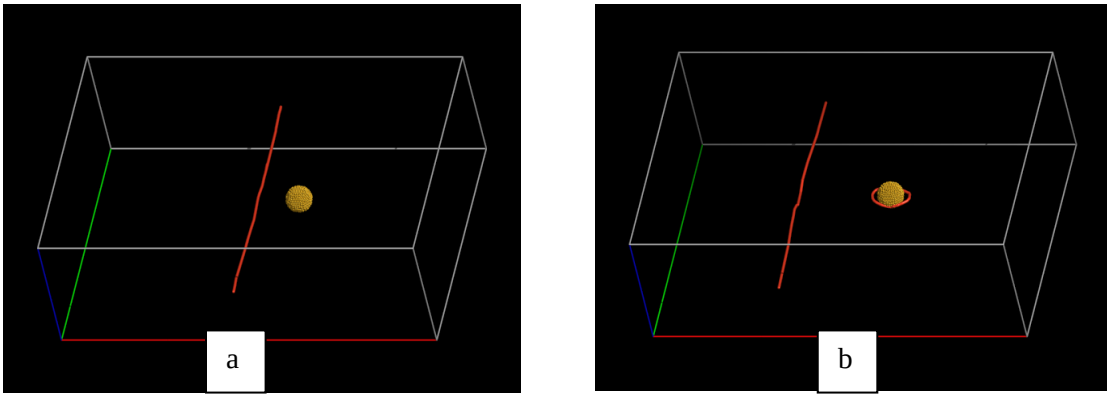

Figure 67. Edge dislocation ½<111>(110) and 6 nm inclusion with its equator in the dislocation slip plane before (a) and after (b) interaction. The Orowan sheared loops shown on the right is formed due to this interaction. This mechanism provides the maximum strengthening.

The configuration obtained after the dislocation bypassed the inclusion is shown in Figure 68b. One should take into account that in this figure the dislocation is seen again on the left side of the obstacle where it appeared due to periodic boundary conditions in the slip plane. A small interstitial loop is left behind near the inclusion and the corresponding negative superjog was created on the dislocation line. This can be seen more clearly in Figure 68c where the view along the dislocation Burgers vector is shown. The loops size and shape is approximately equivalent to the upper part of the inclusion above the dislocation slip plane. These examples demonstrate clearly how the interaction mechanism depends on the interaction geometry.

The mechanism in Figure 68 is observed for the first time and was yet not described in the literature. The usual deformation mechanisms result in formation vacancy-type defects because this is energetically more favorable. Formation of interstitial-type defects occurred on these inclusions because they are very strong obstacles. In fact, they are the obstacles of maximum possible strength.

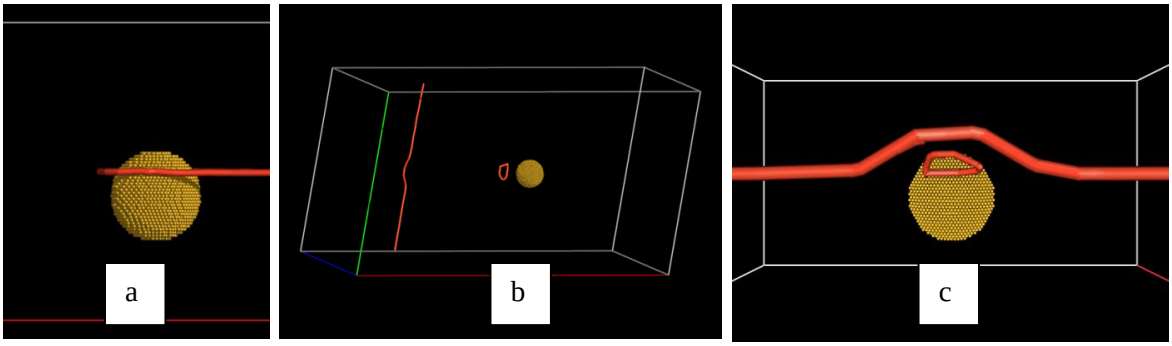

Figure 68. Edge dislocation ½<111>(110) and 6 nm inclusion with its equator half of the inclusion radius below the dislocation slip plane. Left– view of the inclusion along the dislocation slip plane where red line is the bowing around the inclusion. Dislocation glides from left to right. Centre – total view to the crystal after the interaction. Dislocation has a negative superjog created due to an interstitial dislocation loop left behind at the inclusion. Right – view along the dislocation Burgers vector.

FUTURE PLANS

Over the next year of the project we are going to investigate these mechanisms in more details because we think they should have important influence on the creep behavior of ODS alloys.
We have also concluded that 6 nm obstacle might be too small for the treatment within the continuum approach to find the general description of the effect. So we have launched a new series of deformations for a 7 nm rigid particle. The full set of parameters to be studied includes temperature: 100, 300, 450 and 600 K, different levels of the dislocation slip plane relatively to the particle equator: 0, +-0.5 R, +-0.75 R and +-R, where R=7 nm is the particle radius and applied strain rates: 1, 2 and 5 in units of 10^6 s^{-1}.

Visualization of the interaction mechanisms is an important part of the whole study for it allows understanding of the mechanism details. We therefore will continue improving existing and developing new visualization techniques.

After we understand the strongest and the most frequent mechanisms we are going to search for them experimentally using *in situ* or/and interrupted deformation techniques to directly compare computational and experimental mechanisms.

REFERENCES

1. X.L. Wang, C.T. Liu, U. Keiderling, A.D. Stoica, L. Yang, M.K. Miller, C.L. Fu, D. Ma, K. An, "Unusual thermal stability of nano-structured ferritic alloys", *Journal of Alloys and Compounds* 529 (2012) 96– 101.
2. M.K. Miller, D.T. Hoelzer, E.A. Kenik, K.F. Russel, "Stability of ferritic MA/ODS alloys at high temperatures", *Intermetallics* 13 (2005) 387–392.
3. Fu, C. L., Krcmar, M., Painter, G. S. & Chen, X. Q. "Vacancy mechanism of high oxygen solubility and nucleation of stable oxygen-enriched clusters in Fe". *Phys. Rev. Lett.* 99, 225502 (2007).
4. Brodrick, D.J. Hepburn, G.J. Ackland, "Mechanism for radiation damage resistance in yttrium oxide dispersion strengthened steels", *Journal of Nuclear Materials* 445 (2014) 291–297.

8.2 AN ATOMISTIC DESCRIPTION OF HELIUM BEHAVIOR IN STEELS

R. E. Stoller (stollerre@ornl.gov) and Yu. N. Osetskiy

OBJECTIVE

The objective of this research is to determine the equation of state of helium in radiation-induced bubbles in iron-based alloys. Properties of He-bubbles significantly affect the evolution of the microstructure and mechanical properties under radiation damage conditions.

SUMMARY

An equation of state that accurately reproduces the pressure-volume relationship of helium is necessary to understand and predict the behavior of He-vacancy defects in irradiated materials. We have used ab initio calculations to determine the energetics of helium-vacancy clusters and applied the results to develop a new three-body interatomic potential that describes the behavior of helium in iron. The potential was employed in molecular dynamics simulations to determine the conditions for mechanical equilibrium between small helium-stabilized bubbles and an iron matrix, and to systematically map the pressure-volume relationship for the bubbles at a range of temperatures. These atomistic results are compared to an existing equation of state and a modification is proposed for bubbles with high helium densities.

PROGRESS AND STATUS

Molecular dynamics (MD) simulations have been used to characterize the pressure-volume relationship of helium in small bubbles at a range of temperatures in order to develop an improved equation of state (EOS). The EOS for bubbles in solids is material dependent because the repulsive interaction between helium and the lattice atoms depends on the material. The ORNL-developed EOS [1] based on *ab initio* calculations [2] accounts for the He-Fe repulsion, and was used in conjunction with the iron interatomic potential developed by Ackland and co-workers [3]. The simulations were carried out at constant volume using a bcc iron system size of 128,000 iron atoms (40 lattice parameters cubed) containing helium-filled bubbles consisting of 9 to 44,399 vacancies, corresponding to nominal radii (r_b) from ~0.25 nm to ~5.0 nm. The appropriate lattice parameter was used for each simulation temperature in the range from 300 to 1000 K. The helium density in the bubbles was the primary simulation variable, with the density expressed as either the helium-to-vacancy ratio or the number of helium atoms per unit volume.

Because of the strong He-Fe repulsion, the time-averaged positions of the He atoms in the bubbles reveal a small gap between the Fe surface and He atoms in the bubble. This reduces the effective bubble volume. In addition, the nominal bubble volume is calculated based on the number of vacancies in the bubble and the atomic volume, i.e. $V_b = n_v \Omega$, and not as a sphere of radius rb. The importance of both the gap and the deviation from being spherical are increased bubbles. For each simulation condition, the simulations were carried out long enough to obtain an accurate determination of the bubble pressure as illustrated in Figure 69. The He compressibility is defined as the ratio of the bubble pressure obtained from the MD simulations to the ideal gas pressure for the same bubble size, temperature, and helium content. The compressibility of bubbles in mechanical equilibrium with the iron lattice is shown as a function of the He/vacancy ratio in Figure 70.

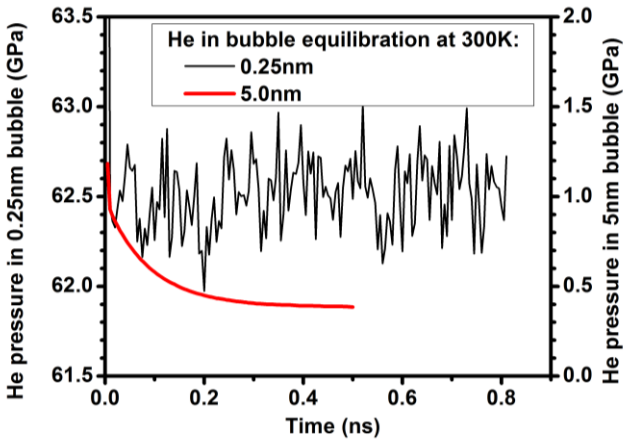

Figure 69. Typical bubble equilibration times at 300K for bubbles with radii of 0.25 and 5.0 nm.

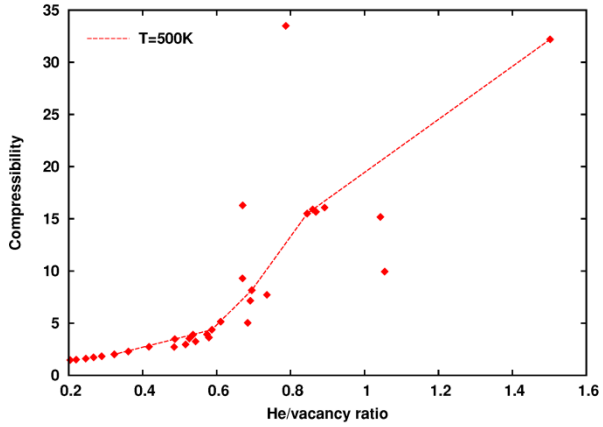

Figure 70. Compressibility of bubbles in mechanical equilibrium with the iron lattice as a function of He/vacancy ratio, all temperatures and radii are includes and line connects at values at 500K.

All temperatures are included for each radius and the line connects values at 500 K as a guide to the eye. There is a clear increase in scatter for He/vacancy ratios greater than about 0.7 (compressibilites greater than about 8) in Figure 70. Other analysis indicates that this may be related to a He phase change from gas to liquid.

Brearley and MacInnes [4] developed a hard-sphere equation of state (HSEOS) for helium based on the formalism of Carnahan and Starling [5]. They parameterized the potential to obtain good agreement between compressibilities (Z) and a somewhat limited amount of relatively low temperature (~65°C), high pressure helium data. The equation of state has the following form:

$$Z = \frac{PV}{mkT} = \frac{(1 + y + y^2 - y^3)}{(1 - y)^3} \quad (1)$$

where y is proportional to the helium density: $y=(\pi dg^3/6)\cdot(m_{He}/V_b)$, d_g is the effective hard sphere

diameter of the He atoms, m_{He} is the number of He atoms, and V_b is the bubble volume in nm^3. The hard sphere diameter is determined by the interatomic potential assumed; Brearley and MacInnes employed a modified Buckingham potential leading to a four-parameter expression for d_g=0.3135 [0.8542 - 0.03996 ln(T/9.16 K)] nm.

Since the ORNL He-Fe potential was used in the MD simulations, the refitting of the HSEOS to improve agreement with the MD results involved reparameterizing the hard sphere expression in the previous paragraph which was based on the Buckingham potential, and including the effect of the He-Fe gap mentioned above. Table 8 lists the original and modified parameter values that were obtained using the non-linear generalized reduced gradient method that has been implemented in the Microsoft Excel Solver function, and Figure 71 shows a comparison of the MD results with the HSEOS prediction using both the original and new parameters. A perfect fit would follow the one-to-one line in Figure 71.

Table 8. Coefficients obtained from fitting the HSEOS to the MD results

Fitting Parameter	Original HSEOS	Refit HSEOS
a_1	*0.3135*	0.319332
a_2	*0.8542*	0.865456
a_3	*0.03996*	0.041802
a_4	9.16	9.228038
Δr	n/a	0.057389
Hard-sphere gas atom diameter: $d_g=a_1\,[a_2 - a_3\,ln(T(K)/a_4)$, *T= temperature in K*		
Effective reduced bubble volume: $V_b^{eff} / V_b = (r_b-\Delta r)^3/ r_b^3$		

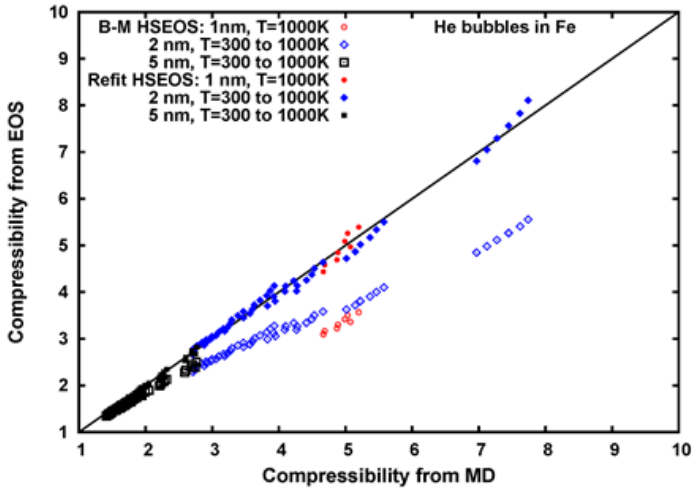

Figure 71. Comparison of compressibility obtained from MD simulations with those calculated using the Brearley-MacInnes HSEOS [4] with the original parameters and those obtained from the non-linear fitting process discussed in the text.

The data in Figure 71 demonstrate the significant improvement obtained with the new parameters in the HSEOS. However, for higher compressibilites in small bubbles the agreement is much worse. As

mentioned above, it is believed that this is due to a phase change of the helium from gas to liquid. Work is underway to verify this phase change and find an appropriate method of representing the higher compressibility for higher He/vacancy ratios.

FUTURE PLANS

Molecular dynamics simulations are underway to determine the critical He/vacancy ratio for helium phase changes in order to explain the behavior of the smallest bubbles with high pressures for which the equation of state does not provide a good description. The simulations involve very long simulation times in order to determine whether the He diffusion in the bubbles is characteristic of the gaseous or liquid phase. Strategies for extrapolating the equation of state into this regime are also being investigated.

REFERENCES

1. R. E. Stoller, S. I. Golubov, P. J. Kamenski, T. Seletskaia, and Yu. N. Osetsky, Philos. Mag. 90 (2010) 923-934.
2. T. Seletskaia, Yu. N. Osetsky, R. E. Stoller, and G. M. Stocks, Phys. Rev. Lett. 94 (2005) 046403:1-4.
3. G. J. Ackland, D. J. Bacon, A. F. Calder, T. Harry, Philos. Mag. A 75 (1997) 713-732.
4. I. R. Brearley and D. A. MacInnes, J. Nucl. Mater. 95 (1980) 239-252.
5. N. F. Carnahan and K. E. Starling, J. Chem. Phys. 51 (1969) 635-636.

8.3 MOLECULAR DYNAMICS MODELING OF ATOMIC DISPLACEMENT CASCADES IN 3C-SiC.

G.D Samolyuk (samolyukgd@ornl.gov), Y. N. Osetskiy and R. E. Stoller

OBJECTIVE

The objective of this effort is to characterize the nature of primary radiation damage in SiC to provide a basis for understanding the experimentally observed fluence-temperature map of the irradiated microstructures. Recently reported results demonstrated that the most commonly used interatomic potentials (Tersoff [1]) are inconsistent with *ab initio* calculations of defect energetics. In order to demonstrate the sensitivity of cascade recombination to the value of barrier recombination, additional cascade simulations have been done with the newly developed Gao-Weber potential [2].

SUMMARY

We demonstrated that the most commonly used interatomic potentials are inconsistent with *ab initio* calculations of defect energetics. Both the Tersoff potential used in this work and a modified embedded atom method (MEAM) potential reveal a barrier to recombination which is much higher than the DFT results. The barrier obtained with a newer potential by Gao and Weber is closer to the DFT result but the overall energy landscape is significantly different. This difference results in a significant difference in the cascade production of points defects. We have completed both 10 keV and 50 keV pka energy cascade simulations in SiC at temperatures equal to 300, 600, 900 and 1200 K. In a contrast to Tersoff potential, the GW potential produces almost twice as many C vacancies and interstitials at the time of maximum disorder (~0.2 ps) but only about 25% more stable defects at the end of the simulation. Only about 20% of the carbon defects produced with the Tersoff potential recombine during the in-cascade annealing phase, while about 60% recombine with the GW potential. The GW potential appears to give a more realistic description of cascade dynamics in SiC, but still has some shortcomings when the defect migration barriers are compared to the *ab initio* results.

PROGRESS AND STATUS

In the initial phase of the project, the GW potential code was introduced in the LAMMS molecular dynamics (MD) package [3]. The good agreement between MD and first-principles calculated formation energies of twelve most typical defects was demonstrated. To improve the weak repulsion of GW potential at short distances we joined GW with the well-established Ziegler, Biersack and Littmark (ZBL) potential at 0.95 Å.

Simulation cells containing 80x80x80 unit cells (409,600 atoms) were used for 10 keV primary knock-on atom (PKA) kinetic energy cascades and 120x120x120 unit cells (13,824,000 atoms) for 50 keV PKA cascades. The initial system was equilibrated for 2 picoseconds with time steps of 0.1 femtosecond. Each cascade was initiated by giving a Si atom the kinetic energy of 10 or 50 keV while holding zero total momentum. The cascades evolved for 20 ps and the time step is modified such that the distance traveled by the fastest particle in the system is less than 0.014 Å. Constant volume is held through the iteration and the lattice parameter is chosen for zero system pressure in equilibrium at a particular temperature. The Wigner-Seitz cell analysis method was used to determine defects in the modeling system.

The *ab initio* recombination barrier within the density functional theory (DFT) was calculated using the Quantum ESPRESSO (QE) package [4]. The calculations have been done a using plane-wave basis set and ultrasoft pseudo-potential [5] optimized in RRKJ scheme [6] (Si.pbe-n-rrkjus.UPF, C.pbe-n-rrkjus.UPF from QE pseudopotentials database). We used the Perdew, Burke, and Ernzerhof [7] exchange-correlation functional. The Brillouin zone (BZ) summations were carried out over a 4x4x4 BZ grid for the system with 64 atoms in the supercell. The electronic smearing with a width of 0.02 Ry was applied according to the Methfessel-Paxton

method. The plane wave energy cut off 40 Ry and charge density -400 Ry allows reaching an accuracy of 0.2 mRy/atom. Atomic structure was optimized until the forces were smaller than 0.001 Ry/Å.

The 10 keV cascade simulations with Tersoff potential were carried out for a range of temperatures and indicated that in-cascade recombination in SiC seemed to be much lower than in metals. Thus, for example, the ratio of the peak defect count to the stable defect count at t>10 ps is less than a factor of two in SiC and almost two orders of magnitude in iron. Such significant difference between SiC and Fe results is caused by the presence of "empty" spaces in the SiC lattice in (1/2, 1/2, 1/2), (3/4, 3/4, 3/4) and symmetry related positions which easily accommodate interstitial atoms.

Point defects in SiC consist of interstitials (I) and vacancies (V) of both carbon and silicon, as well as antisite defects of C on a Si site (C_{Si}) and Si on a C site (Si_C). The carbon defects predominate as shown by the green and purple symbols in Figure 72.

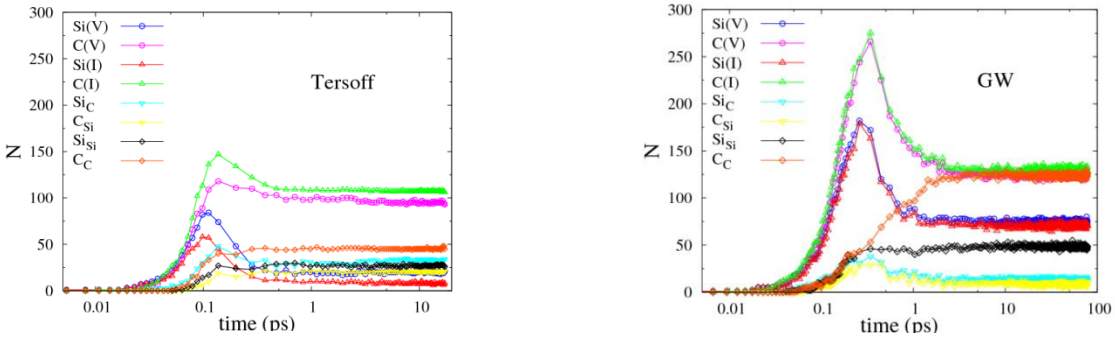

Figure 72. Time dependence of the number of point defects observed in MD displacement cascade simulations at 10 keV pka at 300 K: (a) Tersoff potential, (b) GW potential.

This result is qualitatively similar to that obtained with Tersoff potential (Figure 72b). However, in contrast to the simulations with the Tersoff potential, the GW potential (Figure 72b) produces almost twice as many C vacancies and interstitials at the time of maximum disorder (~0.2 ps) but only about 25% more stable defects at the end of the simulation. As a result the ratio of peak-to-stable defects is much higher for the GW potential. This result is more similar to that observed in metals and oxides. Only about 20% of the carbon defects produced with the Tersoff potential recombine during the in-cascade annealing phase, while about 50% recombine with the GW potential.

As discussed in our earlier reports, the energy barrier for carbon V-I recombination with the GW potential is much smaller than with the Tersoff potential barrier, and is closer to result of first-principles calculation (Figure 72). On the basis of these result we can conclude that GW potential gives a much more realistic description of cascade dynamics in SiC and we will use this potential in our continuing work.

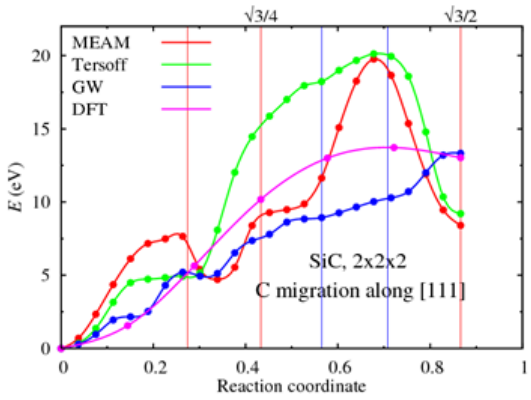

Figure 73. Carbon atom migration barrier in [111] direction.

The results for cluster size distribution at the end of simulation for both potential are presented in Figure 74. In our analysis we defined groups of point defects as a linked cluster if any of them are connected by a distance less than the lattice parameter. Both simulations produce a significant amount of pair clusters and ~ 75 % of these clusters correspond to the same atom type I-V pair. However if in the case of Tersoff potential all I-V pair clusters correspond to carbon atoms, in the case of GW potential a significant part of these clusters corresponds to silicon atoms.

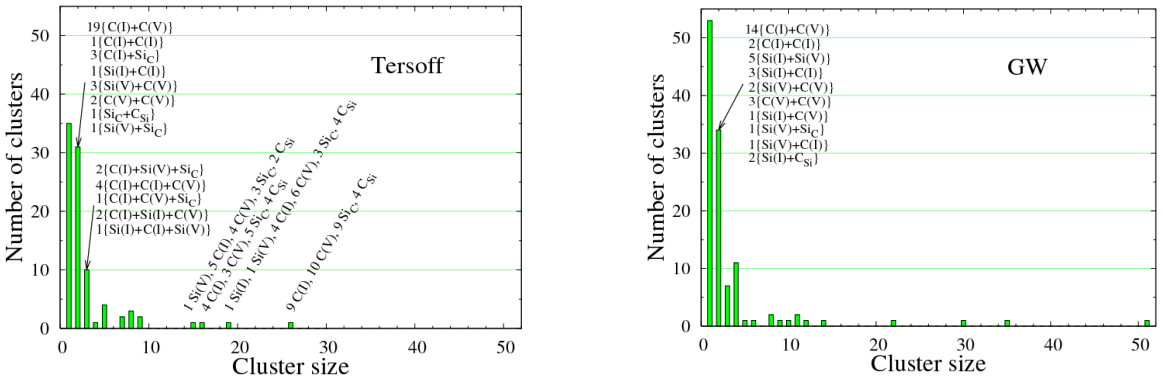

Figure 74. Cluster size distribution at the end of 10 keV Si recoil event in SiC at 300 K: (a) Tersoff potential, (b) GW potential.

Another difference is found for the large size cluster distributions. Thus in the case of Tersoff potential (Figure 74a) there are only two relatively large clusters containing 19 and 21 defects; in the case of GW potential there are four clusters of size 21, 30, 35 and 51 defects. These large size clusters could be discussed as potential candidates for amorphisation region formation.

The number of defects at the end of cascade evolution is weakly temperature dependent for Tersoff potential, but reduces with temperature for the GW potential (Figure 75). The difference is due to artificially large migration barriers for the Tersoff potential. The increase in the temperature naturally leads to more diffusion of carbon vacancies and interstitials. As a result, more carbon vacancies and interstitials recombine and the number of defects at the end of cascade evolution is reduced as the temperature increases. In contrast, the defect migration barriers for Tersoff potential are so large that diffusion is suppressed, even at temperatures as high as 1600 K and the number of defects is only weakly temperature dependent.

Additional computational resources have been used in this work through collaboration with JAEA.

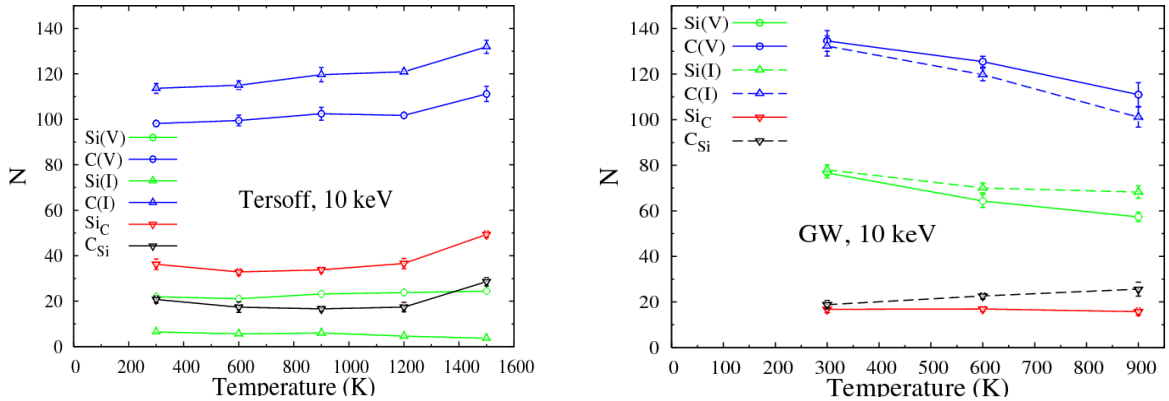

Figure 75. The number of defects at the end of cascade evolution.

FUTURE PLANS

In the coming year, we are planning to do a series of 50 keV cascade modeling with Tersoff potential at elevated temperature, will finish the analysis, and will publish the results.

REFERENCES

6. J. Tersoff, Phys. Rev. B 39 (1989) 5566–5568 .
7. F. Gao and W. J. Weber, Nucl. Instr. And Methods in Phys. Research B 191 (2002) 504-508.
8. S. Plimpton, Fast Parallel Algorithms for Short-Range Molecular Dynamics, J Comp Phys, 117, 1-19 (1995).
9. P. Giannozzi, S. Baroni, and N. Bonini ... Quantum espresso: a modular and open-source software project for quantum simulations of materials. J of Physics:Condensed *Matter*, 21, 395502 (2009).
10. D. Vanderbilt. Soft self-consistent pseudopotentials in a generalized eigenvalue formalism. Phys. Rev. B, 41, 7892–7895, (1990).
11. A. M. Rappe, K. M. Rabe, E. Kaxiras, and J. D. Joannopoulos. Optimized pseudopotentials. Phys. Rev. B, 41, 1227–1230, (1990).
12. J. P. Perdew, K. Burke, and M. Ernzerhof. Generalized gradient approximation made simple. Phys. Rev. Lett., 77,3865–3868,(1996).

9.0 INTERNATIONAL COLLABORATIONS

9.1 US-JAPAN COLLABORATION ON RAFM STEEL

Y. Katoh (katohy@ornl.gov), M. Ando (JAEA)

OBJECTIVE

This collaboration between DOE and JAEA jointly pursues activities using the advanced capabilities for materials irradiation and post-irradiated examination using HFIR. The focus is on ferritic steels and other advanced materials, especially the development of the material database for facilities beyond ITER. The targets include achieving DEMO-relevant performance data on reduced activation ferritic/martensitic steels (RAFS) neutron irradiated in HFIR to high levels of displacement damage (>30 dpa).

SUMMARY

The DOE-JAEA collaboration continues to make steady progress in building the materials data base for the RAFM F82H steel, with irradiations to displacement damage levels of 80 dpa now accomplished. The goal of this project is to accumulate the principal irradiation property data for F82H, contributing to the materials data base for the blanket structural design of a fusion DEMO reactor.

PROGRESS AND STATUS

The DOE-JAEA Project is the US-Japan long-running collaboration now in its 31st year. The objective of this project is to perform irradiation and post-irradiation examination (PIE) of first wall and blanket structural materials for fusion reactor. Irradiation experiments for exposures up to 20 dpa were started for the reduced activation ferritic/martensitic (RAFM) steel and several BCC alloys in the HFIR Phase 3 program (1995-2000). In the Phase 4-5 programs (2000-2009), three main tasks were planned. (1) To improve the irradiation resistance of RAFM, especially the fracture toughness, (2) To obtain data for high-dose irradiated RAFM and ODS steels up to 80 dpa, and (3) To examine the effect of helium on mechanical properties and microstructures using boron and/or nickel-doped RAFM and Ni/Al coating techniques. Four target capsules (JP26, 27, 28 and 29), one RB capsule (RB15J) and several rabbits were irradiated in these Phases. Primary PIE for JP26 and JP27 capsules is almost complete. For RB15J capsule, some PIE remains. Irradiation of the high-dose JP28&29 capsules was completed in 2013. In the Phase 6 (2009-2014) program two additional target capsules (JP30&31) were built to obtain the irradiation effects on joined sections of RAFM (TIG weldments, EB weldments and HIP joints). Several high-dose rabbit capsules (containing RAFM and SiC/SiC composites) were also irradiated. These irradiation experiments were also completed in 2013. Figure 76 shows the current status of data obtained and the planned PIE for irradiated F82H base metal and several weldments (including results from irradiations in the FFTF/MOTA program and in Japanese research reactors).

The PIE of material from the high-dose target capsules (JP28&29) started in 2014, and the irradiation of several rabbit capsules is ongoing.

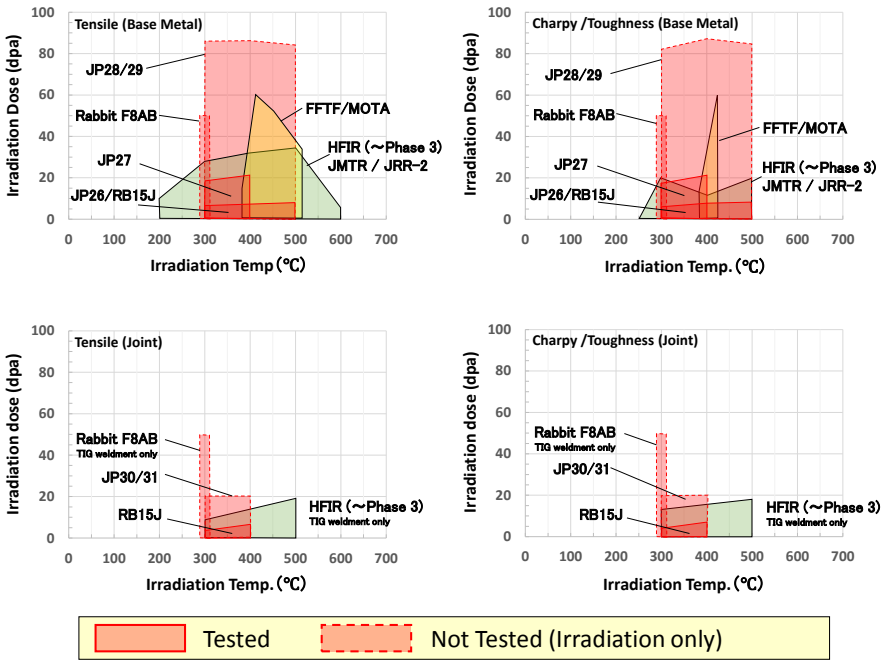

Figure 76. Status of accumulated data for F82H-IEA irradiated in several fission reactors

FUTURE PLANS

The PIE on specimens from some target capsules (JP28, 29, 30 and 31), rabbit capsules (F8AB and F11AB) from phase4-6 programs will continue in FY2015. Also, a new HFIR RB capsule for the post-phase 6 program will be prepared in a shared activity with other collaboration programs.

9.2 US-JAPAN PHENIX COLLABORATION

Y. Katoh, A.S. Sabau, T.S. Byun, L.M. Garrison, X. Hu, L.L. Snead, and Y. Ueda (Osaka University)

OBJECTIVE

The PHENIX Project on Technological Assessment of Plasma Facing Components for DEMO Reactors is the current US/Japan Fusion Research Collaboration Project that started in April 2013. The goal of the project is to evaluate the following critical issues on plasma-facing components (PFCs) under divertor conditions of fusion reactors: (1) heat transfer, (2) mechanical properties, (3) neutron irradiation effects, and (4) tritium retention and permeation. The project participants are ORNL, Idaho National Laboratory, Sandia National Laboratory, Georgia Institute of Technology, National Institute for Fusion Science of Japan, and various Japanese universities . The roles of ORNL are to participate in Task 1 on high heat flux testing, Task 2 on neutron irradiation effects, and provide neutron irradiation in HFIR in support of all research tasks.

SUMMARY

In FY14, six tungsten specimens were successfully tested at ITER-relevant high-heat flux conditions using the ORNL Plasma Arc Lamp facility. Other efforts in this reporting period were focused on: (1) reducing the oxidation of the sample during high-heat flux testing, (2) enhancing the measurement accuracy of sample temperatures during HHF testing, and (3) setup the model for the thermo-mechanical simulation of the high-heat flux testing. For thin specimens that are often used for studies of neutron irradiation effects, one of the main challenges to the PAL systems is the measurement of the sample temperature.

Specimens of tungsten materials that had been irradiated to low dose levels in HFIR were tested for tensile properties, microhardness, and microstructures. In addition, the effects of thermal annealing in neutron irradiated tungsten were examined by microhardness and positron annihilation spectroscopy. In preparation for the new irradiation campaigns, a set of rabbit capsules were constructed for irradiation in HFIR in FY-15 and design work for a new large HFIR-RB* capsule was initiated.

PROGRESS AND STATUS

PHENIX Task 1. High heat flux testing of W-based specimens

The evaluation of several fixtures for specimen clamping continued during the visit of Dr. Kazutoshi Tokunaga of Kyushu University. Six samples, which were supplied by the Japanese collaborators in the PHENIX program, were exposed to high-heat fluxes at ORNL. Each sample was exposed to heat fluxes that would limit the sample temperatures to the allowable maximum temperatures for each sample type.

During a project update presented at the PHENIX Task 1 Workshop, held at the Uji Campus of Kyoto University, Japan on June 5-6, 2014, several recommendations were made, including:

(1) Conduct HHFT at high-vacuum to reduce/eliminate specimen oxidation,
(2) Conduct HHFT at higher thermal gradients through the W/F82H specimen, and
(3) Conduct HHFT at higher heat fluxes.

PHENIX Task 2. Effects of neutron irradiation

Miniature tensile (Type SS-J) and miniature coupon specimens of tungsten, primary monocrystalline materials, were tensile tested following neutron irradiation in HFIR up to ~0.1 dpa at the coolant temperature and nominally at 300, 500, and 650°C. Testing at room temperature indicated the

completely brittle fracture behavior of all the irradiated materials. Testing at the temperatures of irradiation is currently in progress. Transmission electron microscopy examinations have revealed the microstructural development in these materials during irradiation.

An additional experiment was initiated to determine the defect annealing processes in neutron-irradiated tungsten as a function of temperature, using microhardness measurements and positron annihilation spectroscopy for characterization. The initial experiment demonstrated that the positron technique provides useful information on vacancies and their clusters. This works will continue into FY-15. PHENIX assignees Mr. Makoto Fukuda and Prof. Kiyohiro Yabuuchi collaborated on these experiments. .

Additional irradiation vehicles are needed for this collaboration. A set of six rabbit capsules is planned to achieve the relatively low dose irradiation within the first half of the project performance period. Each of these rabbit capsules will accommodate a few dozens circular disc specimens that may be utilized for thermal conductivity measurement, equibiaxial flexural testing, positron annihilation spectroscopy, hydrogen isotope retention and permeation studies, hardness determination, high heat flux testing with the PAL, and microstructural examination. This campaign achieved substantial progress with the engineering design complete and approved and most specimens machined and inspected.

In addition to the rabbit capsules, a full-length capsule for insertion in the HFIR RB* facility is planned. This capsule, tentatively designated RB-19J Experiment, will accommodate a large number of specimens in multiple separate temperature zones, each of which is actively temperature controlled. Most importantly, the large diameter of the RB* capsules allows use of the thermal neutron shielding material surrounding the internals, to minimize undesirable nuclear transmutation of tungsten during irradiation. In FY-14 the design work completed selection of shielding material and achieved major progress in conceptual design of the capsule toward the target insertion in HFIR in early 2016.

FUTURE PLANS

All technical tasks will continue through FY-19. ORNL will contribute to the project by providing project management, participating in personnel exchanges and workshops, and publishing and presenting the results, in addition to the continuing research in the areas described for FY-14.

9.3 ORNL-KIT COLLABORATION

Lance L. Snead (sneadll@ornl.gov), Yutai Katoh, Lauren Garrison, Michael Rieth (KIT)

OBJECTIVE

This recently established collaboration with the Karlsruhe Institute of Technology in Germany is directed at evaluating the effects of irradiation on tungsten materials, as part of the larger effort to develop a material suitable for use in high heat flux components of divertors in fusion service. HFIR is the irradiation source for this research using materials provided by both parties.

PROGRESS AND STATUS

Tungsten is currently the primary candidate plasma facing material for fusion and the only PFM considered for ITER. However, in bridging from ITER to DEMO it is recognized that issues specific to tungsten: difficulty in fabrication, low temperature and irradiation embrittlement, and high-temperature recrystallization, are without current solutions. For this reason efforts are underway at KIT to design advanced helium cooled divertor modules and at ORNL on advanced tungsten-based materials as well as to understand the irradiation-induced property changes. As these programs have natural synergies a no-funds-transferred collaboration began in 2013 for the development of tungsten-based PFC's.

As part of their contribution to the collaboration KIT has provided and continues to develop advanced tungsten composite materials based on their work with tungsten-copper laminates. ORNL, while developing their own advanced refractory alloys, is contributing irradiation and post-irradiation examination to this collaborative effort. A series of rabbit capsules were constructed and irradiated in the flux-trap of HFIR and irradiated in the temperature range of 80 to 760°C in a fluence range of 0.02 to $20x10^{25}$ n/m^2 (E>0.1 MeV). Samples included single crystal tungsten with [110] and [100] orientations as well as the Cu-W laminate. The capsules completed irradiation in 2014 and significant PIE has been carried out including hardness measurement, tensile testing, SEM, and TEM. A plot mapping the microstructure as a function of dose and temperature is provided in Figure 77.

FUTURE PLANS

Over the next year the collaboration will extend the HFIR irradiations to include new materials developed by both ORNL and KIT. A new series of irradiations will include more relevant fusion temperatures, specifically 800-1200°C.

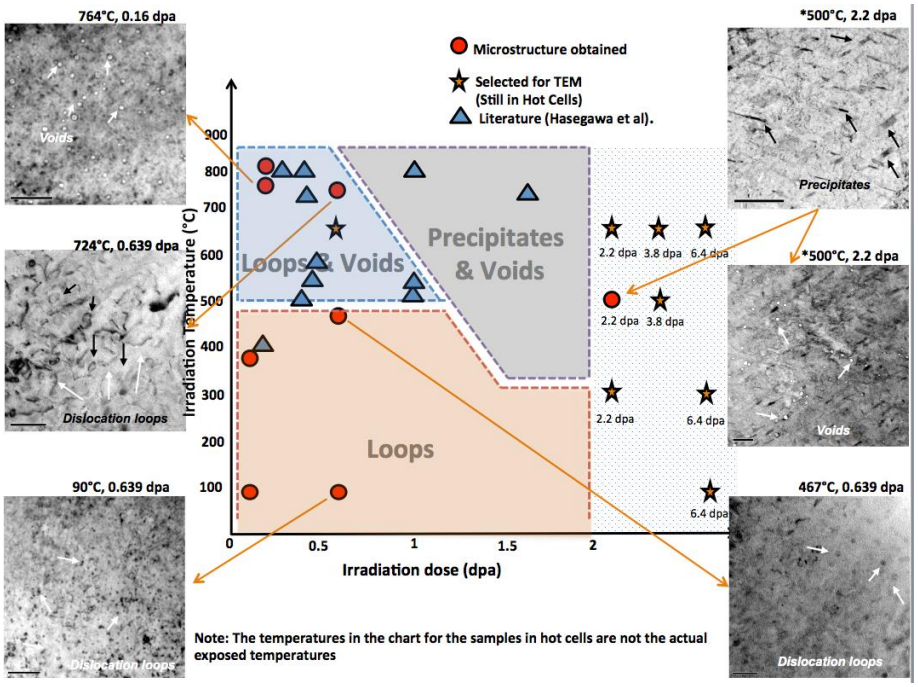

Figure 77. Map of microstructural features in tungsten produced by neutron irradiation at several temperatures.

10.0 MATERIALS ENGINEERING SUPPORTING THE FNSF STUDY

A.F. Rowcliffe (art.rowcliffe@gmail.com)

OBJECTIVE

The primary objective of this task is to define a framework which will enable the development of a credible roadmap for the development and performance validation of power plant-relevant materials for the FNSF in terms of radiation-damage tolerance, reduced activation characteristics, operating temperature range, chemical compatibility, plasma-facing performance, and component-specific fabrication methods.

SUMMARY

Information on materials processing, mechanical behavior, radiation effects, and coolant compatibility issues is being provided to assist in the process of identifying potential solutions to the definition of materials for power core components (FW/blanket, divertor), tritium extraction systems and for lifetime structural components such as the vacuum vessel, structural ring and neutron shields. At the same time, feedback is being provided to the fusion materials program regarding component-specific issues such as proposed operating temperature ranges, temperature and neutron flux gradients, coolant temperatures and transmutation generation rates for helium and hydrogen.

PROGRESS AND STATUS

During this year input has been provided on materials properties and performance in a wide range of technical areas as follows;

a) The critical importance of a 14 MeV-peaked neutron source such as IFMIF in confirming understanding of mechanisms of radiation damage-induced property degradation in the fusion environment and establishing a materials engineering database to support the design and licensing of FNSF/DEMO systems; the pivotal role of neutron sources in the evolution of an FNSF roadmap,

b) FW/blanket and divertor materials issues in water-cooled designs; development of materials performance-based arguments to support a rationale for elimination of water cooling for FNSF, based on low temperature embrittlement of RAFMs and the inadequate performance of current copper heat sink materials,

c) Characteristics of a Materials Testing Module in an FNSF for materials performance surveillance and for fusion neutron testing of advanced materials,

d) Establishment of credible neutron dose limits for structural alloys based on liquid metal breeder reactor experience with component irradiations to doses >100 dpa,

e) Role of current Generation 1 RAFMs, Generation II RAFMs and ODS (NS) structural materials in the development of long-range blanket testing strategies,

f) Refractory metal performance issues in a high temperature tritium permeator extraction system,

g) Joining and fabrication issues with RAFM-based FW/blanket concepts, and the possibilities of utilizing additive manufacturing and other technologies, with the goal of reducing the number of welded and bonded joints in the blanket structure, and

h) Key feasibility issues related to the performance of SiC/SiC composites which must be resolved before extended performance as flow channel inserts in DCLL blankets can be predicted with sufficient confidence.

FUTURE PLANS

This activity will continue to advise on materials issues and promote the ongoing interaction between the FNSF project and the fusion materials program. A main goal is to define a framework for a detailed roadmap that addresses the critical issues associated with developing materials engineering solutions for all fusion core and out-of-core components and systems.

11.0 IRRADIATION PROGRAM

11.1 HFIR IRRADIATION EXPERIMENTS

Y. Katoh (katohy@ornl.gov), J.L. McDuffee, C. Bryan

SUMMARY

Neutron irradiation experiments were performed in support of the research and development of fusion reactor materials using various materials irradiation facilities in the High Flux Isotope Reactor (HFIR). *During FY-2014, 16 target zone rabbit capsules completed HFIR irradiation, achieving the target neutron fluences. Those capsules are listed in*

Table 9 along with condensed information on material, specimen type, and temperature, fluence, and period of irradiation. At the end of FY-2014, 13 target zone rabbit capsules are continuing irradiation in HFIR toward their target neutron fluences. Those capsules are listed in Table 10 along with the information on materials, specimen types, and temperatures, fluences, and periods of irradiation.

Note that HFIR operated for six cycles in FY 2014, included cycles 450 to 455.P

Table 9. Fusion materials program capsules that completed HFIR irradiation in FY-2014. Note that all capsules are target zone rabbit capsules.

Experiment Designation	Primary Materials	Specimen Types*	Irradiation Temperature (°C)	Max Exposure (dpa)	Number of Reactor Cycles	HFIR Cycles From – To		
T9G-13	Steels, W	SSJ, MC	300	10	9	443	–	451
T9C-24	Steels, W	SSJ, MC	650	10	8	443	–	450
PC5X	Various	SSJ, MC	80/100	16	9	442	–	450
TB-650-4	Steels, W	SSJ, MC	650	16	11	443	–	453
JCR11-09	SiC/SiC	Mini-comp.	950	4	3	448	–	450
JCR11-10	SiC/SiC	Mini-comp.	950	10	8	448	–	455
MAX-02	MAX, etc.	Various	400	6	4	449	–	452
MAX-03	MAX, etc.	Various	400	10	6	449	–	454
MAX-05	MAX, etc.	Various	700	6	3	449	–	451
MAX-06	MAX, etc.	Various	700	10	5	449	–	453
MAX-08	MAX, etc.	Various	1000	6	3	449	–	451
MAX-09	MAX, etc.	Various	1000	10	5	449	–	453
SCJ2-10	SiC Joint	Torsion	500	3	2	453	–	454
SCJ2-12	SiC Joint	Torsion	500	3	2	453	–	454
SCJ2-16	SiC Joint	Torsion	1000	3	2	454	–	455
SCJ2-17	SiC Joint	Torsion	1000	3	2	454	–	455

*T/SSJ = Tensile, MC = Multipurpose Coupon, Mini-comp. = single tow composite, Torsion = torsional hourglass joint. Some experiments also contain TEM disks, other special purpose specimens, and monitors occupying small spaces.

Table 10. HFIR fusion materials program rabbit capsules that are continuing irradiation beyond FY-2014.

Experiment Designation	Primary Materials	Specimen Types*	Irradiation Temperature (°C)	Max Exposure (dpa)	Number of Reactor Cycles	HFIR Cycles From – To
F13A5	F82H	SSJ	300	15	9	451 – 459
F13A6	F82H	SSJ	300	30	18	451 – 468
F13B4	F82H	SSJ	300	15	9	451 – 459
F13B5	F82H	SSJ	300	30	18	451 – 468
JCR11-01	SiC/SiC	BB	950	50	25	445 – 469
JCR11-03	SiC/SiC	BB	950	30	15	447 – 461
JCR11-04	SiC/SiC	BB	950	30	15	447 – 461
JCR11-05	SiC/SiC	BB	950	50	24	444 – 467
JCR11-07	SiC/SiC	BB	950	100	50	444 – 493
JCR11-08	SiC/SiC	BB	950	100	50	444 – 493
JCR11-11	SiC/SiC	Mini-comp.	950	30	14	448 – 461
JCR11-12	SiC/SiC	Mini-comp.	950	100	24	448 – 481
SCJ2-11	SiC Joint	Torsion	500	20	10	453 – 462

*T/SSJ = TensileBB = Bend Bar, Mini-comp. = Single Tow Composite, Torsion = torsional hourglass joint. Some experiments also contain TEM disks, other special purpose specimens, and monitors occupying small spaces.

11.2 AN ADVANCED MATERIALS IRRADIATION FACILITY FOR MATERIALS RESEARCH IN HFIR

N.O. Cetiner (cetinerno@ornl.gov), G.L. Yoder, J.L. McDuffee, Y.S. Kwon, L.L. Snead, and C. Bryan

OBJECTIVE

This ORNL-LDRD funded project will design and prototype a state-of-the-art Materials Irradiation Facility (MIF) that can be implemented at the High-Flux Isotope Reactor (HFIR). The MIF will provide a modern, flexible instrumented capability to monitor and control experiments during irradiation. Incorporation of this facility into HFIR will significantly enhance the HFIR capability to develop and assess the performance of advanced materials and fuels in an irradiation environment.

SUMMARY

The design of a new MIF will reinvigorate the use of instrumented experiments and provide a platform to apply advanced measurement and irradiation techniques. The two-year research plan is divided into the following two major tasks: (1) develop a proven, modern, modular design for instrumented materials irradiations, and (2) prototype selected hardware and test design feasibility.

PROGRESS AND STATUS

In FY14 the design team developed a conceptual design that meets the identified customer and operational requirements. The equipment needed to develop the new design has been identified and purchased. In the new MIF concept; there are two human machine interface (HMI) touch screens for both controlling and monitoring irradiation experiments. These are installed in new cabinets that will be included in the MIF footprint. The HMIs located in the MIF will communicate directly with the programmable logic controller (PLC) via a data link. The HMI's display mimics the inert gas supply headers, sensors and control components, experiment vacuum pumps, effluent valve status, and radiation levels to the HFIR effluent gas system. Pop-up controls for the control components will be provided. HMIs will also display sample temperatures, capsule gas pressures, moisture levels, oxygen levels, dry wall junction box pressure, reactor power, and ambient temperature. The MIF software is designed to provide appropriate annunciations for the operator. The alarm panel with an annunciator screen will be available on the new control system. The system has oxygen, moisture, radiation, and pressure sensors that produce input signals to the PLC. An audible annunciator alarm horn is also provided to alert the operator of an alarm condition. The HFIR main control room will be supplied with selected alarm indicators. The HMI also has system diagnostic capabilities to help operators identify problem sources. The gas supply system is designed to supply inert gases to experiments and provides the control of temperature, flow rate and pressure. The typical gases used in past experiments are helium, neon and argon. This new design has introduced the flexibility to use other gases such as a deuterium/helium mixture that is compatible with the system by re-calibrating the appropriate flow transmitting control valves. The MIF also monitors the effluent stream from experiments to the HFIR off-gas systems. The MIF will be used to monitor the effluent lines for moisture, pressure, and flow rate to detect leaks and assist with flow control. The new flexible design of the MIF system allows advanced measurement equipment to be easily incorporated as future research dictates. In FY14 the team also worked on developing the design for the software re-configurable, flexible gas routing module that provides distribution of feed gas streams specific to the requirements of instrumented experiments. This unique modular system is a flexible configuration that will eliminate the requirement for building individual control and piping cabinets for each experiment. The gas lines and the thermocouple leads for each experiment can be easily connected to the newly designed gas routing module. The module serves as an

interface between the MIF common systems and the irradiation experiments. The MIF common systems deliver oxygen- and moisture-free inert gases to the gas routing module. This module distributes the gases into the experiment based on the irradiation design requirements. This system is flexible and reconfigurable to support the needs of future experiments and is designed to be duplicated, easily allowing simultaneous experiments to be operated. The gas routing system will be controlled by a separate Allen Bradley PLC. The MIF gas routing PLC will be configured as a networked slave unit to the main MIF Common PLC. The gas routing HMI will be configured to perform all the functions necessary for system configuration, set-up and testing. Gas routing system configuration and operation can be performed either locally with the gas routing HMI or remotely with the MIF common HMI.

Previously, the temperature control for instrumented experiments was accomplished by varying the flow rates of helium, neon, and/or argon for each of the temperature zones. Because gas introduced into the lower zone of the experiment flows through the upper zones, adjustment of gas flow to one zone requires adjustment to other zones as well. To simplify the operation of experiments, algorithms are being designed to allow the operator to set the gas concentrations for each zone independently, taking into account the interdependence of the gas concentrations between zones and the flow rate limitations. This will transfer the computational burden from the operator to the PLC and reduce the likelihood of errors and simplify operation when adjusting temperatures.

Design and functional requirements documents for the MIF Common systems have been completed. Based on these requirements, the team initiated development of flow and logic diagrams. Mechanical drawings and control software for the MIF Common Systems have been developed. A Quality Assurance Plan (SQAP), software verification and validation (V&V) plan, backup and recovery plan (BRP), and cyber security plan have also been prepared to ensure compliance with SBMS and ORNL IT requirements.

FUTURE PLANS

The FY15 goal is to complete and validate the design feasibility of the MIF modules. The subtasks will be to develop the gas routing system control software and test the software. The team is planning to initiate coupling of control system and the gas routing control hardware, develop a design for a gamma spectrometry system and adapt the design for the shielding and the safety requirements.

11.3 CONCEPTUAL DESIGN FOR A NEW INSTRUMENTED HFIR CAPSULE

J. L. McDuffee (mcduffeej@ornl.gov) and D. W. Heatherly

OBJECTIVE

The objective of this task is the conceptual design for a new Fusion materials temperature-controlled capsule to be irradiated in one of the RB* positions of the High Flux Isotope Reactor. The capsule will be designated MFE-RB-19J, with a possible companion capsule MFE-RB-20J. The zone temperatures have not been finalized, but will likely be in the range from 300 to 1200°C. Specimens will be primarily 3, 6, and 10 mm disks, along with some tensile specimens. The capsule is to have the option of flowing deuterium over the specimens.

PROGRESS AND STATUS

BASIC DESIGN

The conceptual design of the capsule in the specimen region is shown in Figure 78. The outer two layers represent the existing HFIR RB* liner and the water-filled cooling gap. Inside the water gap, the primary containment consists of a 316 stainless steel tube. Inside the steel containment, there is a thermal neutron shield (described in more detail later) that is pressed against the containment with an inner steel cylinder. The primary temperature control gap is between this inner steel cylinder and the specimen holder. The specimen holder is slotted in various ways to accommodate specimens. The specific cut design shown in Figure 78 is arbitrary and will be modified for the specific capsule specimen loading as the specimen loading is developed.

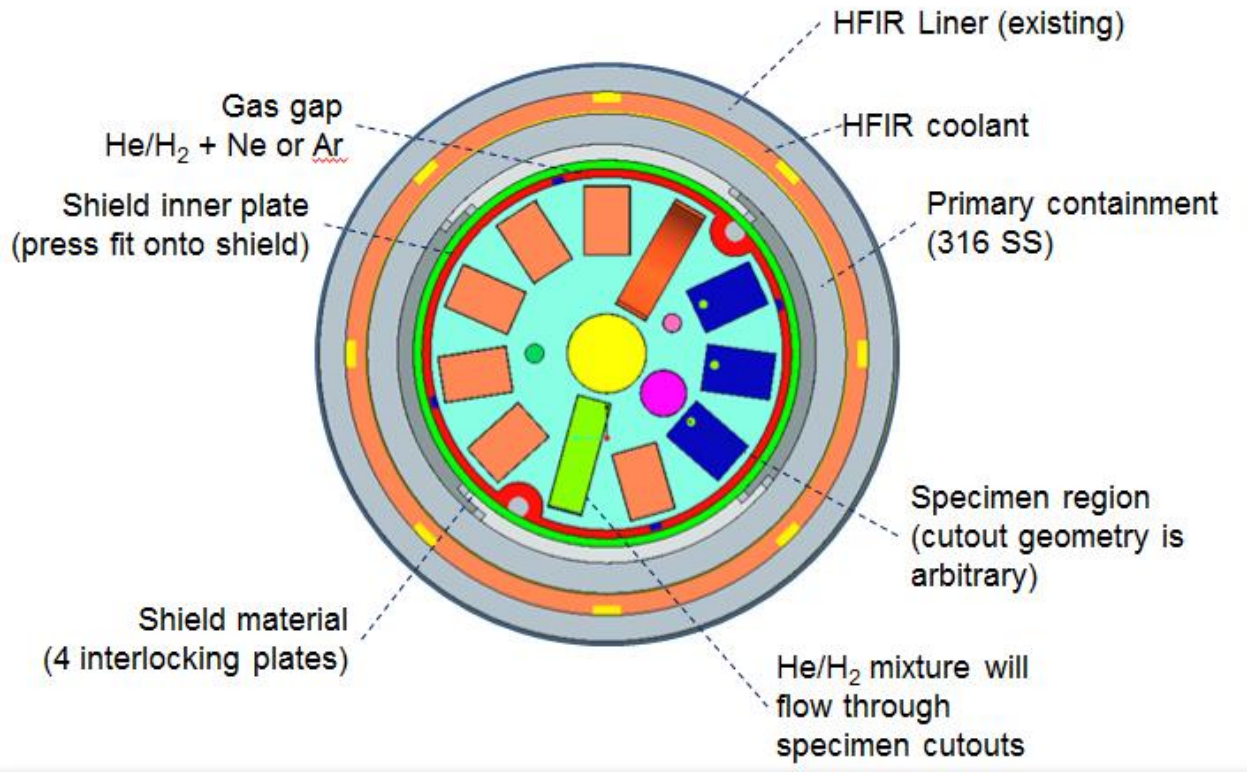

Figure 78. Cross-section of the Conceptual Design

One of the design requirements for this capsule is that the specimens can be exposed to deuterium gas during irradiation. However, it would be costly and difficult to maintain a flammable gas in close proximity to the reactor during operation. The flammability chart for Hydrogen/Helium in air is shown in Figure 79. For this design, a pre-mixed gas will be purchased that is 8.5% deuterium in helium. This will allow deuterium to be delivered to the specimens while also keeping the gas below the lower flammability limit.

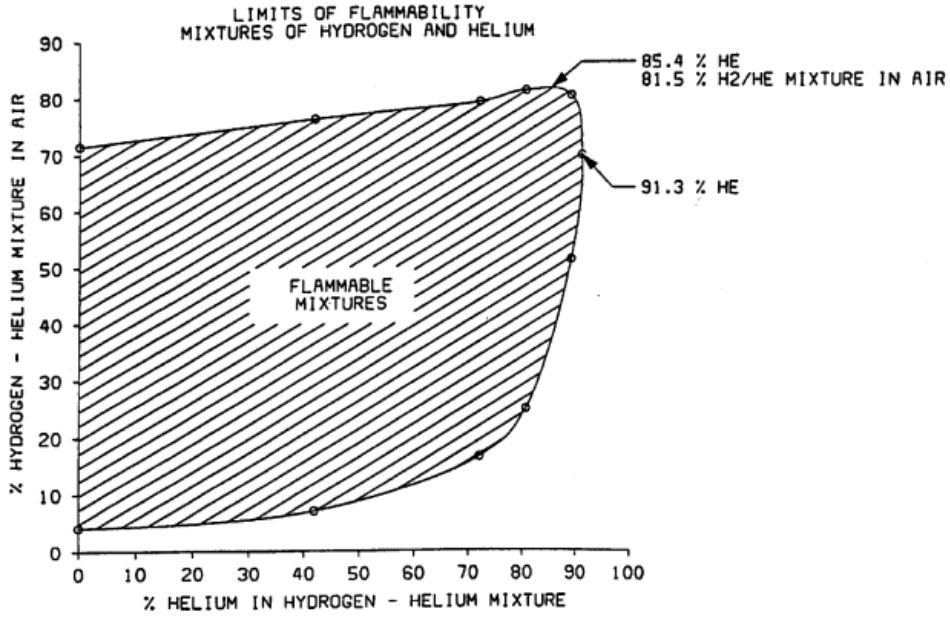

Figure 79. Flammability of Helium-Hydrogen Mixtures

As shown in Figure 80 the He/H_2 mixture is delivered to the top of the in-pile section and is directed through each specimen region to the bottom of the capsule. The spacers between sections are not tightly sealed, but they are sealed well enough to keep most of the He/H_2 gas mixture flowing downward.

The specimen temperature inside the capsule is controlled by a combination of gas gap size (determined by calculation prior to fabrication) and fill gas concentration (for real-time adjustments). At the bottom of the capsule, the He/H_2 gas mixture turns 180°, mixes with a control gas (i.e., neon or argon), and moves upward through the primary gas gap. Additional control gases are introduced in the spacer regions between each subcapsule. Three separate temperature zones are shown in Figure 80, although the actual number of zones has not been decided. Figure 81 shows the current conceptual design with three subcapsules as it is currently represented in the drawing package.

SHIELD DEVELOPMENT

In previous RB* experiments, the thermal neutron shield material was Eu_2O_3, and it was located inside the outer liner and outside the water coolant gap. However, Eu_2O_3 is very difficult to fabricate. Previous work on these shields only achieved a <50% success rate, and the fabrication techniques and expertise from that last capsule build of this type are no longer available.

Figure 82 shows the results of a scoping study performed to compare other possible shield options. The top row shows the neutron flux in a design similar to that used previously with a water gap between the shield and the specimen region. The second row shows the neutron flux when the shield is moved inside

the water gap. There is a clear advantage to moving the shield inside the coolant gap as the gap re-thermalizes the neutrons as they pass through the water.

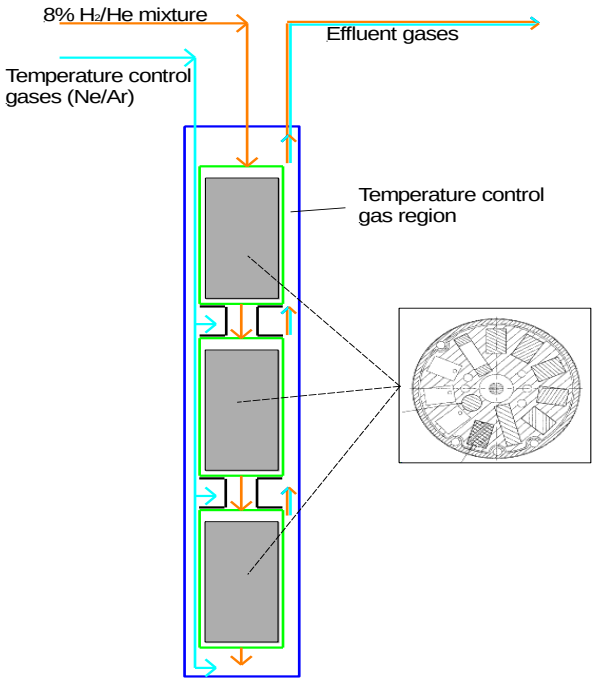

Figure 80. Gas Flow Diagram of the Capsule

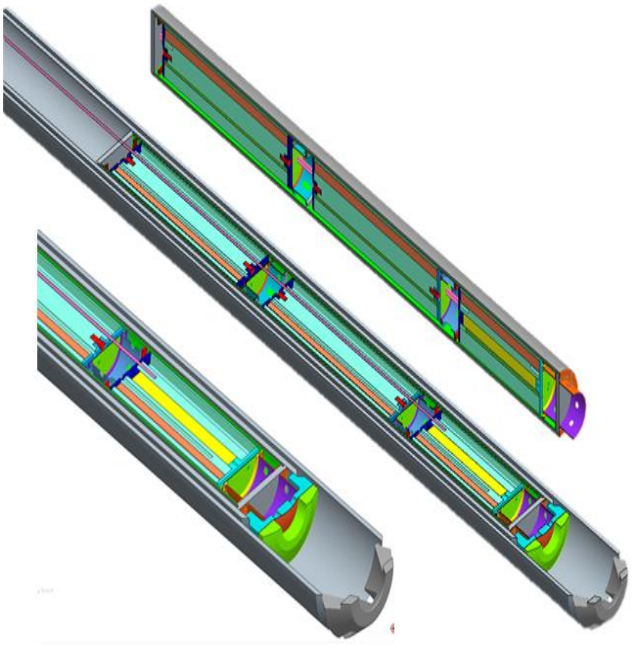

Figure 81. Overall Capsule Design

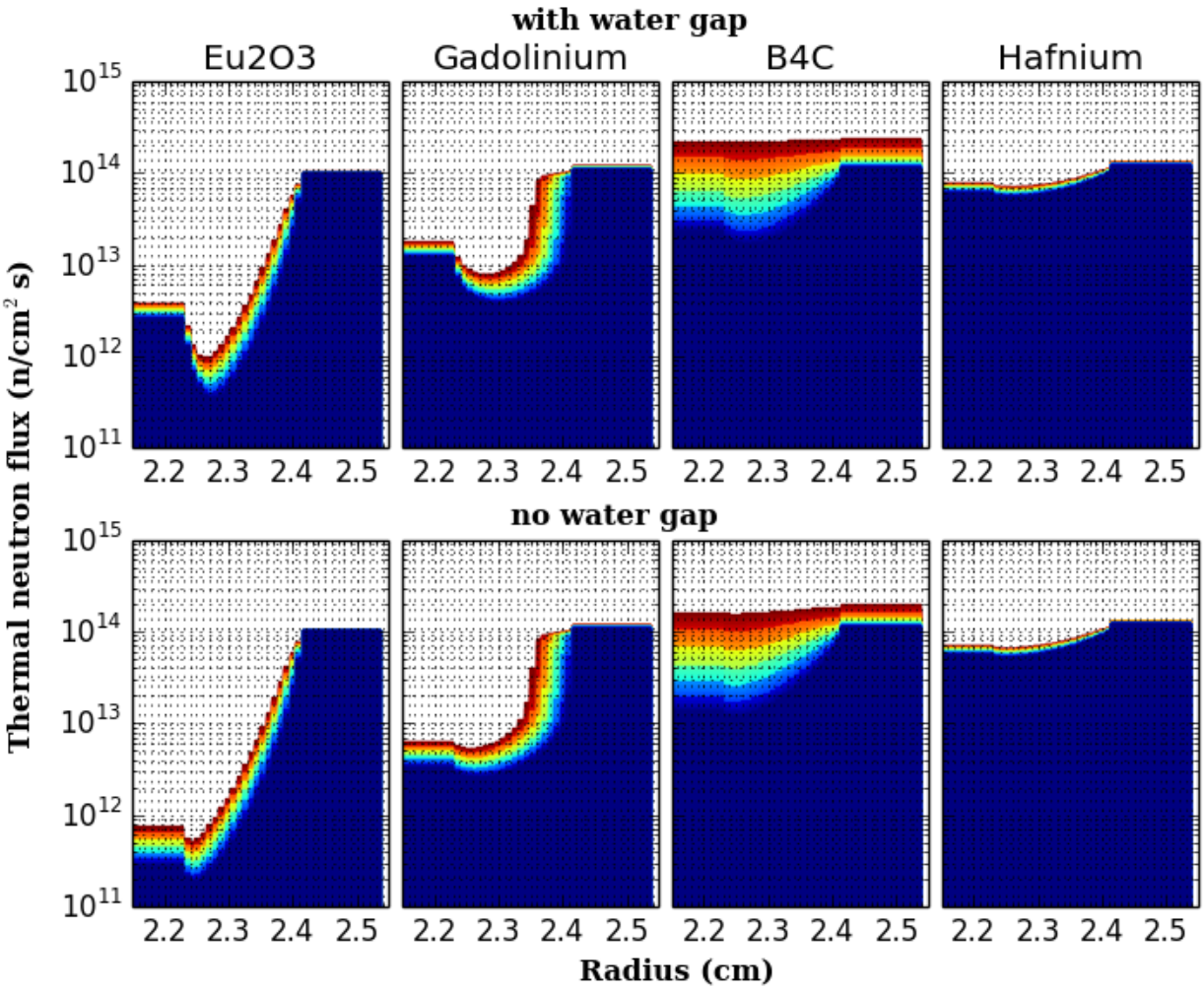

Figure 82. Comparison of Various Materials with and without an Internal Water Gap

Figure 82 also shows the relative effectiveness of four different shield materials. The blue color represents the neutron flux at the beginning of life with the specimen region at the far left. The red color represents the neutron flux at the end of six cycles, or approximately one calendar year of operation. The progression from blue to red in Figure 82 demonstrates the burnout wave as it travels through the shield.

Eu_2O_3 is clearly superior as a shield choice, but gadolinium is also highly effective and is far easier to fabricate. Hafnium is easy to fabricate, but it's difficult to purchase and is a weak absorber compared to the other options. B_4C is more effective than hafnium, but burns out too quickly for long term operation.

By moving the gadolinium metal shield to the inside of the water gap, the effective thermal flux in the specimen region is approximately the same as with the previous designs where an Eu_2O_3 shield was used on the outside of the water gap. Figure 83 is a more detailed look at the gadolinium shield performance as a function of time.

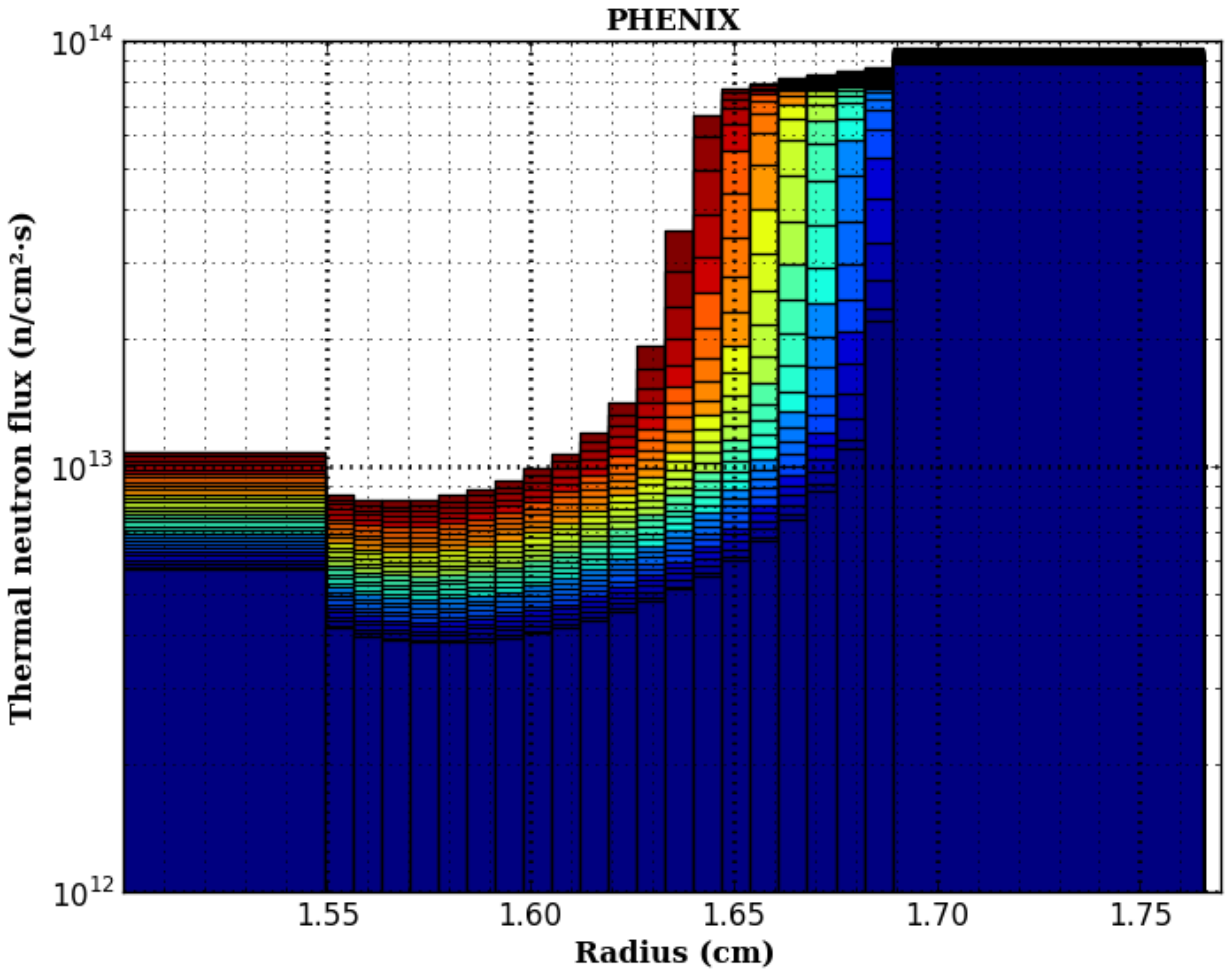

Figure 83. Burnout of a Gadolinium Shield

SUMMARY AND FUTURE PLANS

A conceptual design for a new Fusion materials temperature-controlled capsule is presented. The capsule will be irradiated in one of the RB* positions of the High Flux Isotope Reactor. Specimens will be primarily 3, 6, and 10 mm disks, along with some tensile specimens, and the capsule is to have the option of flowing deuterium over the specimens. The deuterium will be provided in the form of a pre-mixed He/H_2 gas, which will alleviate concerns over the flammability of the deuterium gas. The temperature zones have not been finalized, but will likely be in the range of 300 to 1200°C. A gadolinium shield located inside the coolant gap has been selected as the best method for reducing the thermal neutron flux. Design work will continue through 2015 as specimen loading is finalized. Fabrication and construction is planned for 2015/2016.

11.4 DESIGN AND FABRICATION OF PHENIX TUNGSTEN HFIR IRRADIATION CAPSULES

N. O. Cetiner (cetinerno@ornl.gov), F. D. Riley and D. A. Stringfield

OBJECTIVE

Evaluation of plasma facing components for fusion application is the goal of PHENIX, a Japan-US collaboration project. This task is to evaluate the feasibility of using tungsten materials in helium gas-cooled divertors for DEMO and advanced fusion power reactors, based on the response to neutron irradiation.

SUMMARY

This irradiation task of the PHENIX program will design and irradiate six rabbit capsules in the flux trap of HFIR. Target temperatures are 800 and 1100°C; therefore, there will be two thermal designs. Each capsule will contain a combination of pure tungsten (W), K-doped W, La-doped W, and tungsten-rhenium disk-shaped specimens. These specimens will be supported by SiC retainer specimens, SiC thermometry, and springs inside a molybdenum holder. The primary outer containment is a seal-welded aluminum tube. Helium or neon is used as the fill gas inside the experiment. The specimen temperature is controlled by the axial irradiation location, composition of the heat transfer fill gas, and the size of the gap between the housing and the holder.

PROGRESS AND STATUS

Thermal design requires neutronics calculations to establish heat generation rates for the various tungsten alloy specimens. An MCNP model was created to produce the heat generation rates for each material that is contained in the PHENIX Rabbits. The results are documented, reviewed and approved in a safety basis document C-HFIR-2014-022, R0. The heat generation rates used in the thermal and the safety basis designs are shown in Table 1. The thermal design used ANSYS Finite Element Modelling (FEM). The design drawings for this project were created in PRO/E, and the assemblies were directly imported into ANSYS Workbench. The holder and inner specimen assembly designs are shown in Figure 84.

Table 11. Summary of Design and Safety Basis Heat Generation Rates

Heat generation rate in:	Design Value (W/g)	Safety Basis Value (W/g)
Al-6061	27.7	36.8
Molybdenum	38.0	43.5
Tungsten	52.7	59.5
W82Re18	56.8	98.5
WReLaO	51.1	68.8

Two types of tungsten material specimens will be contained in the experiments. MD specimens are 0.5 mm thick, 6 mm diameter disks that will be used for multiple material property measurements in post irradiation evaluations. TD specimen are 1.0 mm thick, 6 mm diameter disks that will be used for thermal desorption measurements after irradiation.

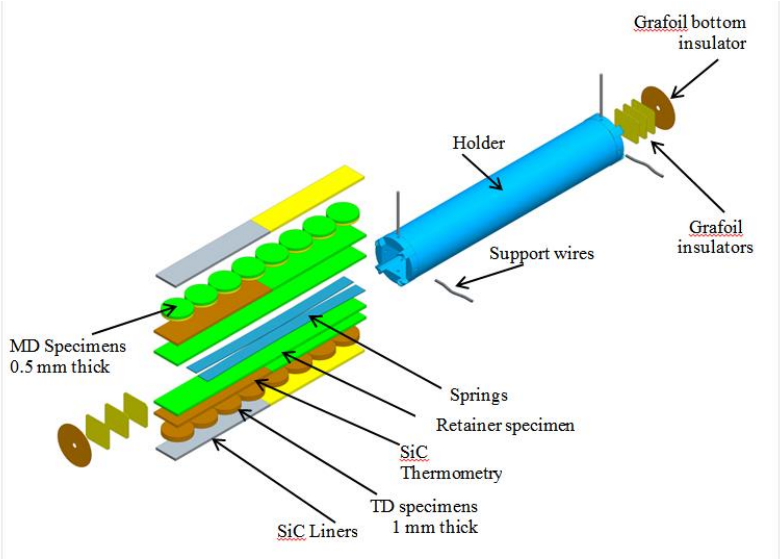

Figure 84. Exploded PRO/E View of the PXW Rabbit Tungsten Rabbit Inner Assembly

The thermal design is composed of two designs. The 800°C design is planned to be irradiated in the target rod rabbit holder axial location-3 (TRRH-3) for 1 and 3 cycles. The 1100°C rabbits are designed to be placed in TRRH-4 for 1 and 3 cycles. The temperature contour plots from the ANSYS FEM Analysis results for the 800 and 1100°C designs are shown in Figure 85 andFigure 86 respectively.

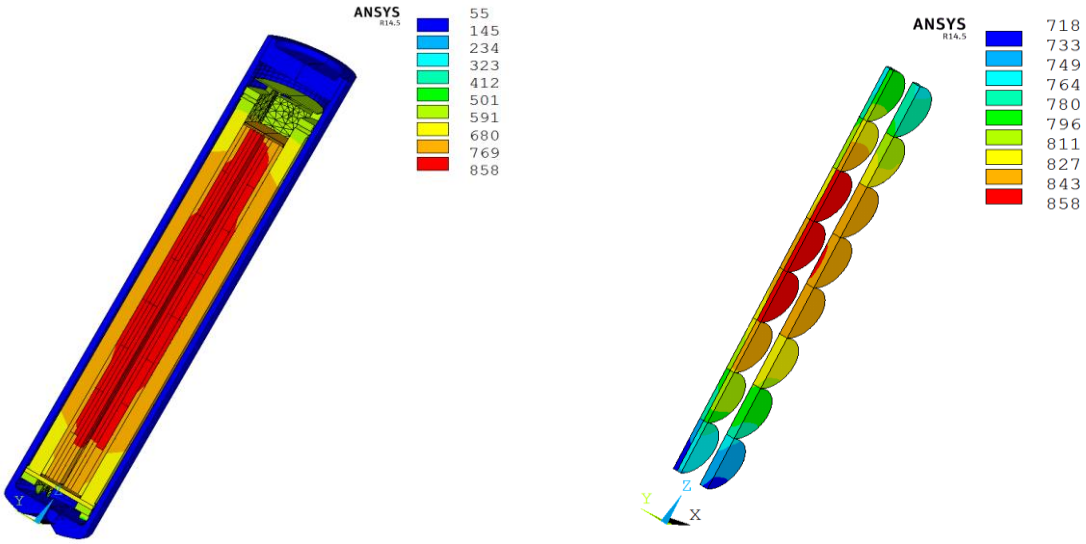

Figure 85. Temperature Contour Plots (°C) for TRRH-3-800°C Case Assembly and Specimens

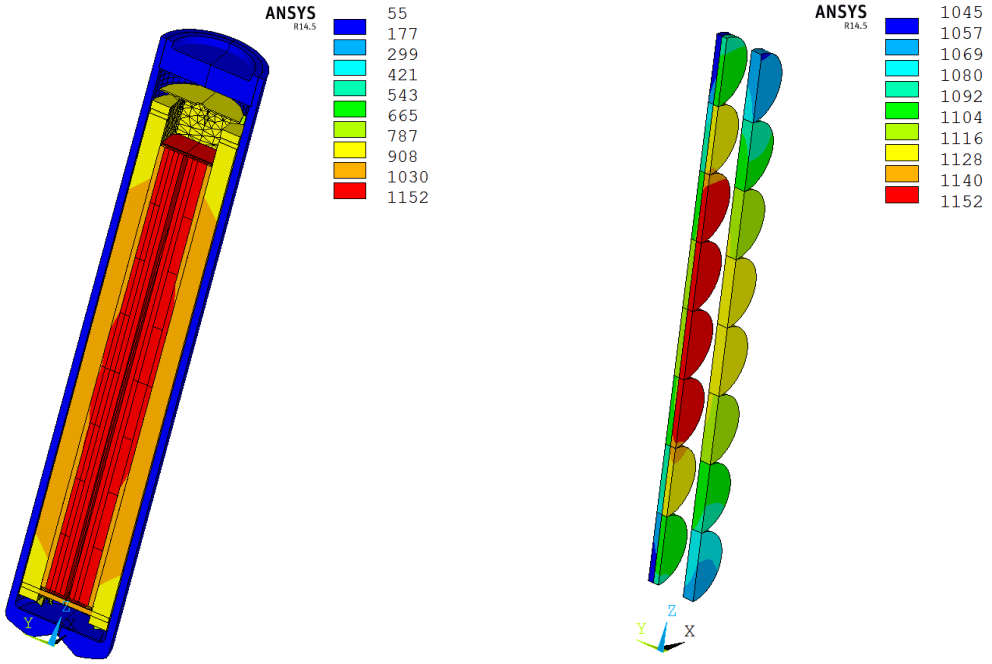

Figure 86. Temperature Contour Plots (°C) for TRRH-4-1100°C Case Assembly and Specimens

The summary of the design temperatures of both the 800 and 1100°C cases are shown in Table 12 andTable 13.

Table 12. Temperature Detail for Design Case TRRH3-800°C with Helium fill gas

Part	Material	Temperature (°C)				
		Ave	Min	Max	T.025	T.975
Housing	AL-6061	66	55	83	56	71
End Cap	AL-6061	78	76	79	77	79
Moly Holder	Molybdenum	679	480	754	546	746
TD specimens	Tungsten	806	728	843	732	843
MD specimens	Tungsten	809	747	858	749	858
Retainer specimen-1	SiC	804	730	841	740	839
Retainer specimen-2	SiC	815	736	852	748	851

Table 13. Temperature Detail for Design Case TH4-1100°C with Neon fill gas

Part	Material	Temperature (°C)				
		Ave	Min	Max	T.025	T.975
Housing	AL-6061	68	55	79	56	71
End Cap	AL-6061	116	115	118	115	118
Moly Holder	Molybdenum	910	769	976	810	968
TD specimen	Tungsten	1100	1055	1125	1059	1125
MD specimens	Tungsten	1108	1045	1152	1047	1152
Retainer specimen-1	SiC	1105	1061	1129	1068	1128
Retainer specimen-2	SiC	1126	1078	1151	1086	1151

A safety basis design and calculation is also being performed using ANSYS. The purpose of this calculation is to demonstrate the safety of irradiating these rabbit capsules in the HFIR flux trap. This

analysis also shows that the melting temperatures of internal components cannot be exceeded and that the specimens cannot produce significant radial or axial stress on the capsule housing under worst operating and expansion conditions.

FUTURE PLANS

The next step in this project is the capsule fabrication. A set of holders with optimized design diameters is currently being machined. The dimensional inspection and non-conforming dimensional justifications are ongoing. Tungsten material specimens and loading lists have been received. Capsule assembly will start as soon as the holders arrive. The fabrication team is planning to submit the rabbits to HFIR for irradiation for cycle 457 projected to start in November 2014.

12.0 NEW AND UPGRADED TESTING CAPABILITIES IN IMET AND LAMDA

J. P. Robertson, A. M. Williams, K. J. Leonard (leonardk@ornl.gov)

SUMMARY

Two ORNL facilities, LAMDA and IMET, provide the equipment and handling capabilities needed for the evaluation of effects of neutron irradiation on non-fuel materials. The post-irradiation examination capabilities in these laboratories shared by the Fusion Materials Program and other programs evaluating irradiation effects on materials continue to expand and improve.

LOW ACTIVATION MATERIALS DEVELOPMENT AND ANALYSIS FACILITY

The Low Activation Materials Development and Analysis Laboratory (LAMDA) facility is a multipurpose irradiated materials science facility for evaluation of materials with low radiological threat. The LAMDA facility typically allows the examination of low radioactivity samples (< 100 mR/hr at 30 cm) without the need for remote manipulation. The preparation facilities for small and compact samples allow researchers to apply cutting-edge characterization and testing equipment for studying radiation effects in materials. During FY 2014 the activities of the LAMDA laboratory have been largely consolidated into one area. This expedites the transfer of specimens between work areas, and improves the cost and efficiency of materials evaluation experiments.

Electron microscopy is a primary focus of LAMDA investigations. The laboratory houses two FEI dual beam (i.e., Focus Ion Beam, or FIB millers) Quanta 3D 200i instruments for specimen preparation. One of these units is inside a lead-lined vault with a remote access console and can be used for high activity samples. The other, shown in Figure 87, is equipped with a cryostage for the milling of hydrogen sensitive materials, such as Zr and other refractory base metal alloys.

An addition this year was a FEI Versa 3D dual beam instrument, equipped with a Schottky Field Emission source with 1 nm resolution. This instrument is equipped with four gas injection systems for variable milling or deposition processes, an integrated plasma cleaner and a cryo-cleaner to achieve the high resolution capabilities. The Versa has the latest secondary electron/ion detectors including an in-column detector, retractable scanning transmission electron microscopy detector and retractable directional backscatter detector to characterize specimens. Recent additions to the instrument also include an Oxford NordlysMax2 electron backscatter diffraction (EBSD) detector and FEI Slice-and-View software. The EBSD detector will allow crystallographic analysis of materials, enabling FIB milling from specific locations and directions. The software package is supported by the Avizo Fire software that will allow 3D serial sectioning of the material and 3D modeling of features.

The Hitachi S-4700 cold-field emission scanning electron microscope (SEM) is available for secondary electron (SE), backscatter electron (BSE), and energy dispersive spectroscopy (EDS) imaging. An in-situ strain fixture for this microscope is also available.

In support of the advanced characterization capabilities a Fischione plasma cleaning system is now available within the LAMDA lab for post-processing cleaning of FIB samples and pre-cleaning of SEM specimens.

A Keyence digital optical microscope provides high resolution, high depth of field, measurement capabilities, three-dimensional tools, and a precision stage. A Keyence IM-6120 digital optical microscope has been added to LAMDA. This is a high-precision image dimension measuring system that

measures dimensions of a sample from the projected image, making precise and instantaneous measurements possible.

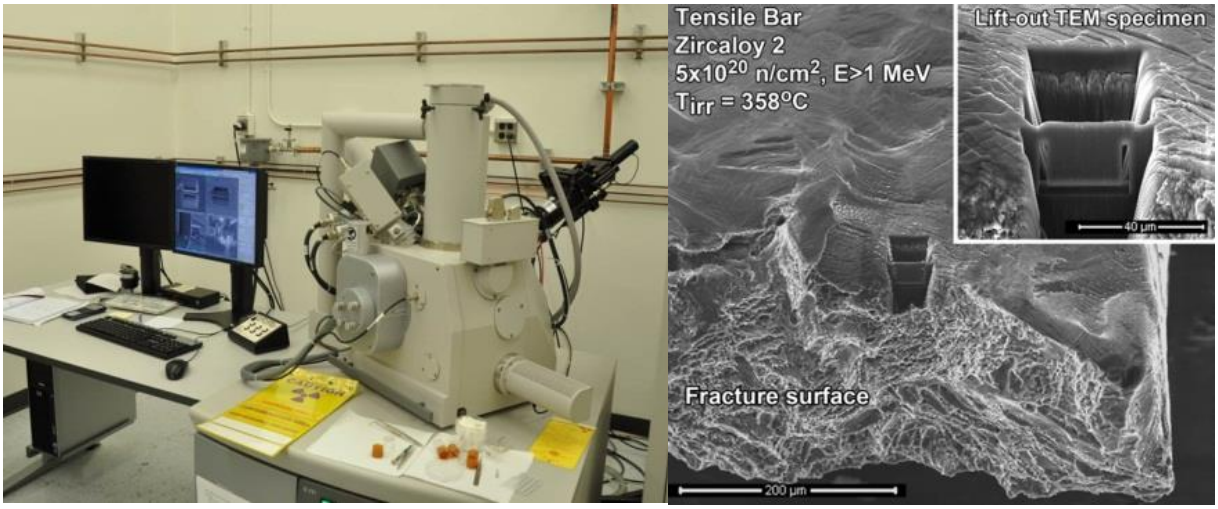

Figure 87. Focused ion beam system for preparation of small examination specimens from irradiated material. Right image shows small foil specimen milled from just below the fracture surface. It will be used for microstructural characterization in an electron microscope.

The installation of a JEOL JEM-2100F transmission electron microscope (TEM) in the LAMDA facility continues into the next FY, with operations expected before the end of the calendar year. This instrument is a 200 kV Schottky emission instrument with scanning-TEM mode capability, with energy dispersive spectrometer and Gatan Image Filter (energy filtered imaging and energy electron loss spectrometry) attachments. Imaging can be performed through the Orius 11 Mpx bottom mounted camera or through the GIF.

A variety of mechanical test systems are available for tension, compression, flexural, or torsional testing, in air, nitrogen, or vacuum, from liquid nitrogen temperatures up to 1800°C. Microhardness testers, sonic velocity measurement systems, impulse excitation technique equipment, impact testers, and creep machines are used to investigate hardness, elastic properties, fracture toughness, ductile-to-brittle transition temperatures, and creep properties.

Physical and thermophysical properties are routinely evaluated in LAMDA. A TA Instruments Q600 Simultaneous Differential Scanning Calorimeter (DSC) and Thermogravimetric Analysis (TGA) Unit measures specific heat capacity and heats of transition, detects phase changes and melting points, and examines time-temperature-environment relationships for materials in aggressive environments simulating processing or operating conditions. In addition, Netsch, Anter, BETA, Sartorious, and Keithley instrument systems are used to measure thermal expansion, thermal diffusivity, thermal conductivity, specific heat capacity, density, mass, volume, and electrical resistivity under a variety of test conditions.

All of these capabilities are supported by state-of-the-art sample preparation equipment.

IRRADIATED MATERIALS EXAMINATION AND TESTING LABORATORY

The Irradiated Materials Examination and Testing (IMET) hot cell facility is a Class III nuclear facility located in Building 3025E at Oak Ridge National Laboratory. These hot cells are the primary mechanical

testing and examination facility for highly irradiated structural alloys and ceramics. The six interconnected steel-lined hot cells contain 320 square feet of work space and are maintained as a low alpha contamination facility to allow transfer of specimens to other radiological laboratories after testing or sorting. Functions that can be performed include capsule disassembly, laser profilometry microscopic examination, grinding, polishing, welding, shearing, machining, sawing, photography, and video examination. Mechanical systems are available for tensile, creep, Charpy impact, fracture toughness, and fatigue testing.

A new JEOL 6010LA SEM was installed in Cell 5 of the IMET facility in FY2014. This is an air-cooled instrument with an advanced user interface outside the cell. This instrument will support Fusion Program objectives by providing SE, BSE, and EDS analysis capabilities.

A small irradiation capsule disassembly system, shown in Figure 88, has been designed, built, and installed in Cell 6. This system is a collection of tools mounted together on a swivel base to expedite the cutting and disassembly of HFIR rabbit capsules. It includes a low speed saw for capsule cutting as well as a modified press for the extraction of samples from the irradiated rabbit capsules.

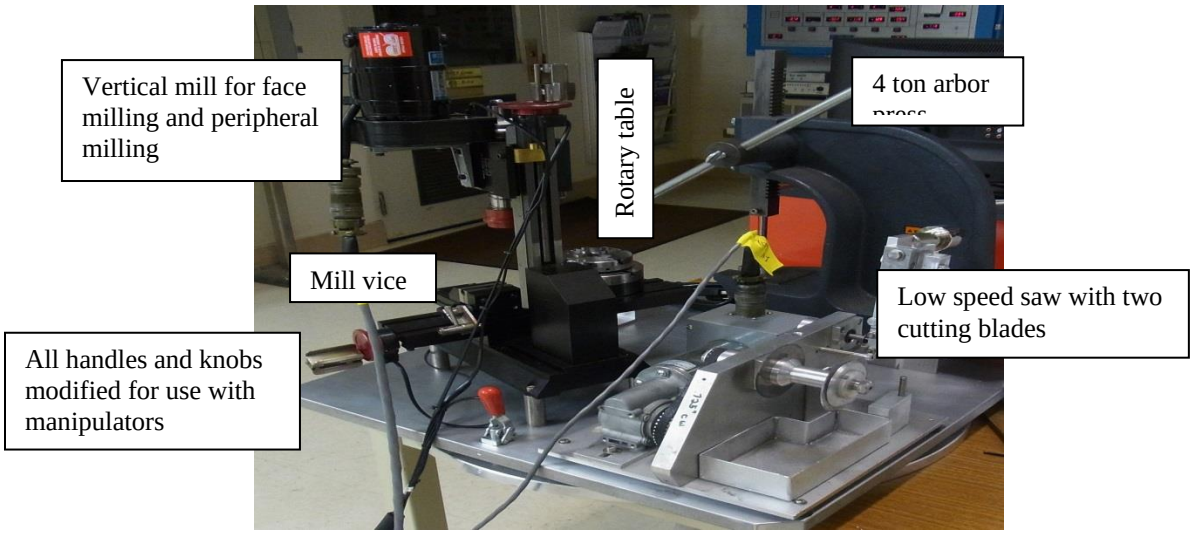

Figure 88. Capsule disassembly system showing the three functional components of the system.

13.0 PUBLICATION AND PRESENTATION RECORD

13.1 PAPERS PUBLISHED IN FY 2014 *(Alphabetical by first author)*

Thak Sang Byun, Ji Hyun Yoon, David T. Hoelzer, Stuart A. Maloy, "Fracture Behavior of 9Cr Nanostructured Ferritic Alloy with Improved Fracture Toughness," *Journal of Nuclear Materials,* 449 (2014) 39-48.

L. El-Guebaly, T. Huhn, A. Rowcliffe, S. Malang, and the ARIES-ACT Team, "Design Challenges and Activation Concerns for ARIES Vacuum Vessel", *Fusion Science and Technology* 64(3), 449-454, (2013)

S. Grasso, P. Tatarko, S. Rizzo, H. Porwal, C. Hu, Y. Katoh, M. Salvo, M.J. Reece, and M. Ferraris, "Joining of β-SiC by Spark Plasma Sintering," *Journal of the European Ceramic Society*, 34 (2014), 1681-86.

D.T. Hoelzer, K.A. Unocic, M.A. Sokolov, Z. Feng "Joining of 14YWT and F82H by Friction Stir Welding", *Journal of Nuclear Materials*, 442 (2013), S529-S534.

Y. Katoh, "Ceramic Matrix Composites in Fission and Fusion Energy Applications", Chapter in *Advances in Ceramic Matrix Composites*, ed. by I.M. Low (Cambridge, UK: Woodhead Publishing Limited, 2014), pp. 496-523.

Y. Katoh, K. Ozawa, C. Shih, T. Nozawa, R.J. Shinavski, A. Hasegawa, L.L. Snead, "Continuous SiC Fiber, CVI SiC Matrix Composites for Nuclear Applications: Properties and Irradiation Effects," *Journal of Nuclear Materials*, 448 (2014) 448-476.

Y. Katoh, L.L. Snead, T. Cheng, C. Shih, W.D. Lewis, T. Koyanagi, T. Hinoki, C.H. Henagar, M. Ferraris, "Radiation-Tolerant Joining Technologies for Silicon Carbide Ceramics and Composites," *Journal of Nuclear Materials,* 448 (2014) 497-511.

H. Katsui, Y. Katoh, A. Hasegawa, M. Shimada, Y. Hatano, T. Hinoki, S. Nogami, T. Tanaka, S. Nagata, and T. Shikama, "Tritium Trapping in Silicon Carbide in Contact with Solid Breeder under High Flux Isotope Reactor Irradiation", *Journal of Nuclear Materials*, 442 (2013), S497-S500.

T. Koyanagi, K. Shimoda, S. Kondo, T. Hinoki, K. Ozawa, Y. Katoh, "Irradiation Creep of Nano-Powder Sintered Silicon Carbide at Low Neutron Fluences," *Journal of Nuclear Materials,* (2014), 455 [1-3] (2014) 73-80.

K.J. Leonard, T. Aytug, A.A. Gapud, F.A. List III, N.T. Greenwood, Y. Zhang, A.G. Perez-Bergquist, W.J. Weber and M.W. Rupich, "Irradiation Response of Next Generation High Temperature Superconductors for Fusion Energy Applications", *Fusion Sci. and Techn.*, 66, 1 (2014) 57-62.

K.J. Leonard, G.E. Jellison Jr., N.A.P. Kiran Kumar and L.L. Snead, "The Role of Microstructure on the Optical Performance of Neutron Irradiated Dielectric Mirrors," *Journal of Nuclear Materials,* 445 (2014) 281-290.

Alejandro G. Perez-Bergquist, Hongbin Bei, Keith J. Leonard, Yanwen Zhang, and Steven J. Zinkle, "Effects of Ion Irradiation on $Zr_{52.5}Cu_{17.9}Ni_{14.6}Al_{10}Ti_5$ (BAM-11) Bulk Metallic Glass," *Intermetallics* 53 (2014) 62-66.

B. A. Pint and K. A. Unocic, "Pb-Li Compatibility Issues for DEMO" *Journal of Nuclear Materials,* 442 (2013) S572-575.

M. Sawan, Y. Katoh, and L.L. Snead, "Transmutation of Silicon Carbide in Fusion Nuclear Environment", *Journal of Nuclear Materials*, 442 (2013), S370-S375.

R. E. Stoller and Yu. N. Osetsky, "An Atomistic Assessment of Helium Behavior in Iron," *J. Nucl. Mater.*, 455 (2014) 258-262, accepted and online June 2014.

S. K. Sundaram, P. Colombo, and Y. Katoh, "Selected Emerging Opportunities for Ceramics in Energy, Environment, and Transportation", *International Journal of Applied Ceramic Technology*, 10 (2013), 731-39.

L. Tan, T.S. Byun, Y. Katoh, L.L. Snead, "Stability of MX-type strengthening nanoprecipitates in ferritic steels under thermal aging, stress, and ion irradiation," *Acta Materialia* 71 (2014) 11-19.

L. Tan, Y. Katoh, L.L. Snead, "Stability of the Strengthening Nanoprecipitates in Reduced Activation Ferritic Steels under Fe2+ Ion Irradiation," *Journal of Nuclear Materials* 445 (2014) 104-110.

D. Terentyev, A. Bakaev, Yu.N. Osetsky, "Interaction of Dislocations with Frank Loops in Fe-Ni Alloys and Pure Ni", *Journal of Nuclear Materials*, 442 (2013), S628-S632.

K. A. Unocic, M. Lance and B. A. Pint, "Characterization of Specimens Exposed in a Li Loop," *Journal of Nuclear Materials*, 442 (2013) S580-S584.

S.J. Zinkle, "Evaluation of High Strength, High Conductivity CuNiBe Alloys for Fusion Energy Applications", *Journal of Nuclear Materials,* in press (Sept., 2013), doi 10.1016/j.jnucmat.2013.09.007.

S.J. Zinkle and A. Möslang, "Evaluation of irradiation facility options for fusion materials research and development" *Fusion Engineering & Design*, 88, (2013) 472-482. Doi 10.1016/j.fusengdes.2013.02.081

S.J. Zinkle, A. Möslang, T. Muroga and H. Tanigawa, "Multimodal options for materials research to advance the basis for fusion energy in the ITER era", *Nuclear Fusion* 53, (2013) 104024. doi:10.1088/0029-5515/53/10/104024

13.2 PAPERS SUBMITTED IN FY 2014 *(Awaiting publication)*

A.A. Gapud, N.T. Greenwood, J.A. Alexander, A. Khan, K.J. Leonard, T. Aytug, F.A. List III, M. Rupich and Y. Zhang, "Irradiation of Commercial, High Tc Superconducting Tape for Potential Fusion Applications: Electromagnetic Transport Properties," submitted to *Superconductor Science and Technology.*

Takaaki Koyanagi, Jim O. Kiggans, Chunghao Shih, Yutai Katoh, "Processing and Characterization of Diffusion-Bonded Silicon Carbide Joints Using Molybdenum and Titanium Interlayers," accepted for publication in *Ceramic Engineering and Science Proceedings*.

Chad M. Parish and Yutai Katoh, "Understanding checkerboard-like EBSD artifacts in CVD 3C-SiC," Submitted to *Microscopy and Microanalysis*

Alejandro G. Perez-Bergquist, Takashi Nozawa, Chunghao Shih, Keith J. Leonard, Lance L. Snead, and Yutai Katoh, "High Dose Neutron Irradiations of Hi-Nicalon Type S Silicon Carbide Composites, Part 1: Microstructural Evaluations," Submitted to *Journal of Nuclear Materials.*

A.S. Sabau, E.K. Ohriner, J.O. Kiggans, C.R. Schaich, Y. Ueda, D.C. Harper, Y. Katoh, L.L. Snead and T.S. Byun, "High-Heat Flux Testing of Irradiated Tungsten based Materials for Fusion Applications using Infrared Plasma Arc Lamps" submitted to the *Journal of Nuclear Materials*.

W. Tang, J. Chen, X. Yu, D.A. Frederick, Z. Feng, "Heat Input and Post Weld Heat Treatment Effects on Reduced-Activation Ferritic/Martensitic Steel Friction Stir Welds," submitted to the proceedings of a 2015 *TMS Conference*

M. S. Tillack, X. R. Wang, D. Navaei, H. H. Toudeshki, A. F. Rowcliffe, F. Najmabadi and the ARIES Team, "Design and Analysis of the ARIES- ACT 1 Fusion Core", submitted to *Fus. Eng. Design*

K. A. Unocic, D. T. Hoelzer and B. A. Pint, "The Microstructure and Environmental Resistance of Low-Cr ODS FeCrAl," submitted to *Materials at High Temperature*

K. A. Unocic and B. A. Pint, "Alloying and Coating Strategies for Improved Pb-Li Compatibility," submitted to *Journal of Nuclear Materials*.

X.Yu, B. Mazumder, M.K. Miller, S.A. David, and Z. Feng, "Stability of Y–Ti–O Nanoclusters in Friction Stir Welded Nanostructured Ferritic Alloys," submitted to *Script Mat*.

13.3 PRESENTATIONS *(Only includes OFES-funded ORNL resenting Authors)*

Presentations associated with ICFRM-16, Beijing October 20-26, 2013

a. Plenary, Invited and Oral Presentations

Thak Sang Byun, Ji Hyun Yoon, David T. Hoelzer, Stuart A. Maloy**, "***Fracture Behavior of 9Cr Nanostructured Ferritic Alloy with Improved Fracture Toughness."*

D.T. Hoelzer, K.A. Unocic and D. Shin, "*Computational and Experimental Studies of the Stability of Oxides for Development of ODS FeCrAl for Fusion Reactor Applications*."

Y. Katoh, L.L. Snead, C.H. Henager, Jr., T. Nozawa, T. Hinoki, A. Iveković, S. Novak, S.M. Gonzalez de Vicente, "*Current Status and Recent Research Achievements in SiC/SiC Composites*."

T. Koyanagi, Y. Katoh, L.L. Snead, C. Shih, T. Hinoki, M. Fukuda, K. Shimoda, S. Kondo, K. Ozawa and A. Hasegawa, "*Irradiation Creep Behavior of Silicon Carbide Materials Beyond the Initial Transient*,"

K.J. Leonard, T. Aytug, A.A. Gapud, F.A. List III, N.T. Greenwood, Y. Zhang, A.G. Perz-Bergquist, and W.J. Weber, "*Irradiation Response of Next Generation High Temperature Superconductors for Fusion Energy Applications*."

A.G. Perez-Bergquist, K.J. Leonard, Y. Katoh, L.L. Snead, C. Shih, R.A. Meisner, and T. Nozawa, "*Microstructural Evolutions in Advanced Silicon Carbide Composites Neutron-Irradiated to High Fluences*."

A.S. Sabau, E.K. Ohriner, T.S. Byun, Y. Katoh, J.O. Kiggans, Y. Ueda, L.L. Snead, and D.C. Harper, *"High-Heat Flux Testing of Irradiated W-based Materials for Fusion Applications using Infrared Plasma Arc Lamps."*

L.L. Snead, "*Neutron Irradiation Effects in Pure and Engineered Forms of Tungsten."*

R.E. Stoller, Yu. N. Osetsky, "*Atomistic Assessment of He Bubbles and an Equation of State for He in Iron*."

L. Tan, T.S. Byun, Y. Katoh, L.L. Snead, G.S. Was, "*Stability of MX nanoprecipitates in ferritic steels under thermal, stress, and ion irradiation."*

K. A. Unocic and BA Pint, "*Alloying and Coating Strategies for Improved Pb-Li Compatibility*."

S.J. Zinkle, G. Federici, C.E. Kessel, S. Konishi, T. Muroga and L.L. Snead, "*Near-term Research Challenges for Fusion Nuclear Materials Systems.*"

b. Poster Presentations

Alexander V. Barashev, Stanislav I. Golubov and Roger E. Stoller, "*Mean-Field Model of Gas Bubbles and Dislocation Loop Evolution in Metallic Materials Under Neutron Irradiation and Thermal Aging Conditions*."

P. D. Ferguson, L. L. Snead, and S. A. Maloy, M. W. Wendel, R. E. Stoller, "*A Fusion Materials Irradiation Test Station at the Spallation Neutron Source."*

N.A.P. Kiran Kumar, K.J. Leonard, H. Bei, T.S. Byun, Yanwen Zhang and S.J. Zinkle, "*Microstructural Stability and Mechanical Behavior of FeMnNiCr High Entropy Alloy under Ion and Neutron Irradiation*",

K.J. Leonard, N.A.P. Kiran Kumar, G.E. Jellison Jr. and L.L. Snead "*Structural Causes of Optical Changes in Neutron Irradiated Dielectric Mirrors*"

Yuri Osetsky, Roger E. Stoller and Dmitry Terentyev, "*Radiation-Induced Obstacles in Iron and Ferritic Alloys: An Atomic-Scale View*."

Alejandro G. Perez-Bergquist, Hongbin Bei, Keith J. Leonard, Yanwen Zhang, and Steven J. Zinkle "*Effects of Ion Irradiation on* $Zr_{52.5}Cu_{17.9}Ni_{14.6}Al_{10}Ti_5$ *(BAM-11) Bulk Metallic Glass***."**

A.G. Perez-Bergquist, Y. Katoh, C. Shih, N.A.P. Kiran Kumar, and S.J. Zinkle, "*Effect of Neutron Irradiation on Ti-Si-C MAX-Phase Ceramic Microstructures."*

Arthur F.Rowcliffe, S.J.Zinkle, R.K.Nanstad, L El-Guebaly, M.Tillack, L.Tan, F.W.Wiffen " *Structural Materials for Lifetime Components of Long-Term Fusion Energy Systems*"

German Samolyuk, Yuri Osetsky and Roger E. Stoller, "*Molecular Dynamics Modeling of Atomic Displacement Cascades in 3C-SiC*."

C. Shih, Y.Katoh, J.O. Kiggans, L.L. Snead, H.E. Khalifa, C. Back, T. Koyanagi, T. Hinoki, M. Ferraris, and S.T. Gonczy, "*Shear Strength Test Development for Irradiation Study of Joined Materials*."

Z. Yu, Z. Feng, D.T. Hoelzer, L. Tan, and M.A. Sokolov, "*Friction Stir Welding of ODS steels and RAFM steels"*

c. Lectures at Short Course Tutorial on Foundations of Fusion Materials

R.E. Stoller, "*Theory and Modeling for Fusion Reactor Materials*"

S.J. Zinkle, "*Fundamentals of Fusion Materials Radiation Effects*"

d. Presentations at IEA Fusion Materials Workshops

T.S. Byun, "*A Brief on ORNL Advanced Steel Efforts*"

Yutai Katoh*, "An Update on Recent US Work on SiC/SiC*"

L.L. Snead**,** "*Ongoing ORNL / KIT Collaborative Study on Neutron Irradiation Effects in Tungsten*"

K.A. Unocic, D.T. Hoelzer and B.A. Pint, "*Characterization of Specimens Exposed in Vanadium Loop with Flowing Li*"

Presentations at the 38th International Conference on Advanced Ceramics and Composites, January 26-31, 2014, Daytona Beach, FL.

S.T. Gonczy, Y. Katoh, M. Ferraris, *"Development of an ASTM C28 Test Standard for the Torsional Shear Strength of Adhesive Bonds for Advanced Ceramics."*

Y. Katoh, T. Koyanagi, C. Shih, T. Hinoki, L.L. Snead, *"Irradiation creep of silicon carbide beyond the initial transient."*

T. Koyanagi, J.O. Kiggans, C. Shih, Y. Katoh, *"Processing and characterization of diffusion-bonded silicon carbide joints using molybdenum and titanium interlayers."*

C. Shih, J.O. Kiggans, H.E. Khalifa, C. Back, T. Koyanagi, M. Ferraris, Y. Katoh, *"Comparison of shear strength of ceramic joints determined by various test methods with small specimens."*

L.L. Snead, Y. Katoh, W. Porter, M.A. Fechter, *"Extending the Application and Functional Range of SiC Irradiation Temperature Monitors."*

L.L. Snead, Y. Katoh, K. Terrani, A. Perez-Bergquest, K. Leonard, *"Microstructural Stability of Neutron Irradiated Nano-Powder-Derived SiC."*

J. Su, J. Hemrick, S. Yu, C. Shih, R.J. Shinavski, S. Gonczy, Y. Katoh, *"Characterization of Advanced SiC/SiC Composite Tubes Under Monotonic Axial Tensile Loading at Ambient Temperature."*

A.Ventrella, M. Salvo, F. Smeacetto, S. Rizzo, V. Casalegno, D. Gross, S. Gonczy, Y. Katoh, M. Ferraris, *"Torsion tests on joined materials."*

Other Presentations during FY 2014, ordered by presentation date

S.J. Zinkle, J.P. Blanchard, R.W. Callis, C.E. Kessel, R.J. Kurtz, P.J. Lee, K.A. McCarthy, N.B. Morley, R.E. Nygren, G.R. Tynan, D.G. Whyte, R.S. Willms and B.D. Wirth, "*Fusion Materials Science and Technology Research Opportunities Now and During the ITER Era*," 11th International Symposium on Fusion Nuclear Technology, Barcelona, Spain, Sept. 16-20, 2013.

Wendel, M. W. and T. J. McManamy, "*FMITS at SNS*," Workshop on fast neutron applications at spallation sources, Abingdon, UK, 30 September - 1 October 2013.

S.J. Zinkle, "*Foundations of Materials Engineering Challenges in Fission and Fusion Energy*," China Distinguished Materials Scientists Forum, School of Materials and Engineering, University of Science & Technology Beijing, Beijing, China, Oct. 24, 2013.

Y. Katoh, K. A. Terrani, L. L. Snead, "*Ceramic Matrix Composites for Nuclear and Fusion Ene*rgy," at Materials Science and Technology 2013, October 27-31, 2013, Montreal, Canada.

S.J. Zinkle, "*Materials Engineering Challenges in Fission and Fusion Energy*," Nuclear Science & Engineering department seminar, Massachusetts Institute of Technology, Cambridge, MA, Nov. 4, 2013.

S.J. Zinkle, "*Materials Engineering Challenges in Fission and Fusion Energ*y," Nuclear Engineering department seminar, Purdue University, West Lafayette, Indiana, Nov. 20, 2013.

A.A. Gapud, J.A. Alexander, A. Khan, K.J. Leonard, T. Aytug, F.A. List III and Y. Zhang, "*Irradiation of Commercial, High-T_c Superconducting Tape for Potential Fusion Applications: Electromagnetic Transport Properties*", 80th Annual Meeting of the American Physical Society Southeastern Section Conference in Bowling Green, Kentucky. November 23, 2013.

A.F. Rowcliffe, *"Assessment of Materials Issues Related to Next Step Fusion Systems"*, presented to FNSF Systems Study Meeting, PPPL Princeton, Jan 28-30, 2014

Z. Yu, Z. Feng, D. Hoelzer, L. Tan, M.A. Sokolov, *"Similar and Dissimilar Friction Stir Welding of ODS and RAFM Steels,"* TMS Annual Meeting, Feb 16-20, 2014, San Diego, CA.

K. A. Unocic, D. T. Hoelzer and B. A. Pint, *"The Microstructure and Environmental Resistance of Low-Cr ODS FeCrAl,"* presented April 15, 2014 at the 9th Microscopy of Oxidation Conference, Nottingham, UK.

X. Chen, Z. Yu and Z. Feng, *"FSW of Reduced Activations Steels with PWHT",* 10th Int. Friction Stir Welding Symposium, May 20-22, 2014, Beijing, China.

Adrian S. Sabau, Jim Kiggans, Evan K. Ohriner, Kazutoshi Tokunaga, Yutai Katoh, Lance L. Snead, and David C. Harper, "*Update on High-Heat Flux Testing of Irradiated W-based Materials using Plasma Arc Lamps,"* PHENIX Task 1 Workshop, June 5-6, 2014, Kyoto University, Japan.

Y. Katoh, C. Shih, C. Parish, K.J. Leonard, S.J. Zinkle, T.S. Byun, T. Toyama, and T. Shikama, *"Effects of Neutron Irradiation on MAX-phase Ceramics,"* CIMTEC 2014 – Forum on New Materials, June 15-20, 2014, Montecatini Terme, Italy.

Y. Katoh, *"ORNL Research on Silicon Carbide Joining for Nuclear Applications,"* Workshop on Joining of SiC-based Materials for Nuclear Applications, June 20, 2014, Turin, Italy.

Chad M. Parish, Takaaki Koyanagi, Sosuke Kondo (Kyoto University), and Yutai Katoh, *"Atomic-Resolution Investigation of Irradiation-Induced Defects in Silicon Carbide"* Microscopy and Microanalysis 2014, August 3-7, Hartford, Connecticut

Chad M. Parish, *"When does FIB preparation of irradiated materials make sense?"* at Department of Energy workshop on TEM Characterization of Irradiation Induced Defects, Argonne National Laboratory, September 3-5, 2014.

Yutai Katoh, *"Advanced tungsten fabrication,"* presentation to the High-Power Density US/Japan Workshop, Tohoku University, Sendai, Japan, Sept. 11-13.

Adrian S. Sabau, Jim Kiggans, Evan K. Ohriner, Kazutoshi Tokunaga, Yutai Katoh, Lance L. Snead, and David C. Harper, *"Testing of High-Heat Flux Components using Plasma Arc Lamps,"* presentation to the High-Power Density US/Japan Workshop, Tohoku University, Sendai, Japan, Sept. 11-13.

Lance L. Snead, *"Tungsten Irradiation Effects,"* presentation to the High-Power Density US/Japan Workshop, Tohoku University, Sendai, Japan, Sept. 11-13.

Adrian S. Sabau, Jim Kiggans, Evan K. Ohriner, Kazutoshi Tokunaga, Yutai Katoh, Lance L. Snead, and David C. Harper, *"PAL status and HHF tests",* presentation to the PHENIX Workshop on Planning of Neutron Irradiation Experiments, Tohoku University, Sendai, Japan, Sept. 12-13.

Lance L. Snead, "*PIE status and results from previously irradiated W*," presentation to the PHENIX Workshop on Planning of Neutron Irradiation Experiments, Tohoku University, Sendai, Japan, Sept. 12-13.

Yutai Katoh, "*Material development and evaluation in USA*," presentation to the PHENIX Workshop on Planning of Neutron Irradiation Experiments, Tohoku University, Sendai, Japan, Sept. 12-13.

Y. Katoh, J.L. McDuffee, "*PHENIX irradiation program status*," presentation to the PHENIX Workshop on Planning of Neutron Irradiation Experiments, Tohoku University, Sendai, Japan, Sept. 12-13.

L. Snead, L. Garrison, N.A.P. Kiran Kumar, T. S. Byun, M. R. McAlister, W. D. Lewis (ORNL) M. Rieth, S. Antusch, J. Reiser, J. Hoffmann, L. Commin, T. Weingärtner (KIT) *" Update on the ORNL KIT Collaborative Study on Neutron Irradiation Effects in Tungsten."* IEA Workshop on W and W-alloy Development for Protection and Structural Application in Fusion Reactors, associated with SOFT 2014 in San Sebastián, Spain, September 29, 2014. (Presented for ORNL authors by Steffen Antusch of Karlsruhe Institute of Technology)